TURBULENCE MODELING FOR SHOCK WAVE/TURBULENT BOUNDARY

LAYER INTERACTIONS

A Dissertation

Submitted to the Faculty

of

Purdue University

by

Randolph P. Lillard

In Partial Fulfillment of the

Requirements for the Degree

of

Doctor of Philosophy

December 2011

Purdue University

West Lafayette, Indiana

ACKNOWLEDGMENTS

[Put statement of appreciation or recognition of special assistance here.]

PREFACE

This research was driven by needs identified at NASA Johnson Space Center during the Agency's Return to Flight effort. The computational prediction of ascent aeroheating environments for the Space Shuttle has long been challenging due to the side-mounted configuration and geometric complexity of the vehicles. This combination leads complicated flow phenomenon, including massively separated flows interacting and being caused by multiple shock waves. The intent of this effort was to leverage the capability developed at NASA in the 1990's using overset grids with the OVERFLOW code to predict the aerodynamics of this configuration. It was recognized that aerothermodynamic predictions of this configuration, unlike bulk aerodynamic properties and even to a lesser extend running loads, are dominated by the viscous effects and thus required enhanced physical modeling of the turbulent boundary layer and the complicated interations. The models proposed and assessed here are an attempt to provide that enhancement.

TABLE OF CONTENTS

LIST OF TABLES

LIST OF FIGURES

SYMBOLS

Greek Symbols

α	Thermal diffusivity or turbulence modeling constant
β	Clauser's pressure gradient parameter
δ	Boundary layer thickness, m
δ^*	Displacement thickness, m
ϵ	Dissipation per unit mass, m^2/s^3
κ	Closure coefficient
μ	Dynamic viscosity, $kg/m \cdot s$
ν	Kinematic viscosity, m^2/s
ω	Specific dissipation, s^{-1}
ρ	Density, kg/m^3
σ	Turbulence modeling constant
τ_{ij}	Reynolds stress tensor, Pa
θ	Momentum thickness, m

English Symbols

a	Turbulence modeling constant
c	Sound speed, m/s
c_μ	Turbulence modeling constant
C_p	Pressure coefficient
C_f	Skin friction coefficient
k	Turbulent kinetic energy
l	Turbulence model mixing length, m
M	Mach number
M_{1n}	Normal shock Mach number

xvii

M_c	Convective Mach number
P	Pressure, Pa
$\mathcal{P}$	Turbulent model production term
Pr	Prandtl number, ν/α
q	Heat flux per unit area, W/m^2
s_{ij}	Strain rate tensor, 1/s
S_t	Stanton number, $q_w/\rho_\infty U_\infty C_p(rT_{aw} - T_w)$
T	Static temperature, K
$\widetilde{u'v'}$	Turbulent shear, m^2/s^2
u', v'	Fluctuating velocity components, m/s
x, y	Cartesian body axes, m

Subscripts

aw	Adiabatic wall
eq	Equilibrium condition
k	Kinetic energy equation constant
o	Total conditions
w	Wall conditions
t	Turbulent conditions
∞	Freestream conditions
ω	Specific dissipation equation constant

Superscripts

D	Diviatoric part of a tensor

ABBREVIATIONS

CAIB	Columbia Accident Investigation Board
CEV	Crew Exploration Vehicle
CFD	Computational Fluid Dynamics
CUBRC	Calspan University of Buffalo Research Center
DNS	Direct Numerical Simulation
EARS	Explicit Algebraic Reynolds Stress
ET	External Tank
IH	Integrated Heating (test)
LES	Large Eddy Simulation
RANS	Reynolds Averaged Navier-Stokes
RST	Reynolds Stress Tensor
SA	Spalart-Allmaras Turbulence Model
SRB	Solid Rocket Boosters
SST	Shear Stress Transport Turbulence Model
STS	Space Transportation System
SWTBLI	Shock Wave / Turbulent Boundary Layer Interactions

ABSTRACT

Lillard, Randolph P. Ph.D., Purdue University, December 2011. Turbulence Modeling for Shock Wave/Turbulent Boundary Layer Interactions. Major Professors: Anastasios S. Lyrintzis and Gregory A. Blaisdell.

Accurate aerodynamic computational predictions are essential for the safety of space vehicles, but these computations are of limited accuracy when large pressure gradients are present in the flow. The goal of the current project is to improve the state of compressible turbulence modeling for high speed flows with shock wave / turbulent boundary layer interactions (SWTBLI). Emphasis will be placed on models that can accurately predict the separated region caused by the SWTBLI. These flows are classified as nonequilibrium boundary layers because of the very large and variable adverse pressure gradients caused by the shock waves. The lag model was designed to model these nonequilibrium flows by incorporating history effects. Standard one- and two-equation models (Spalart Allmaras and SST) and the lag model will be run and compared to a new lag model. This new model, the Reynolds stress tensor lag model (lagRST), will be assessed against multiple wind tunnel tests and correlations. The basis of the lag and lagRST models are to preserve the accuracy of the standard turbulence models in equilibrium turbulence, when the Reynolds stresses are linearly related to the mean strain rates, but create a lag between mean strain rate effects and turbulence when nonequilibrium effects become important, such as in large pressure gradients. The affect this lag has on the results for SWBLI and massively separated flows will be determined. These computations will be done with a modified version of the OVERFLOW code. This code solves the RANS equations on overset grids. It was used for this study for its ability to input very complex geometries into the flow solver, such as the Space Shuttle in the full stack configuration. The model was successfully implemented within two versions of the OVERFLOW code. Results show a substantial improvement over the baseline models for transonic separated flows. The results are mixed for the SWBLI assessed.

Separation predictions are not as good as the baseline models, but the over prediction of the peak heat flux downstream of the reattachment shock that plagues many models is reduced.

1. Introduction

Computational predictions of the aerodynamic and aerothermodynamic environments a space vehicle encounters are essential for the design and operation of the vehicle. As computer speeds continue to increase, Computational Fluid Dynamics (CFD) can be used to not only predict the flowfield around simple configurations, but also complex vehicles such as the Space Shuttle. The advances in computer speeds have given rise to advances in the modeling of turbulent flows using Direct Numerical Simulations (DNS) and Large Eddy Simulations (LES). For complex configurations such as the Space Shuttle, DNS or even LES are still impractical because of the grid spacing requirements and the need for time-accurate solutions. Although DNS and LES employ a more physics based representation of the fluid dynamics occurring, the Reynolds Averaged Navier Stokes (RANS) Equations solved along with a turbulence model are still a valuable tool for aerodynamic analysis. The averaging process leaves variables that must be modeled because no explicit relationship between the new quantities and the mean flowfield averaged quantities are given. This is called the closure problem. The quantities that need modeling are the Reynolds stress tensor (RST) and the turbulent heat flux vector. These turbulence models typically use the Boussinesq approximation for the Reynolds Stress closure, relating mean strain rate to the RST in a linear fashion. More general representations of the RST (i.e. not limited by the Boussinesq approximation) have given mixed results, a possible reason being the complexity of the formulations. Despite the speed advantages, turbulence models can not capture all the relevant physics of the problem and are prone to inaccuracies in adverse pressure gradient regions, especially those with shock waves such as many compressible flows.

Applications at the NASA Johnson Space Center use Computational Fluid Dynamics (CFD) predictions in the design and analysis of all spacecraft, including the Space Shuttle on ascent and re-entry. CFD computations are used along with wind tunnel testing to create an aerodynamic and aerothermodynamic database for the vehicle as well as solve any post-
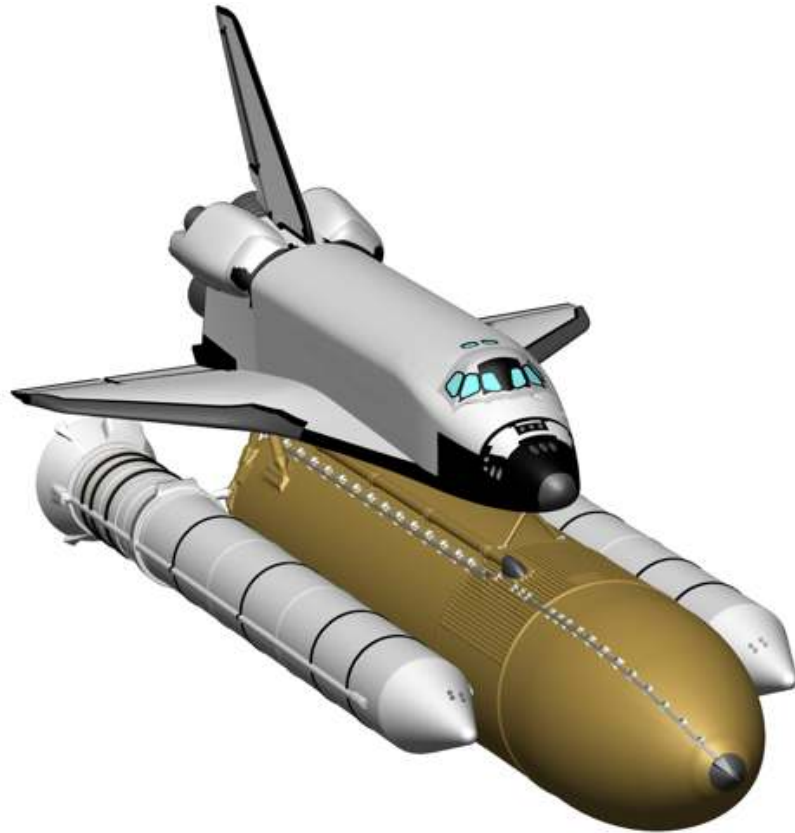
Figure 1.1. Space Shuttle Ascent Stack configuration.

design problems that may pose a flight risk. CFD computations are advantageous for quick decisions as planning and executing a wind tunnel test can take anywhere from a few weeks to years and can cost up to a few million dollars. Although quicker than wind tunnel tests, CFD computations carry a higher uncertainty in complicated flow regions, especially if wind tunnel tests are not available to validate the computations. Typically, CFD is initially used in conjunction with a wind tunnel test, then if any predictions are needed the CFD is applied in the same manner as in comparison to the wind tunnel test and the uncertainties from the comparison of the CFD to the wind tunnel test are used in the predictions.

1.1 Motivation

One of the major recommendations of the Columbia Accident Investigation Board (CAIB) report [1] was to remove all sources of debris from the Space Shuttle. This configuration, pictured in figure 1.1, has the orbiter side mounded to the External Tank (ET) along with two Solid Rocket Boosters (SRB) attached on opposite sides of the ET. The bipod attach fitting carries the load between the orbiter and the ET underneath the nose of the orbiter. The foam ramp covering the bipod fitting was targeted for removal because of the CAIB recommendation, and its probable fault as being the foam that impacted the wing leading edge causing the Space Transportation System (STS)-107 accident. Figure 1.2, shows the bipod attachment region with and without foam ramps covering the attachment structures. The flowfield in the bipod region is very complicated because of several shock wave/turbulent boundary layer interactions and protuberances in the flowfield.

All the computations were done with the OVERFLOW code **??** due to its ability to handle very complex grids. THe OVERFLOW code was developed in part to predict the flow around the Space Shuttle configuration. The ability of the code to use overset grids made it the only feasible way to provide computational predictions. Figure 1.3 shows a CFD solution of the bipod attachment region at Mach 3.2. Contour lines of Mach number are shown. The orbiter bow shock impinges on the turbulent boundary layer of the ET separating the boundary layer upstream of the bipod. In addition, a shock wave emanates from each SRB and interacts in this region. Figure 1.4 shows Mach contours at a constant axial station. The upstream influence of the bipod attachment fitting can be seen in the behavior of the boundary layer. Figure 1.5 shows surface C_p contours at a Mach 3.5 condition. Notice the SRB shocks and the large separation region merging into one complicated interaction. The stringers (ridges upstream of the bipod) add another level of complexity because of the non-smooth surface on the ET.

By removing the foam ramp, the metal bipod structure is exposed to the flow, which creates two distinct challenges. The first is that thermal environments for the bipod fitting need to be generated and validated. Second, the absence of the bipod ramps change the
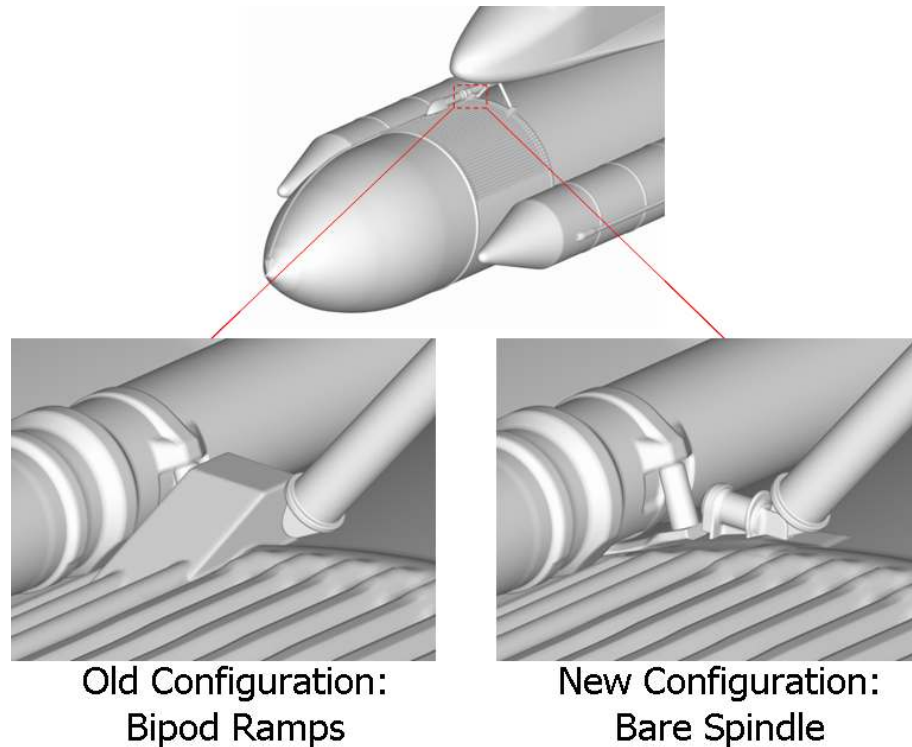
Figure 1.2. Comparison of surface geometries with and without the bipod ramps in the bipod attachment region.

local flowfield on the ET around the bipod affecting the flowfield on the liquid oxygen feedline and the separated region upstream of the fitting. Figure 1.6 details a computation showing the local flowfield changes caused by the ramp removal.

Heat transfer predictions were needed in this area for thermal modeling, but the OVER-FLOW code had never been tested for heat transfer predictions at supersonic speeds with SWTBLI's embedded in the flowfield. Several computations were done to assess the accuracy of the RANS solutions, including a Mach 4 case with the Spalart-Allmaras (SA) and the Shear Stress Transport (SST) turbulence models, the two models of choice for RANS computations in aerodynamic applications. Upstream of separation on the ET the velocity profiles from the two separate turbulence models match each other very well (within 5%), however in the separation zone the mean streamwise velocity profile showed a separation zone height with nearly a factor of two difference between the two turbulence model pre-

$$Y = -50"$$
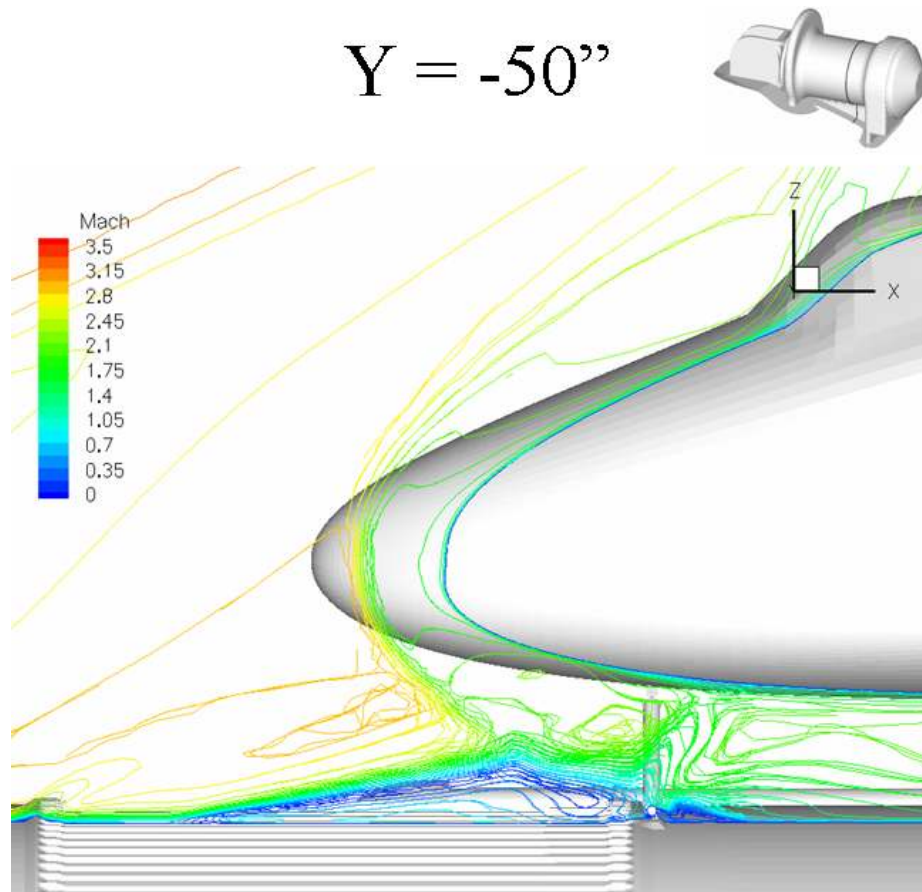
Figure 1.3. Flowfield cut through the bipod fitting attachment showing Mach contours of a M_{inf} = 3.5 case.

dictions. Figure 1.7 shows a similar computation at Mach 2.79. RANS simulations were done with the SA and SST models and the predicted surface pressure distributions were subtracted from each other to give the delta C_p between the two predictions. Large differences can be observed. There was no data available to validate the CFD with. The only available flight data was below Mach 2.5 (above this Mach number, and hence altitude, the pressures were lost in the noise of the system) and all the previous wind tunnel tests were done on configurations with simplified geometries instead of the actual bipod attachment fittings.
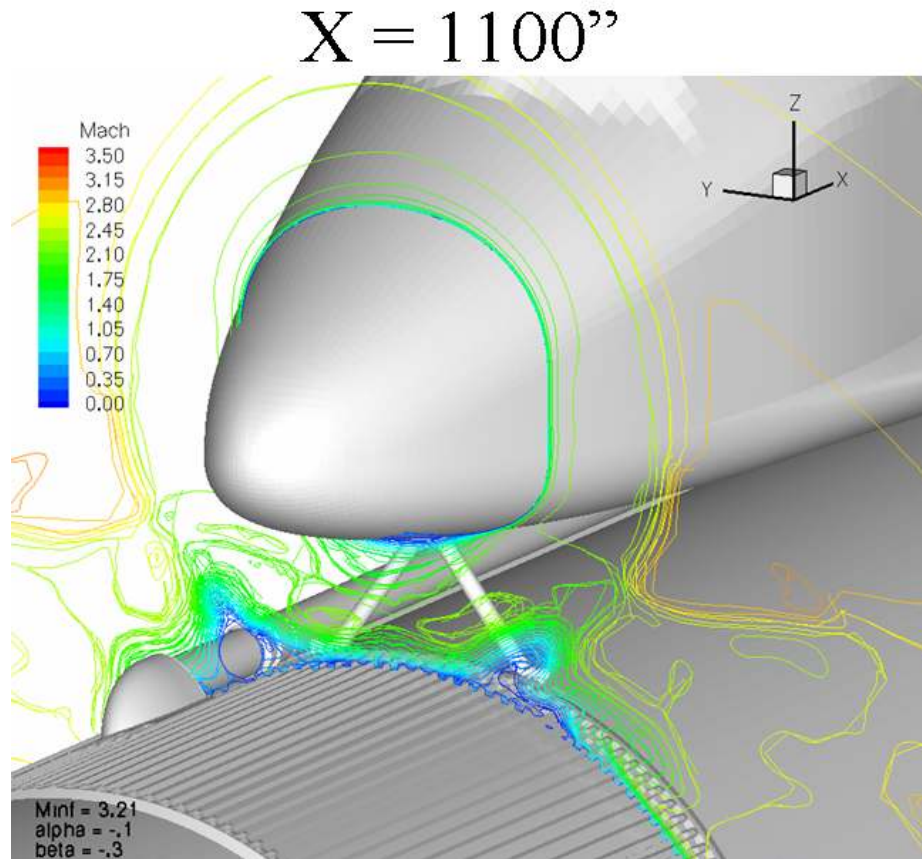
Figure 1.4. Constant axial cut through a M_{inf} = 3.5 case upstream of the
bipod attachment fitting.

Based on the uncertainty in the predictions discussed above, a simplified model of the
bipod attachment fitting was placed in a wind tunnel and tested in an attempt to simplify
the problem and test the turbulence models on a more controlled configuration. The bipod
attachment fitting was modified by smoothing out the shape to resemble a cylinder and
placing it on a flat plate. Although this configuration's flowfield did not resemble the flight
flowfield very accurately, it was used for CFD validation, nonetheless. The freestream
conditions were chosen to match a M_{inf} = 3.95 case. The simplified protuberance test
produced a very complicated flowfield with shocks intersecting each other and shock waves
interfering with a turbulent boundary layer.
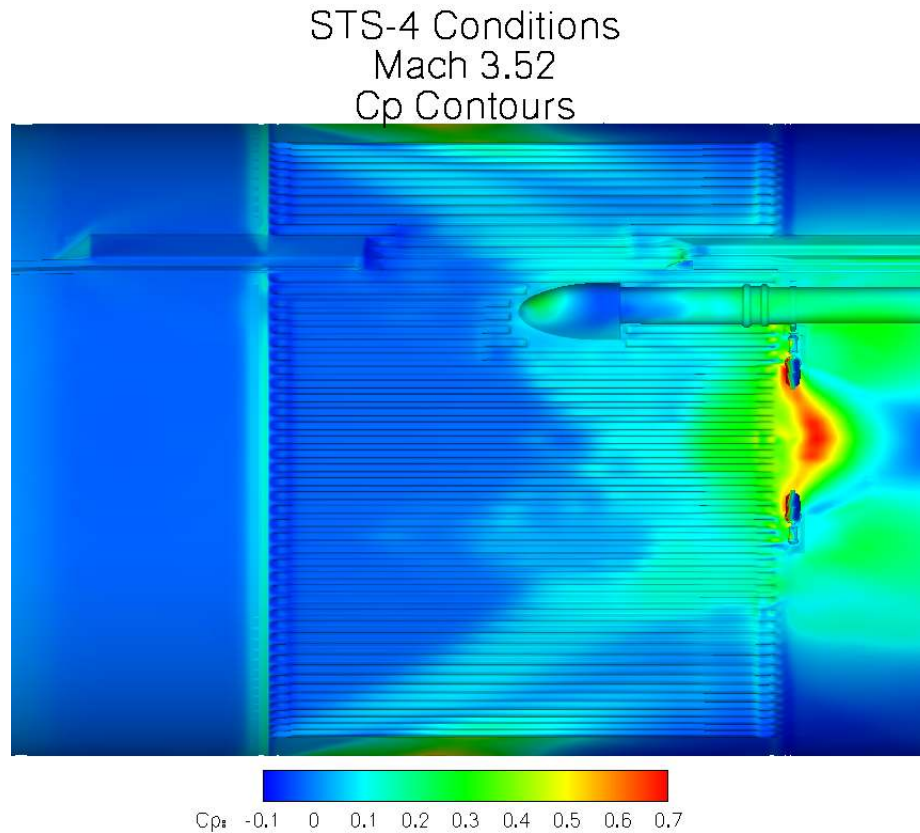
Figure 1.5. C_p contours on the ET for a $M_{\text{inf}} = 3.5$ case

The SA model underpredicts the extent of the separated region by approximately three inches ($\sim$40%) while the SST and the k-ω model only slightly underpredict separation ($\sim$5%). The SA predicts a larger pressure value, indicating a higher pressure on the protuberance. The k-ω and the SST models give very comparable pressure predictions, while the SA gives a much larger pressure prediction. The SA model predicted a higher peak pressure on the protuberance and a shorter separated region, which is consistent with the predictions for the full stack cases reported earlier.

The previous discussions highlights several reasons that heat transfer predictions from the CFD solutions were not used in design.

1. There was no heat transfer data on the correct configuration to validate against.
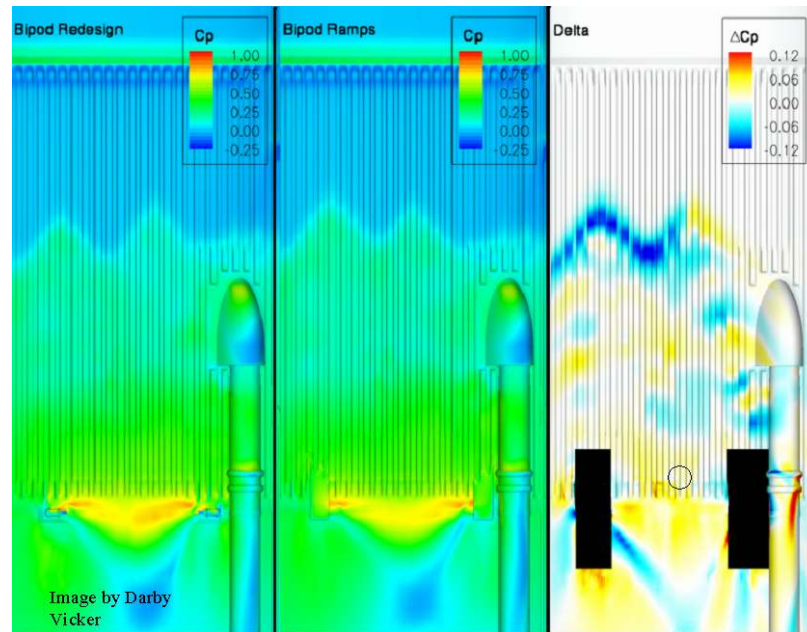
Figure 1.6. Delta C_p between the original bipod design with the foam ramps and the redesigned without the ramp.

2. The flight pressure data in the area of interest was inaccurate.

3. Previous computations at identical conditions with different turbulence models showed large variations in separation prediction, with no data to choose the correct model.

4. The simplified protuberance computations showed a large spread in the prediction of separation with the standard model of choice (SA) being less accurate than the SST model.

5. This type of computation had never been attempted in a situation where innacurate results could not be tolerated.

Instead of using the OVERFLOW code for heat transfer, a plan was implemented to provide the essential data needed for Return to Flight and to improve the validation database and the ability of RANS computations to predict SWTBLI. To improve the validation database and provide the design heating measurements around the bipod attachment
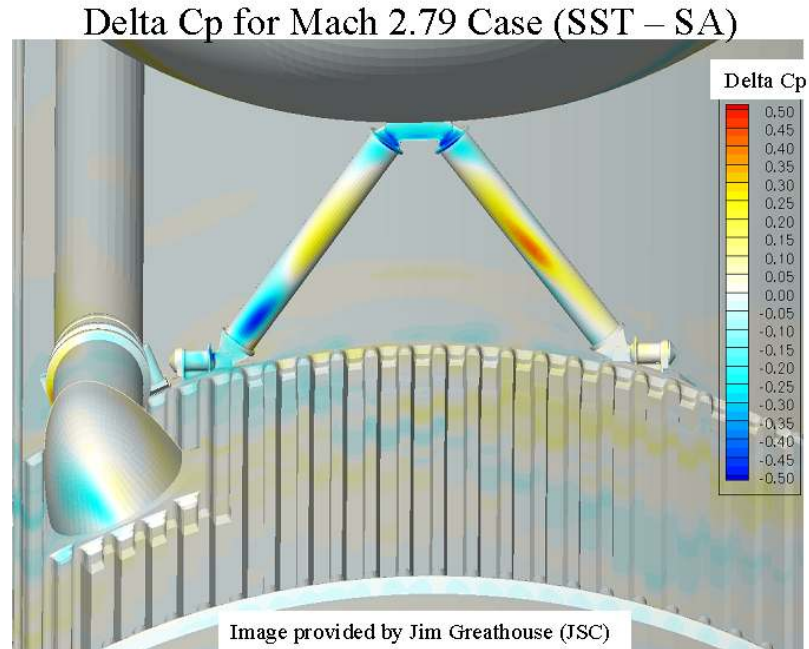
Figure 1.7. Difference between surface C_p values from SA and SST predictions of a $M_{\text{inf}} = 2.79$ case.

fitting, the Integrated Heating (IH)-108 wind tunnel test [2] was initiated at the Calspan University of Buffalo Research Center (CUBRC) facilities in Buffalo, NY. In parallel, the current effort to improve the turbulence models for SWTBLI's was initiated with the goal to provide engineering heating estimates for these types of interactions on the Space Shuttle Orbiter full stack configuration. Improvements to the existing models and new models will be explored in order to improve predictions inside the separated region. Although not part of this Dissertation, the database generated from the IH-108 wind tunnel test could be used to validate CFD predictions in this complicated region. Further validation on other historical configurations, such as X-33, X-38, Apollo, other vehicles or wind tunnel configurations will also be necessary to assess the robustness of any modifications or new models. For future vehicles, this CFD capability could reduce the number of expensive wind tunnel tests needed and reduce uncertainties in aerothermodynamic environments opening up more abort opportunities. The Multi Purpose Crew Vehicle (MPCV) is an excellent ex-

ample of this opportunity. The current uncertainty on turbulent heat transfer is very high, especially on the aft end where separation dominates the flowfield. If more accurate turbulent predictions were available, uncertainties on the turbulent heating would shrink opening up more margin for the thermal protection system. These turbulence model uncertainties not only affect the aerothermodynamics, but also the aerodynamic performance as well. The MPCV capsule has a large separated wake, which is extremely difficult to model with conventional turbulence models.

1.2 OVERFLOW Code Description

OVERFLOW [3, 4] is a structured (overset) grid, Navier-Stokes flow solver. It uses a finite-difference formulation, with flow quantities stored at the grid nodes. OVERFLOW has central- and Roe upwind-difference options, and uses a diagonalized, implicit approximate factorization scheme for time advancement. Local timestepping, multigrid techniques and grid sequencing are all used to accelerate convergence to a steady state. The standard turbulence models used by the OVERFLOW code are the one-equation SA model and the two-equation SST model. Other models available are the Baldwin-Lomax, k-ϵ and the k-ω. SA and SST are used for general aerodynamic applications within the OVERFLOW community.

OVERFLOW has recently been applied to supersonic and hypersonic flowfields by Olsen and Prabhu [5], Lillard and Dries [6], and Olsen et al. [7]. Lillard and Dries [6] evaluated the ability of the OVERFLOW code to capture laminar heating. For the flat plate, sphere, and X-38 forebody test cases, the error in the predictions of heat transfer was below 8%. Olsen et al. [7] computed several different turbulent flows with OVERFLOW, including a turbulent flat plate, ogive cylinder flare, overexpanded bell nozzle, and a Space Shuttle. Several turbulence models were used, including the SA, SST, k-ω, and lag models. Comparisons of heat transfer were made for the flat plate with the Van Direst II with Karman-Schoenherr law and were within 5-10%. For the ogive cylinder flare with low flare angles, the separation bubble was computed accurately, but as the flare angle approached

35 ° the predictions began to deviate from experiments. The separation bubble was under predicted and the reattachment heating was over predicted. Olsen et al. Olsen et al. [8] also applied the Lag model to massively separated flows, including two transonic and supersonic capsule flowfields. For these two flows, the Lag model provided more accurate predictions of experimental lift, drag, and pressure distributions for subsonic and supersonic flows.

1.3 Configurations Available for Comparison

Many simplified configurations cause SWTBLI's, but the flow of an oblique shock wave impinging on a turbulent boundary layer will be the flow of interest for this investigation. This phenomenon is present on the ET when the oblique shock emanating from the nose of the Space Shuttle Orbiter impinges on the ET. Therefore, the data obtained for comparison will focus on this test case. An accurate turbulent boundary layer upstream of the interaction is vital, thus turbulent flat plate data will be examined as well. Data for comparison can consist of wind tunnel data or DNS/LES computations, provided the quality is high. Flowfield quantities are a must, including mean properties and preferably turbulent quantities. Heat transfer, or at a minimum skin friction, is also required. In general, the higher Mach number cases are preferred and a test case that can be treated as 2D or axi-symmetric.

1.3.1 DNS/LES Computations

DNS calculations of a SWTBLI have been carried out by two groups. Gatski and Erlebacher [9] and Pirozzoli et al. [10] carried out simulations of a supersonic spatially evolving supersonic turbulent boundary layer before Pirozzoli et al. [11,12] did DNS simulations of an oblique shock impinging on a turbulent boundary layer. In addition, Spyropoulos [13] and Spyropoulos and Blaisdell [14] did LES simulations of the turbulent boundary layer flow.

In addition, work at Princeton University has been done by Wu and Martin [15] and Wu et al. [16] on a similar interaction as the one just detailed. These simulations have

been done to compare with direct measurements from a wind tunnel test currently being executed at Princeton University [17].

1.3.2 Wind Tunnel Tests

Although many excellent computational datasets exist, the preferred method is to compare the predictions to a wind tunnel test.Multiple reviews of SWTBLI test cases have been done, the most notable by Settles and Dodson [18], who were commissioned by NASA to identify and review the available experimental data for these interactions. Since this review, several others have been done, including Roy and Blottner [19] and Knight et. al. [20] to name a few. Recently, for NASA's Fundamental Aeronautics program, Brown [21] reviewed the literature and made recommendations on which tests to use for CFD validation.

Several wind tunnel tests have been carried out of a oblique shock wave impinging on a fully-turbulent boundary layer. Six wind tunnel cases have been identified as possible candidates for CFD validation. Settles and Dodson [18] reviewed three of these wind tunnel tests in their search for experimental data for CFD validation and gave recommendations on each. Brown [21] reviewed the three latter experiments and recommended them all for analysis.

The first set of experiments are those of Reda and Murphy [22, 23] and Rose and Johnson [24]. They tested a Mach 3 turbulent boundary layer in a rectangular channel with several different oblique shock strengths. The initial tests were affected by the turbulent boundary layers on the sidewalls, thus Reda and Murphy created a new shock-generation divide and reduced the size of the sidewall boundary layers by an order of magnitude [25, 26]. Settles and Dodson [18] analyzed the data and stated that the experimental setup was 'actually a 3-D interaction' and was 'too complex for a useful test case'. Settles and Dodson also remarked on Rose and Johnson [24] saying 'the level of this experiment is not up to current code-validation standards'. Reda [27] also pointed out that the experimental flowfield was indeed not two-dimensional and any prediction from a two-dimensional simulation would

have to be analyzed with that fact in mind. Therefore, this case will not be used in this analysis.

The second case considered are the experiments of Rose [28,29] and Rose and Childs [30]. They conducted experiments in an axi-symmetric wind tunnel with a $9°$ conical shock wave generator. Settles and Dodson [18] state that 'serious questions have arisen about the accuracy of these hot-wire data'. In addition, no apparent CFD calculations have been done for this configuration. Although the axi-symmetric configuration and data available would make this an ideal case for CFD validation, the lack of quality data makes this an unusable test case.

The third case considered is from Horstman and Owen [31]. They first tested a $10°$ cone-ogive-cylinder at the Ames 3.5 ft. Hypersonic Wind Tunnel to measure turbulent mean flow properties. From this data they were also able to compute turbulent shear-stress, eddy-viscosity, mixing-length, heat-flux, and turbulent Prandtl-number distributions. Owen et al. [32] measured mass-flow and total temperature fluctuations for the same configuration. This experimental configuration was used for many other test programs in which more complicated geometries such as a flare, a skewed flare, and an axi-symmetric impinging shock. Kussoy and Horstman [33] and Horstman et al. [34] detail the axi-symmetric impinging shock system. The experimental data includes wall pressure, skin friction, Stanton number, and mean flow velocity, density, and static pressure profiles for two different oblique shock angles. Mikulla and Horstman [35] detail turbulent intensity and Reynolds shear stress measurements for both oblique shock angles. Settles and Dodson [18] recommend this case for CFD validation.

Several groups have computed this flowfield, including Horstman et al [34], Coakley et al. [36], Viegas and Coakley [37], and Vuong and Coakley [38]. In addition, this test case was used in the 1980-81 AFOSR-HTTM-Stanford Conference on Complex Flows [39]. The majority of the computations did not accurately predict the C_f values, especially downstream of reattachment. In particular the peak C_f values were over predicted by the computations.

Although this test case has been shown to be very popular, it will not be chosen here due to inconsistencies discovered when attempting to run the entire geometry instead of just a portion of it, like most previous analysis was done. It is this author's opinion that more of the wind tunnel geometry needs to be modeled in order to accurately model the cone-ogive-cylinder with the shock generation ring.

Brown [21] recommends three distinct datasets for analysis. The first, which is the one chosen here for analysis, is that of Schulein [40, 41], who conducted a ($M_\infty = 5$) wind tunnel test in the DLR Gottingen Ludwieg Tube facility, using air as the test gas. The measured values included wall pressure, skin friction (by an oil-flow technique), and wall heat transfer (infrared camera measurements and semi-infinite wall gages). Schulein tested four configurations, starting from a 2D nominal zero-pressure gradient flat plate boundary layer and then adding a shock generator with 3 different angles. An issue that plagues most cases that have this configuration is the shock generator is not relatively "long" compared to the nominal boundary layer thickness. This allows the expansion waves that emanate from the tail of the shock generator to interfere with the separation region, making the interaction more complex and not allowing for the various topological features of the SWTBLI flowfield to develop. Schulein was able to have a $\frac{L_{gen}}{\delta_0} \approx 1000$, which is a large enough ratio to provide ample space for the interactions to set up.

Brown [21] has identified two other high quality experimental datasets that could be used. One dataset is the Mach 8.9 experiment of Murray [42–44] which was conducted at the Imperial College Nitrogen gun tunnel. This test series consists of a hollow axisymmetric cylinder with an axisymmetric cowl use as a shock ring generator. Data available for this case are wall pressure and heat flux. The second experiment is the Mach 8.18 experiment of Kussoy and Horstman [45]. It was conducted on a 2D flat plate in the no longer operational NASA Ames Research Center Hypersonic facility. The test configuration was the nominal 2D flat plate with a shock generator inclined, similar to the Schulein configuration assessed in this study. Pressure, skin friction, and heat flux were obtained in this study as well as flow field quantities (no turbulence quantities) were obtained.

1.4 Objectives of the Proposed Research

The primary goal of the proposed research is to improve the turbulence modeling for compressible flows, including flows with SWTBLI's or massive separation. At first, we assess the current state of standard turbulence models in the prediction of SWTBLI's. Then we propose a new model to better capture the desired flow phenomenon. Of specific interest is a new model that incorporates the history effects seen when abrupt adverse pressure gradients are introduced into the flowfield. This will be executed by first comparing CFD predictions to four simplified test cases in order to assess the models and choose modeling constants. These configurations are an incompressible turbulent flat plate [46, 47], incompressible turbulent mixing layer [48], incompressible turbulent separated boundary layer [49], and a transonic bump flow [50]. The lessons learned for these test cases will then be applied to a SWTBLI [40, 41] and a massively separated transonic capsule flowfield [51, 52]. Both of these flows are of interest to NASA Johnson Space Center.

1. Implement the Reynolds stress lag model in a form that is consistent with existing experimental data and correlations.

2. Compare Reynolds stress lag model to existing one- and two-equation turbulence models along with the lag model to determine the most applicable turbulence model for SWTBLI and massively separated flows.

2. Turbulence Modeling

Wilcox [53] reviewed numerous shock wave/turbulent boundary layer predictions [54–58] and came up with the following conclusions from nearly every prediction:

1. The turbulence models do not predict the measured starting location of adverse pressure gradient flow.

2. In the separation bubble, the predicted surface pressure is too high.

3. Downstream of the reattachment point the heat transfer and C_f are too high.

4. Downstream of reattachment, the velocity profiles indicate flow within the boundary layer decelerating more than experiments show.

Marshall and Dolling [59] examined several computations for highly separated compression ramps and noted the accuracy of the predictions was generally poor for any turbulence model. They noted that the upstream influence was not correct, the wall pressure rise through separation was too steep, and the pressures under the separated shear layer were too high. These are the same general conclusions as Wilcox. In an effort to separate time-dependent experimental behavior from the steady two-dimensional analysis, they executed a wind tunnel test in a Mach 5 flow for a $28°$ compression ramp. They concluded that the flow was two-dimensional, but a low-frequency oscillation of the separation shock was evident. Thus any computation with the separation shock fixed in space misses the physics of the problem, i.e. a translating shock front affecting the upstream flow. This phenomenon could be responsible for the incorrect prediction of the starting location of the adverse pressure gradient flow. Brusniak and Dolling [60] noted the same oscillation for three-dimensional flowfields.

Knight and Degrez [61] conducted an assessment of 2-D and 3-D shock wave boundary layer interactions using nearly 20 researchers around the world. Their computations

involved hollow cylinder flares (2-D) and single and double fins (3-D). The general conclusions of the assessment were that Large Eddy Simulations (LES) must be used if the fluctuating pressure and heat transfer loads were to be calculated. These fluctuating loads can be very significant in shock wave/boundary layer interactions. They also stated that for turbulence modeling to be successful, accurate experimental data for flowfield Reynolds stresses, flowfield turbulent heat flux, and wall pressure and heat transfer fluctuations are necessary. Knight et al. [20] broadened the test cases from the 1998 analysis and compared DNS, LES, and RANS calculations to experiments. Their general conclusions were that new strides in RANS simulations accounting for weak nonlinearity (realizability) had improved the simulations enough so they had started to predict flowfield features more accurately. The weakly nonlinear Wilcox-Durbin [62] and Thivet [63] models both successfully predicted secondary separation on a 3-D fin, which had not been done before with RANS. They recommend continued emphasis on weakly nonlinear corrections to the two-equation models. The DNS and LES methods are still limited, because detailed comparisons to experiment can not be done based on the lower Reynolds number limitations of the simulations. To date, neither DNS, LES, or RANS models have successfully predicted surface heat transfer in strongly separated shock wave turbulent boundary layer interactions. The mismatch between the DNS and LES predictions could be due to the Reynolds number not being identical to the computations.

Several researchers have had difficulties getting improved results with Reynolds stress models. Rizzetta [64] evaluated three popular explicit algebraic Reynolds-stress (EARS) models for separated supersonic flows, a shock impinging on turbulent boundary layer and a compression ramp. He compared these results to the k-ϵ model. The results consistently showed that the EARS models offered little improvement over standard RANS approaches using the Boussinesq approximation. Viti et al. [65] showed similar results for the Reynolds stress-transport turbulence models.

2.1   Nonequilibrium Turbulence Modeling Review

Past work has shown that one- and two-equation models do not predict turbulent separation or the reattachment properties of a Shock Wave Turbulent Boundary Layer Interaction (SWTBLI) correctly. It is proposed that a main cause of this inaccuracy of the predictions in the separated regions is the effect of flow history. In other words, the Boussinesq approximation relates mean strain rates directly to the Reynolds stress tensor (RST). Thus any change in the strain rate is instantly accounted for in the RST. In reality, there is a time lag between changes in the strain rate and changes in the RST when the turbulence is not in equilibrium. Turbulent flows deviate from equilibrium conditions when large adverse pressure gradients are present. The standard one- and two-equation turbulence models have been designed and tuned to accurately predict equilibrium flows, such as zero-pressure gradient boundary layers and free shear layers.

Clauser [66] proposed that a boundary layer is in equilibrium if the pressure gradient parameter

$$\beta = \frac{\delta^*}{\tau_w} \frac{dP_o}{dx} \tag{2.1}$$

is a constant. When boundary layers are in equilibrium, they are self-preserving, i.e. when properly scaled, the wake portions of the velocity profile for two different boundary layers with the same value of β are identical, even if their Reynolds numbers are different. Equilibrium boundary layers have the characteristic that the turbulent time scales are much smaller than the mean flow time scales so the turbulence can react quickly to these slowly changing mean flows.

Turbulence models for nonequilibrium flows have been proposed, with the simplest being modifications to algebraic eddy viscosity models. Horstman [67] proposed a modified algebraic eddy viscosity model corrected for variable pressure gradient effects. This method relaxes the modeling constants in the algebraic eddy viscosity model based on nonequilibrium effects through a constant, the lag parameter, and a pressure gradient parameter similiar to Clauser's. The constants modeled were the van Driest damping parameter, A^+, and the von Karman constant, κ. Rose and Johnson [24] and Shang and Han-

key [68] proposed slightly different models that use an exponential expression to include history effects into the algebraic eddy viscosity parallel to the wall. Deiwert [69] used a similiar relationship but the calculations were done along streamlines instead. These exponential expressions use roughly between 5 and 15 boundary layer thicknesses as the relaxation length.

The most notable nonequilibrium turbulence model is the Johnson-King model [70, 71], which is considered a half equation model. The model solves an ordinary differential equation for the development of the maximum Reynolds shear stress through an iteration process. This model performs well for two-dimensional flows with rapid changes in the streamwise pressure gradient. However, it performs poorly when the flow is in equilibrium, most notably for attached flows. The model seems to overemphasize nonequilibrium effects in regions where the flow is in equilibrium. Ahmed and Tannehill [72, 73] modified the Johnson-King model to remove the iterative solution process and improved the model to better capture equilibrium flows. Abid et al. [74] extended the Johnson-King model to three dimensions. Despite these modifications, the Johnson-King model did not become accepted in the community as a viable option for turbulence modeling due to limited robustness and range of applicable flow cases.

Reyhner [75] formulated a differential lag relationship for the eddy viscosity of the form

$$\frac{d\mu_t}{dx} = \frac{k_3}{\delta} \left(\mu_{teq} - \mu_t \right). \tag{2.2}$$

The lag constant, k_3, was set to 0.5. Lee et al. [76] modified the above relationship to account for bleeding off the boundary layer. The equation was added to the turbulent boundary layer equations and solved at a given marching distance. Equilibrium values were calculated from the Cebeci-Chang [77] algebraic turbulence model. Boundary layer profile shapes improved dowstream of the bleed slot.

Knight and Saffman [78] developed a Reynolds stress relaxation model that derives the RST from a non-linear stress-strain relationship instead of the Boussinesq approximation. Their relaxation equations contain diffusion terms, and include a "gyroscopic stability" term to account for rotation effects.

Speziale and Xu [79] tested a model on homogenous shear flow that uses the Reynolds anisotropy tensor. Speziale and Xu credit the idea to Saffman **??**, who implemented this relaxation algebraically on the Reynolds Stress Tensor. Radhia et al. [80] follow a similar approach as Speziale and Xu. They also did calculations in homogenous shear flow.

Hamlington and Dahm [81, 82] have derived a model similar to our proposed lagRST model in which they use the Reynolds anisotropy tensor (similar to the version discussed above). However, instead of numerically solving the lag equation, they solve the lag equation along a streamline, reducing it to an ordinary differential equation. They assessed several homogenous flows and have done work on flat plates and the interaction of an impinging oblique shock wave with a turbulent boundary layer.

Churchfield and Blaisdell [83] used a similar definition of the lagRST model discussed above, but used the 2006 $k-\omega$ formulation to define ν_{teq}. Churchfield and Blaisdell [84,85] then went on to use a previous version of the lagRST formulation with the OVERFLOW code provided by Lillard and Olsen to assess wingtip vortex flow.

2.2 Lag Model

Olsen and Coakley [5] proposed a new turbulence model to account for the inability of two-equation turbulence models to directly describe nonequilibrium effects, which are encountered in large pressure gradients involving separation and shock waves. These effects are only important when the turbulent time scales are much larger than the time scale of the mean strain. This new model can capture more of the non-equilibrium effects without invoking a full Reynolds stress model. It is formed by taking a baseline two-equation model and coupling it with a third equation (lag equation) to model the nonequilibrium effects in the eddy viscosity. This class of models essentially introduces a lag into the response of the eddy viscosity to rapid changes in the mean flowfields, which is the character of the response seen experimentally. By lagging the third equation it gives the turbulence model an extra degree of freedom without affecting accurate equilibrium flow predictions.

Olsen et al. [7] did further comparisons with the 2001 version of the lag model and slightly modified it to its current state. The revised model is

$$\frac{\partial \rho k}{\partial t} + \frac{\partial}{\partial x_k}\left(\rho u_k k - [\mu + \sigma_k \mu_t]\frac{\partial k}{\partial x_k}\right) = \mathcal{P}_k - \epsilon_k \tag{2.3}$$

$$\frac{\partial \rho \omega}{\partial t} + \frac{\partial}{\partial x_k}\left(\rho u_k \omega - [\mu + \sigma_\omega \mu_t]\frac{\partial \omega}{\partial x_k}\right) = \mathcal{P}_\omega - \epsilon_\omega \tag{2.4}$$

$$\frac{\partial \rho \nu_t}{\partial t} + \frac{\partial}{\partial x_k}\left(\rho u_k \nu_t\right) = a_0 \rho \omega \left(\nu_{t_{eq}} - \nu_t\right) \tag{2.5}$$

where:

$$\nu_{t_{eq}} = k/\omega \qquad\qquad \mathcal{P}_\omega = \alpha \rho S^2$$

$$\mathcal{P}_k = \tau_{ij} s_{ij} \qquad\qquad \epsilon_\omega = \beta \rho \omega^2$$

$$\epsilon_k = \beta^* \rho k w \qquad\qquad S = \sqrt{2\left(s_{ij}s_{ij} - s_{kk}^2/3\right)}$$

$$\tau_{ij} = -\rho\left(\frac{2}{3}k\delta_{ij} - \nu_t(2s_{ij} - \frac{2}{3}s_{kk}\delta_{ij})\right) \qquad s_{ij} = \frac{1}{2}\left(\frac{\partial u_i}{\partial x_j} + \frac{\partial u_j}{\partial x_i}\right)$$

with parameters

$$a_0 = 0.35 \qquad\qquad \beta = 0.075 \qquad\qquad \sigma_k = 1.5$$

$$\alpha = 5/9 \qquad\qquad \beta^* = 0.9 \qquad\qquad \sigma_e = 0.5.$$

Equation 2.5 governs the turbulent viscosity. The turbulent viscosity goes to its equilibrium value along a streamline like any first order dynamical system with a time constant of $1/(a_0\omega)$. By having no diffusion term, the evolution of the turbulent viscosity is driven by its upstream history and the equilibrium value of turbulent viscosity at that point.

Originally, the lag model had a function of the form

$$a(R_T) = a_0 \frac{R_T + R_{To}}{R_T + R_{T\inf}} \tag{2.6}$$

with $R_{To} = 1$ and $R_{T\inf} = 0.01$ on the right hand side to determine the amount of "lag" in the third equation. This function was deemed unnecessary, in fact slightly more accurate results were obtained by setting a equal to the constant a_o. The constant a_o controls the amount of lag in the equations, with a higher value giving the system a shorter time constant thus driving the model to equilibrium values quicker. This value was determined in

the original formulation by running the model on simple test cases where nonequilibrium effects were evident. It is the one added modeling constant. With the updated implementation, Olsen also modified the value of σ_k to go from 0.5 to 1.5. The authors made this change thinking it was only cosmetic in that it only rounded the turbulent / non-turbulent edge of the boundary layer. Recently, Olsen [86] again changed the constant σ_k to 0.8. This is now referred to as the "standard Lag model". The sensitivity of the solution to a_0 and σ_k will be explored.

Olsen et al. showed that the lag model gave comparable results to other standard turbulence models (if not better) for the cylinder-flare flowfield. The model still suffered from an over-prediction of reattachment heating by about 10-15% and an underprediction of separation. Another application involved an overexpanded bell nozzle flow. The lag model, when run in time accurate mode, predicted a separation position much more accurate than other models.

The Lag model was implemented in OVERFLOW using a 2nd order upwind method with a min-mod limiter to discretize the turbulence equations. Other 2-equation models within OVERFLOW are implemented with a 1st order scheme. The authors explain that they initially implemented 1st order, but ran into grid convergence issues for separated flow cases and found that the 2nd order scheme brought the grid density needs back in line with the requirements for the nominal 2-equation models already in OVERFLOW. Olsen and Coakley go on to explain that this increase in order is due to the lag equation which implements the history effects of the model. If a 1st order scheme was used, this would be analogous to using a 1st order time integrator to integrate an ODE, with grid spacing analogous to the ODE time size step.

2.3   LagRST Model

To capture more nonequilibrium turbulent effects without invoking a Reynolds stress model, Olsen and Coakley [5] propose lagging the Reynold's stresses instead of the eddy viscosity,

$$\frac{D\tau_{ij}}{Dt} = a_0\omega \left(2\nu_{t_{eq}}s_{ij} - \tau_{ij}\right). \tag{2.7}$$

This model, referred to as the lagRST model, would be an alternative to an algebraic stress model to capture some history effects seen in three-dimensional flows. No new terms are introduced, as in Reynolds stress modeling. A few modifications can be done to the proposed model to improve the formulation. The baseline formulation will use the same equations to define the equilibrium values of k and ω as the lag model did, equations 2.3 and 2.4.

The main form of the equations will lag the Reynolds stress, τ_{ij}, defined as

$$\tau_{ij} = -\bar{\rho}\widetilde{u_i'v_j'}. \tag{2.8}$$

By using a form very similar to equation 2.7, the lag equation for τ_{ij} is

$$\frac{\partial \tau_{ij}}{\partial t} + \frac{\partial}{\partial x_k}(\tau_{ij}\tilde{u}_k) = a_o\omega \left(\tau_{ij_{eq}} - \tau_{ij}\right), \tag{2.9}$$

where $\tau_{ij_{eq}}$ is defined by

$$\tau_{ij_{eq}} = -\rho \left[\frac{2}{3}k\delta_{ij} - \nu_{t_{eq}}\left(2s_{ij} - \frac{2}{3}s_{kk}\delta_{ij}\right)\right]. \tag{2.10}$$

By lagging the Reynolds stress tensor and coupling that to equation 2.3, the kinetic energy equation, there are two equations for the turbulent kinetic energy. This is due to the following relation,

$$\tau_{kk} = -\bar{\rho}\widetilde{u_k'u_k'} = -2\bar{\rho}k. \tag{2.11}$$

Thus, for this formulation, the turbulent kinetic energy used in the flowfield must come from the trace of the Reynolds stress tensor and k derived from equation 2.3 will only be used in the equilibrium calculations.

2.3.1 Lagging the Reynolds Stress Tensor using Menter's SST

An implementation of the LagRST model using Menter's SST model [87] to provide the equilibrium values of k and ω was also implemented.

$$
\frac{D\rho k}{Dt} = \tau_{ij}\frac{\partial u_i}{\partial x_j} - \beta^*\rho\omega k + \frac{\partial}{\partial x_j}\left[(\mu + \sigma_k\mu_t)\frac{\partial k}{\partial x_j}\right] \tag{2.12}
$$

$$
\frac{D\rho\omega}{Dt} = \frac{\gamma}{\nu_t}\tau_{ij}\frac{\partial u_i}{\partial x_j} - \beta\rho\omega^2 + \frac{\partial}{\partial x_j}\left[(\mu + \sigma_\omega\mu_t)\frac{\partial \omega}{\partial x_j}\right]
$$

$$
+2\rho\left(1 - F_1\right)\sigma_{\omega 2}\frac{1}{\omega}\frac{\partial k}{\partial x_j}\frac{\partial \omega}{\partial x_j} \tag{2.13}
$$

The modeling constants and blending functions used were not modified and therefore can be found in Menter [87]. The turbulent eddy viscosity was calculated the standard way, Where ν_t is defined as

$$
\nu_{t_{eq}} = \frac{a_1 k}{max\left(a_1\omega; \Omega F_2\right)} \tag{2.14}
$$

This was then substituted into equation 2.10 to obtain $\tau_{ij_{eq}}$.

2.3.2 Numerical Method

Each of the previously discussed models were implemented into version 2.0aa of the OVERFLOW code. OVERFLOW [3, 4] is a structured (overset) grid, Navier-Stokes flow solver. It uses a finite-difference formulation, with flow quantities stored at the grid nodes. OVERFLOW has central- and Roe upwind-difference options, and uses a diagonalized, implicit approximate factorization scheme for time advancement. Local timestepping, multi-grid techniques and grid sequencing are all used to accelerate convergence to a steady state. The standard turbulence models used by the OVERFLOW code are the one-equation SA model and the two-equation SST model. Other models available are the Baldwin-Lomax, k-ϵ and the k-ω. SA and SST are used for general aerodynamic applications within the OVERFLOW community. The full Navier Stokes equations were solved for all solutions.

The turbulence models were spatially discretized as specified in the original Lag model paper, with a 2nd order operator. This choice will be assessed on the chosen test cases. It is worth noting that Menter [88] implemented a third-order upwind difference, a second-order TVD, and a first order scheme in his initial studies of 2-equation models. He found that the solutions were virtually independent of the spacial discretization. Menter goes onto explain that this is due to the convective terms not being the leading order error term.

2.4   Summary of Proposed Models

In all the following tables, the models will be referred to as 905, 906, 907, and 909, the respective turbulence modeling option number in the input file. The following table has the model number along with the lag variable and the respective equilibrium description of that variable.

Model number	lag variable	equilibrium variable
903	ν_t	$\nu_{t_{eq}} = \frac{k_{eq}}{\omega_{eq}}$
905	$\tau_{ij} = -\bar{\rho}\widetilde{u_i' v_j'}$	$\tau_{ij_{eq}} = -\rho \left(\frac{2}{3} k \delta_{ij} - \nu_{t_{eq}} (2s_{ij} - \frac{2}{3} s_{kk} \delta_{ij}) \right)$ $\nu_{t_{eq}} = \frac{k_{eq}}{\omega_{eq}}$, defined from Lag Model
906	$\tau_{ij}^D = \tau_{ij} - \frac{1}{3}\tau_{kk}\delta_{ij}$	$\tau_{ij_{eq}}^D = 2\nu_{t_{eq}} s_{ij}^D$
907	$b_{ij} = \frac{\tau_{ij} - \frac{1}{3}\tau_{kk}\delta_{ij}}{2\bar{\rho}k}$	$b_{ij_{eq}} = -\frac{\nu_{t_{eq}} s_{ij}^D}{\bar{\rho}k}$
908	ν_t	$\nu_{t_{eq}} = \frac{a_1 k_{eq}}{max(a_1 \omega_{eq}; \Omega F_2)}$
909	$\tau_{ij} = -\bar{\rho}\widetilde{u_i' v_j'}$	$\tau_{ij_{eq}} = -\rho \left(\frac{2}{3} k \delta_{ij} - \nu_{t_{eq}} (2s_{ij} - \frac{2}{3} s_{kk} \delta_{ij}) \right)$ $\nu_{t_{eq}} = \frac{a_1 k_{eq}}{max(a_1 \omega_{eq}; \Omega F_2)}$, defined from SST

Table 2.1 Lag Variables

These lag variables are then the quantities operated on by the lag transport equation and the equilibrium values are the quantities the lag variables are relaxed towards.

Model number	Transport Equation
903, 908	$\frac{\partial \rho \nu_t}{\partial t} + \frac{\partial}{\partial x_k}\left(\rho u_k \nu_t\right) = a_o \rho \omega \left(\nu_{t_{eq}} - \nu_t\right)$
905, 909	$\frac{\partial \tau_{ij}}{\partial t} + \frac{\partial}{\partial x_k}\left(\tau_{ij}\tilde{u}_k\right) = a_o \omega \left(\tau_{ij_{eq}} - \tau_{ij}\right)$
906	$\frac{\partial \tau_{ij}^D}{\partial t} + \frac{\partial}{\partial x_k}\left(\tau_{ij}^D \tilde{u}_k\right) = a_o \omega \left(\tau_{ij_{eq}}^D - \tau_{ij}^D\right)$
907	$-\frac{\partial \bar{\rho}b_{ij}}{\partial t} + \frac{\partial}{\partial x_k}\left(\bar{\rho}b_{ij}\tilde{u}_k\right) = a_o \omega \left(\bar{\rho}b_{ij_{eq}} - \bar{\rho}b_{ij}\right)$

Table 2.2 Transport equations

3. Test Cases

Four test cases were chosen to test the implementation of the lagRST models and to calibrate the single constant, a_o, previously derived by Olsen and Coakley [89] as 0.35 and to confirm the σ_k value obtained by Olsen et al. [7]. In addition, multiple other turbulence models were ran for comparison purposes including the Spalart-Allmaras, Baldwin Barth, k-ω 1998, SST, and lag models. Although the $k - \omega$ model is not a standard model chosen anymore due to known freestream dependencies, it will be assessed here for comparison because it is the base model for the Lag model and the majority of the lagRST models. Table 3.1 lists the set of turbulence models that are referred to by number instead of name in some of the upcoming figures. The associated number is also the turbulence model designator within the OVERFLOW code.

Model Number	Turbulence Model
102	Spalart Allmaras
202	k-ω
203	SST
304	Lag
903	Lag model with Reynolds Stress Tensor Implementation
905	lagRST - τ_{ij} using k-ω for equilibrium values
909	lagRSTSST - τ_{ij} using SST for equilibrium values

Table 3.1 Table of turbulence models and their associated reference numbers in the OVERFLOW code

The four test cases chosen were the incompressible flat plate of Osterlund [46] and Osterlund et al. [47], adverse pressure gradient boundary layer of Driver [49], incompressible

mixing layer of Bell and Mehta [48], and a transonic bump flow by Bachalo and John-son [50].

Special care will be taking in assessing the entire boundary layer profile when the data is available, especially the profile near the edge. This region of the boundary layer has a large affect on re-attachment and/or impingement, but it is often ignored in the validation of models.

3.1 Incompressible Flat Plate

Osterlund [46] and Osterlund et al. [47] obtained zero pressure gradient turbulent bound-ary layer data in the Minimum Turbulence Level or Marten Theodore Landahl (MTL) wind-tunnel at the Department of Mechanics, Royal Institute of Technology(Swedish: Kungliga Tekniska hgskolan, abbreviated KTH). The data was taken on a 7 meter flat plate, with instrumentation locations ranging from 1.5 to 5.5 meters. Fluctuating velocity components and the fluctuating wall-shear stress were measured. Re_θ ranged from 2500 to 27000 with freestream velocities ranging from 10 to 50 m/s. All velocity profile comparisons were done at $x = 5.5m$.

This test case was first chosen to verify three things

1. The lagRST models were implemented correctly and give nearly identical results to their base models and / or show no effects of nonequilibrium turbulence

2. The lagRST model's ability to predict the near wall portion of the turbulent boundary layer (law of the wall)

3. The model's ability to predict the wake portion of the turbulent boundary layer

To compare velocity profiles, all the models were independently shifted so they matched the experimental value of θ at x = 3.5 meters. The velocity profiles were then compared at x = 5.5 meters in the shifted coordinate space.

During the course of this study, it was discovered that an exhaustive study of the effect of σ_k had not been done in the original lag model formulation. Since the formulation of

the original lag model, three values had been proposed for the value of σ_k, 0.5, 0.8 and 1.5. Although previously thought to only be a cosmetic change, the value of σ_k makes a substantial difference on the edge of the boundary layer. In addition, a_o will be assessed for values of 0.35 and 0.2. The value of 0.35 is the standard defined by Olsen and Coakley [5].

3.1.1 Grid Convergence

The grids generated were cartesian using geometric spacing in the off-body direction. The nominal grid chosen (referred to as the medium grid) had 92 streamwise points and 129 points in the boundary layer. The grid was extended well beyond the boundary layer edge to remove any boundary condition effects. The wall spacing chosen gave a y^+ less than 0.15 across the plate. To create the coarse and fine grids, both grid dimensions were scaled by $\sqrt{2}$ to increase the total grid dimension by a factor of 2. The wall spacing was then changed proportionally. This gave grids with dimensions of 65 by 91 and 129 by 182.

Figure 3.1 shows the results for the lagRST model with the standard coefficients (a_o= 0.35, σ_k = 0.8). The profiles converge fairly well until you get to the edge of the boundary layer. The finer the grid, the larger the bump in the velocity profile gets and the closer the profile gets to having an inflection in the boundary layer.

Figure 3.2 presents skin friction verse Re_θ for the same set of solutions. Although the change between grids is on the order of 1%, the fact that the fine grid difference is getting larger indicates an issue with this choice of constants. If the value of σ_k is increased to 1.5, the discrepancy at the edge goes away.

Figure 3.3 and 3.4 show the same set of plots for the lagRST model with $\sigma_k = 1.5$. The coefficient change vastly improves the grid convergence. There is a minimal difference between the medium and fine grids.

Figure 3.5 and 3.6 show the worst cases for grid convergence for the lagRST model, $\sigma_k = 0.5$. There is no grid convergence for this case near the edge of the boundary layer and the skin friction diverges with increasing grid resolution.
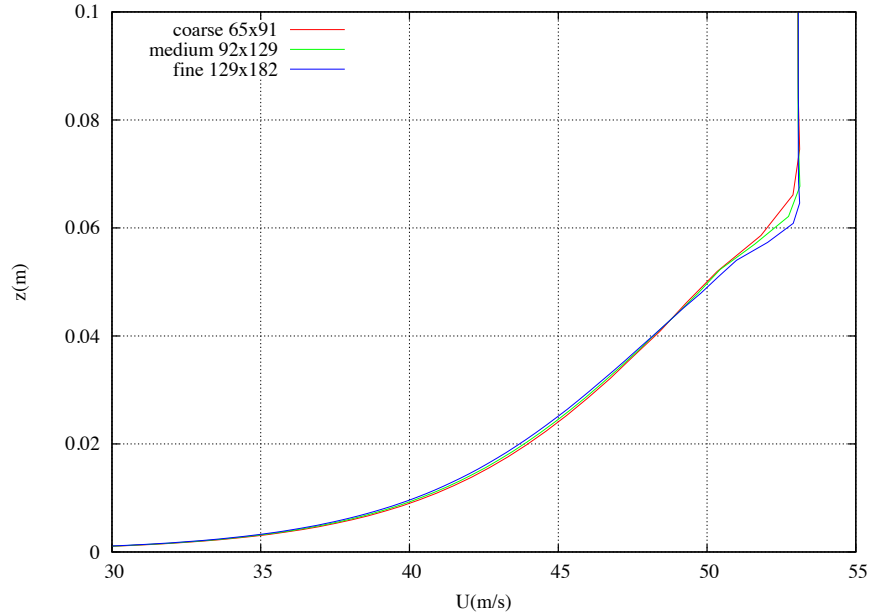
Figure 3.1. Velocity profiles for lagRST showing the effects of varying grid dimensions

At this point it is worth assessing the affects of the first order convective terms on the turbulence model and grid convergence. Figure 3.7 shows the effects of grid convergence on the velocity profile when the solution is ran with 1st and 2nd order convective terms. It is clear that the second order solution has a larger inflection near the edge of the boundary layer than the 1st order. This effect will be explored in the following sections.

Figure 3.8 and 3.9 show the same set of plots for the SST model. For both pots, the medium and fine grids provide virtually identical answers. A grid independent solution is obtained with the medium grid.
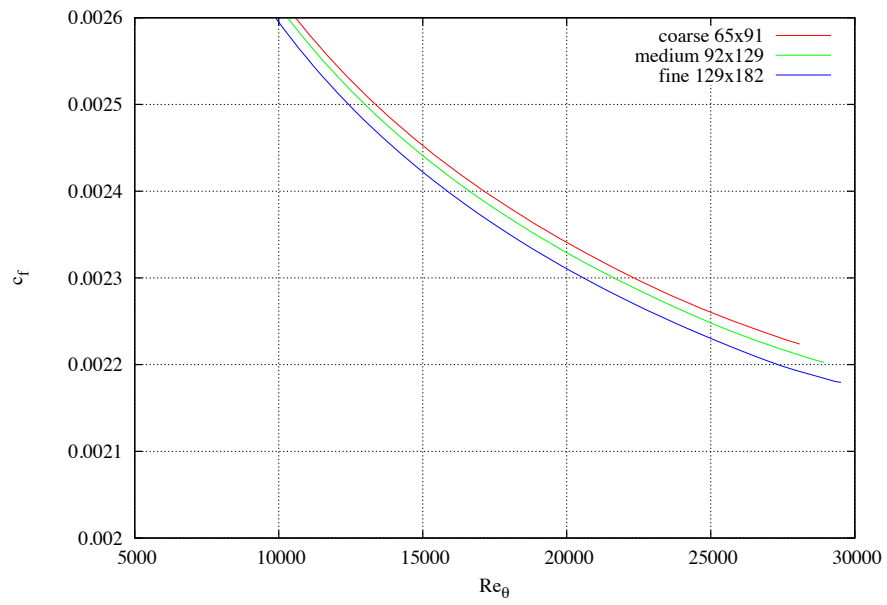
Figure 3.2. Skin friction profiles for lagRST showing the effects of varying grid dimensions
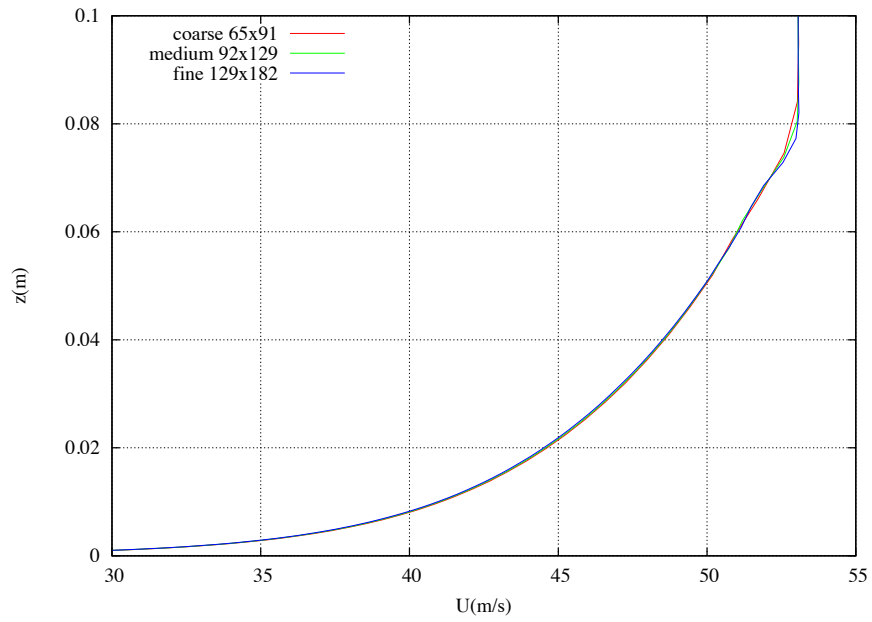
Figure 3.3. Velocity profiles for lagRST with $\sigma_k = 1.5$ showing the effects of varying grid dimensions
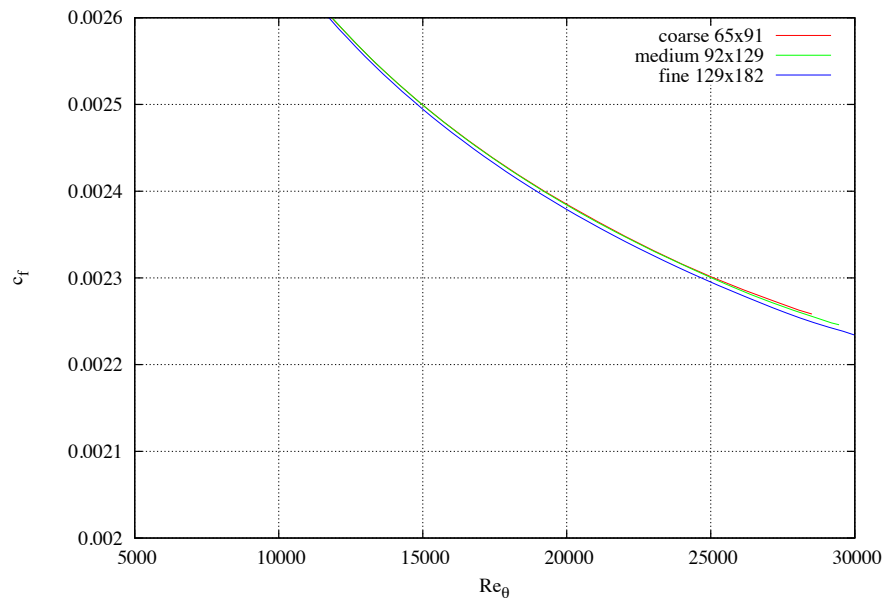
Figure 3.4. Skin friction profiles for lagRST with $\sigma_k = 1.5$ showing the effects of varying grid dimensions
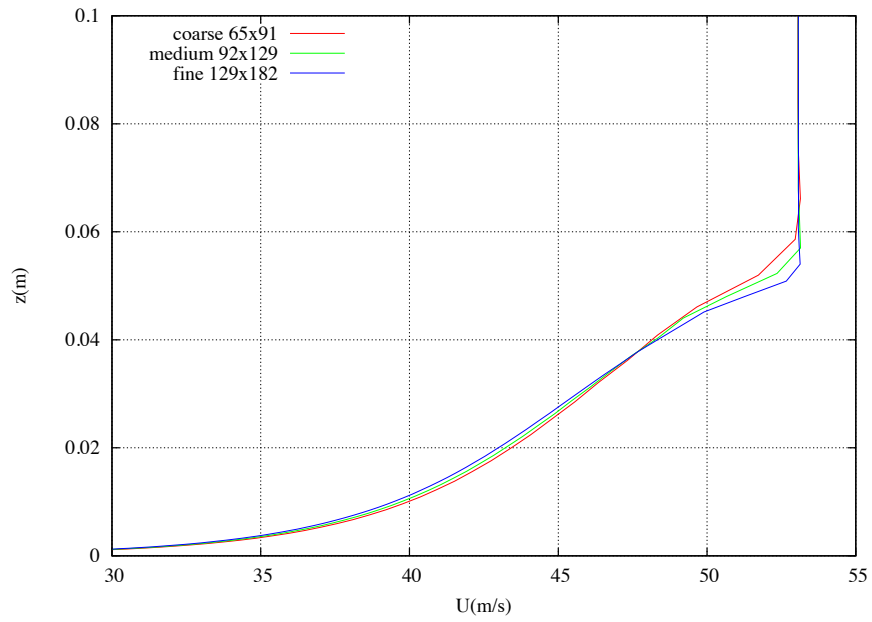
Figure 3.5. Velocity profiles for lagRST with $\sigma_k = 0.5$ showing the effects of varying grid dimensions
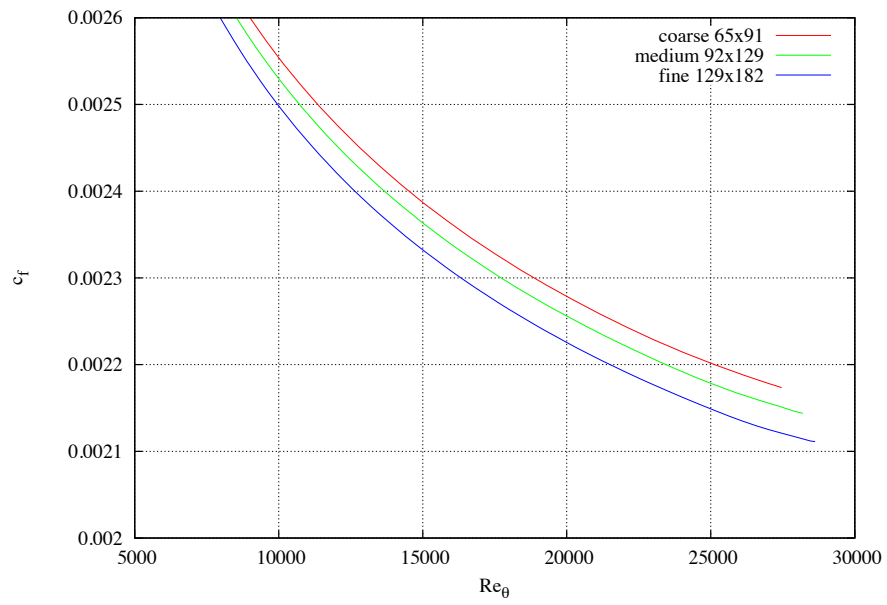
Figure 3.6. Skin friction profiles for lagRST with $\sigma_k = 0.5$ showing the effects of varying grid dimensions
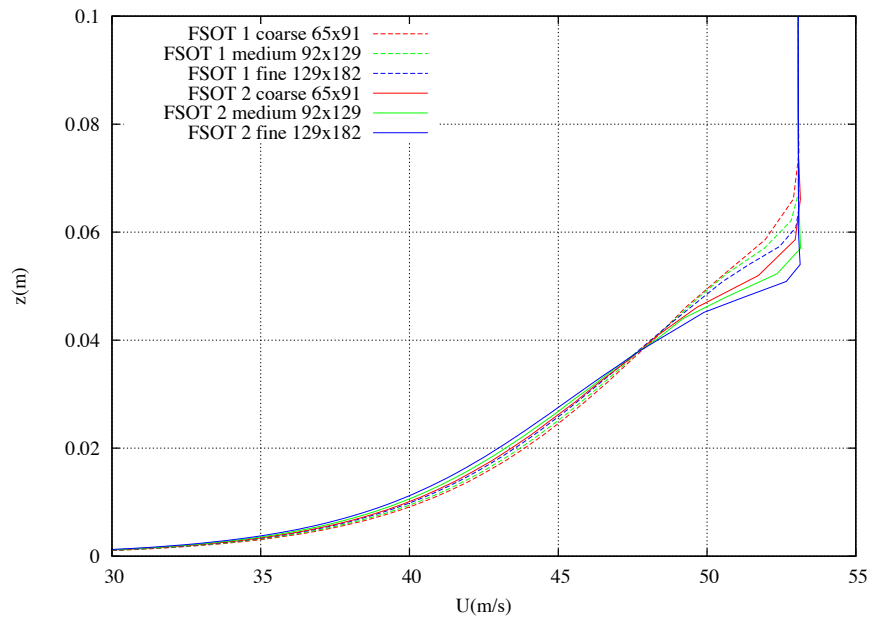
Figure 3.7. Velocity profiles for lagRST with $\sigma_k = 0.5$ showing the effects of varying grid dimensions for a 1st order (FSOT 1) convective term formulation vs the 2nd order (FSOT 2) formulation.
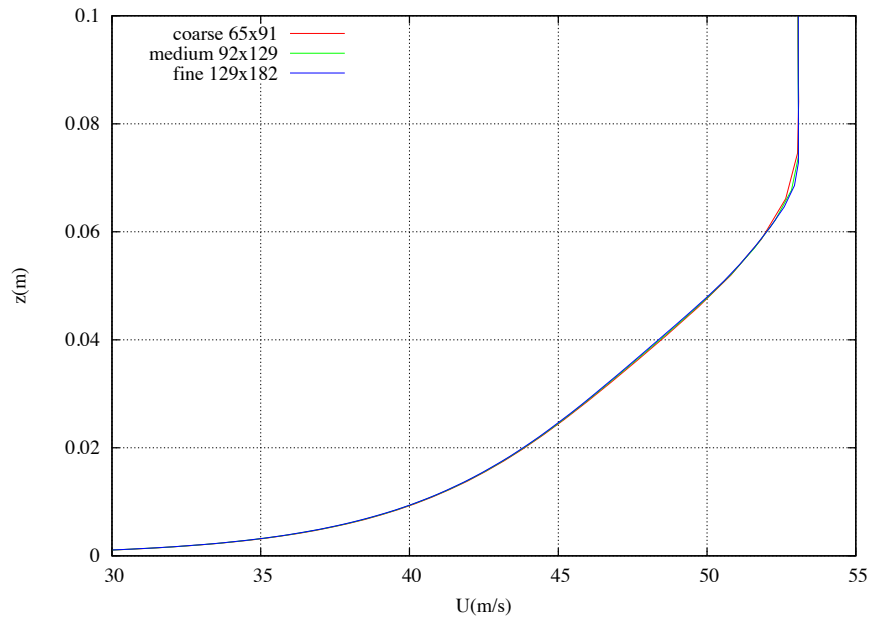
Figure 3.8. Velocity profiles for the SST model showing the effects of varying grid dimensions
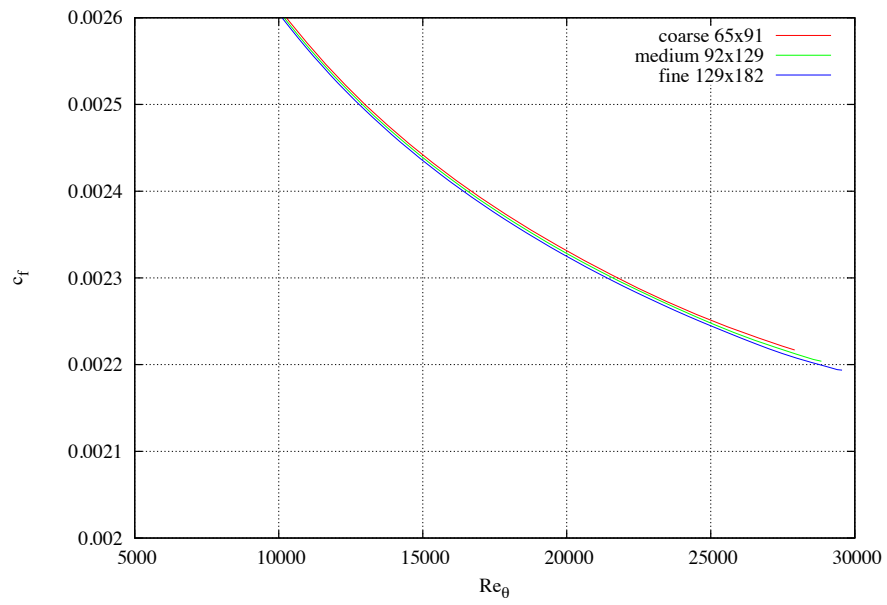
Figure 3.9. Skin friction profiles for the SST showing the effects of varying grid dimensions
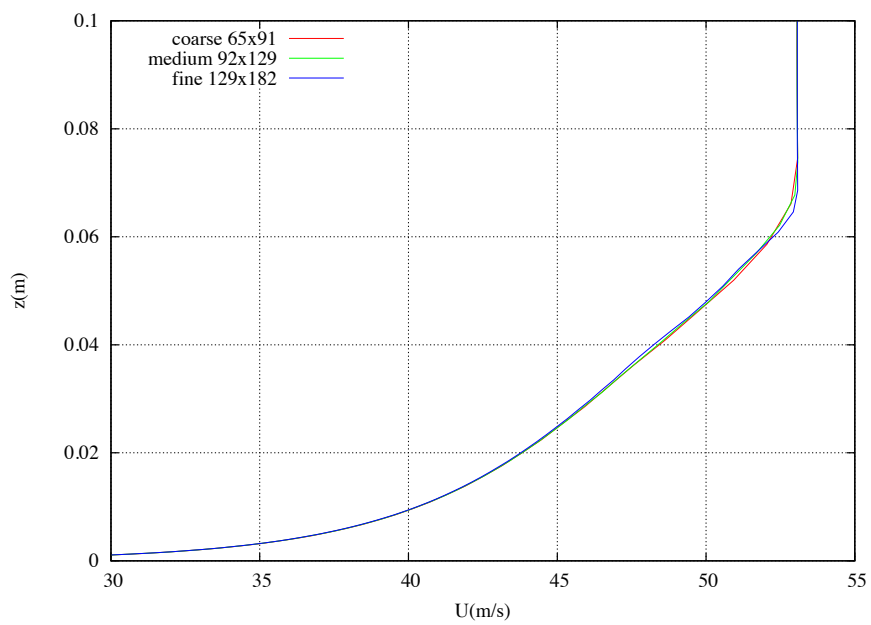
Figure 3.10. Velocity profiles for the SSTlagRST model showing the effects of varying grid dimensions
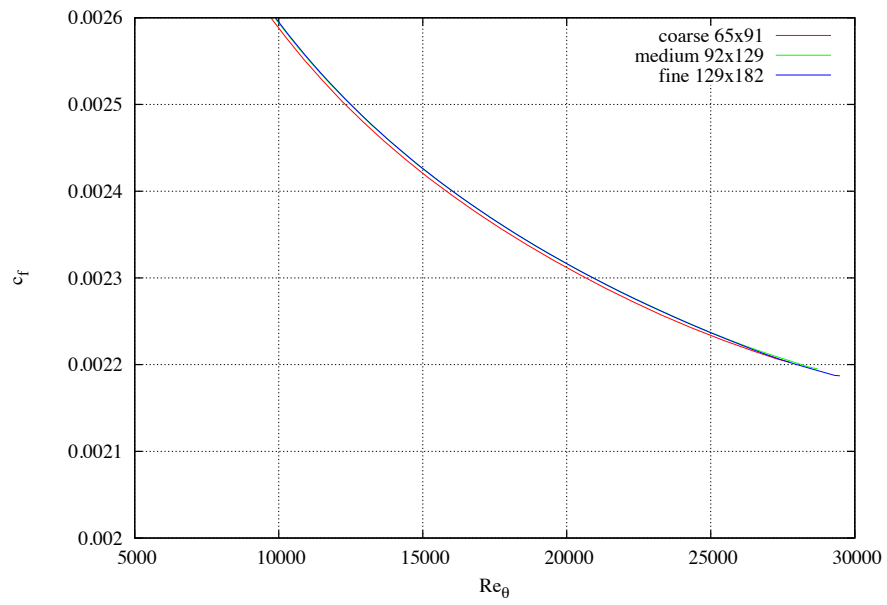
Figure 3.11. Skin friction profiles for the SSTlagRST showing the effects of varying grid dimensions

3.1.2 Model Consistency lagRST

To begin the analysis, the first series of plots analyzed were to assure the proper implementation of the lagRST models. Figure 3.12 shows velocity profiles plotted for three different turbulence models, 304 (standard 3 equation lag model), 903 (lag model using RST implementation), and 905 (lagRST model). 903 has not been previously discussed, but it is the implementation of the lag model in a lagRST form. In other words, the lagged variable is still μ_t, but the Reynolds stress tensor is calculated before it is added into the momentum equation, instead of adding the turbulent viscosity to the laminar viscosity inside the momentum equation. You are essentially adding a turbulent Reynolds stress explicitly instead of augmenting the laminar viscosity with the turbulent viscosity. This model is used to test one of the larger modifications to the OVERFLOW code.

The lag model and the lagRST model should give very similar answer (if not exactly the same) for equilibrium turbulent boundary layers because there are no non-equilibrium effects. The figure shows this, as a_0 constants were chosen to be 0.2 and 0.35 and σ_k was chosen to be 0.5, 0.8, and 1.5. For all cases, the lag and lag using the RST implementation give nearly identical results and the lagRST differences are on the order of $1 - 2\%$ for the worst case. Figure 3.13 plots the same profiles in law of the wall space. The results are again identical. Figure 3.14 shows the skin friction comparisons that go along with the previous two figures. The models are all within 1 to 2% for a given choice of constants.

The choice of σ_k makes a large difference in the wake portion of the boundary layer, especially near the edge. Values less than 0.8 look to cause an inflection in the velocity profile. Figure 3.15 shows the standard lagRST set of coefficients ($a_o = 0.35$ and $\sigma_k = 0.8$) and the recommended second order convective term discretization. The dashed lines represent a 1st order implementation for a varying set of coefficients. The figure shows a dramatic change in the shape of the curve near the edge of the boundary layer when the order is changed from 1st to 2nd for the same set of coefficients (dashed vs bold green lines). However, by reducing σ_k for a 1st order scheme to 0.55, a nearly identical profile to the standard lagRST set can be obtained. This points to the fact that the 1st order scheme
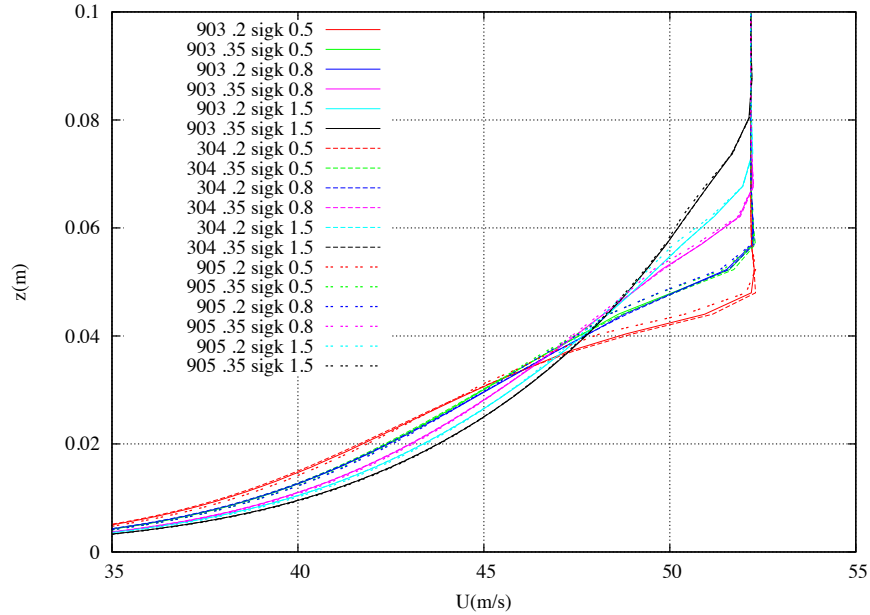
Figure 3.12. Velocity profiles for lag and lagRST showing consistency between models.

is increasing the numerical dissipation, so by decreasing σ_k the total numerical dissipation is brought back to the standard lagRST set. This needs to be assessed for separated flows as well (and will be in upcoming sections), but by changing the value of σ_k the velocity profiles can then be matched between 1st and 2nd order. The recommendation for the model will be to run 2nd order unless the scheme does not behave well numerically and in that case, the model will be ran 1st order with a reduced value of σ_k. The model coefficients will thus be down-selected from 2nd order solutions and then the equivalent values of σ_k for the 1st order set will be found.
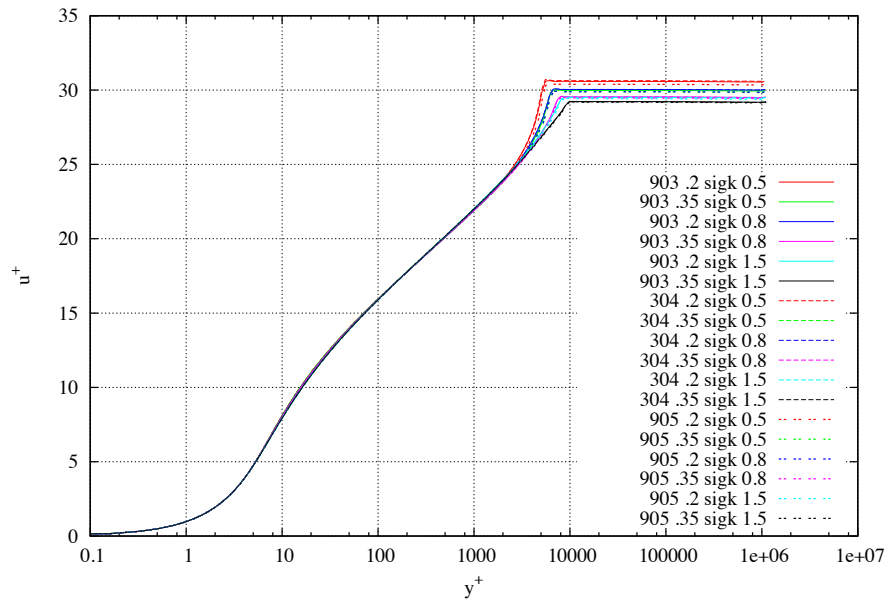
Figure 3.13. Velocity profiles in law of the wall space for lag and lagRST showing consistency between models
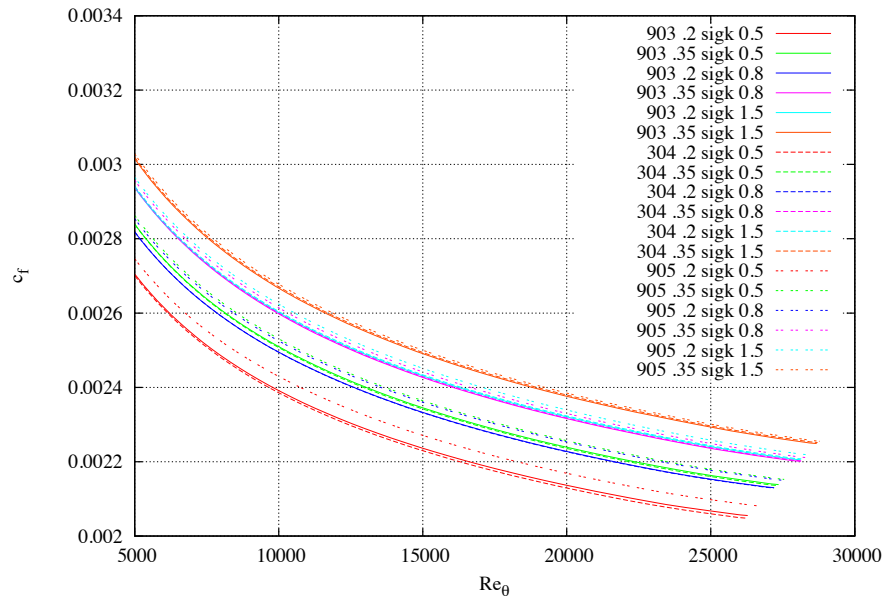
Figure 3.14. Skin friction verses Re_θ for lag and lagRST showing consistency between models
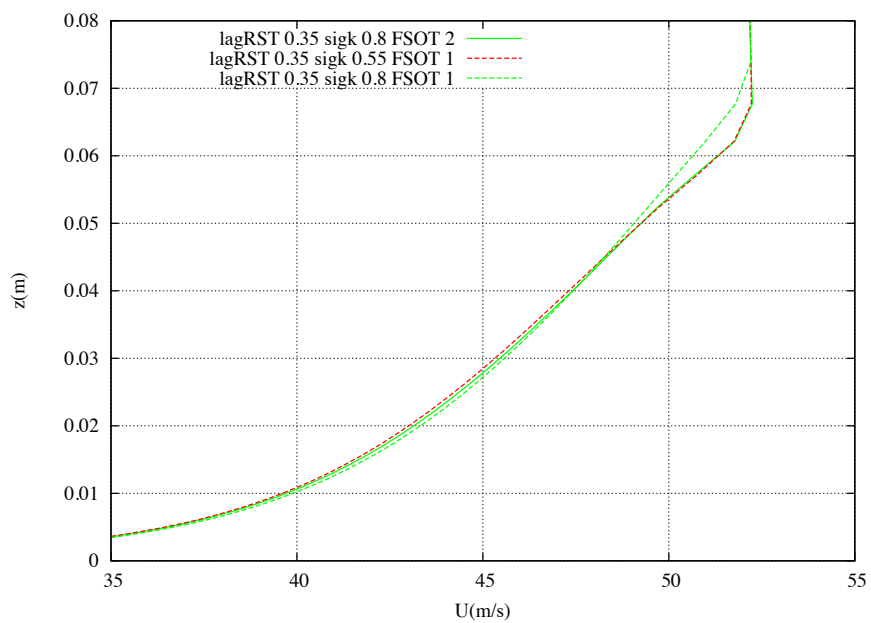
Figure 3.15. Velocity profiles for the lagRST model with varying coefficients and order of accuracy.

3.1.3 Model Consistency SST

This section assess the implementation of the SST version of the model. Figure 3.16 shows velocity profiles for for the two-equation SST model, the SST model with a Reynolds Stress implementation using a 1st order discretization, the SST model with a Reynolds Stress implementation using a 2nd order discretization, and the lagRSTSST model. All of the models give nearly the same results, showing little sensitivity to the order of the turbulent convective operators.

Figure 3.17 shows the skin friction comparisons for the same predictions as the previously discussed velocity profiles. All models are well within 1%.
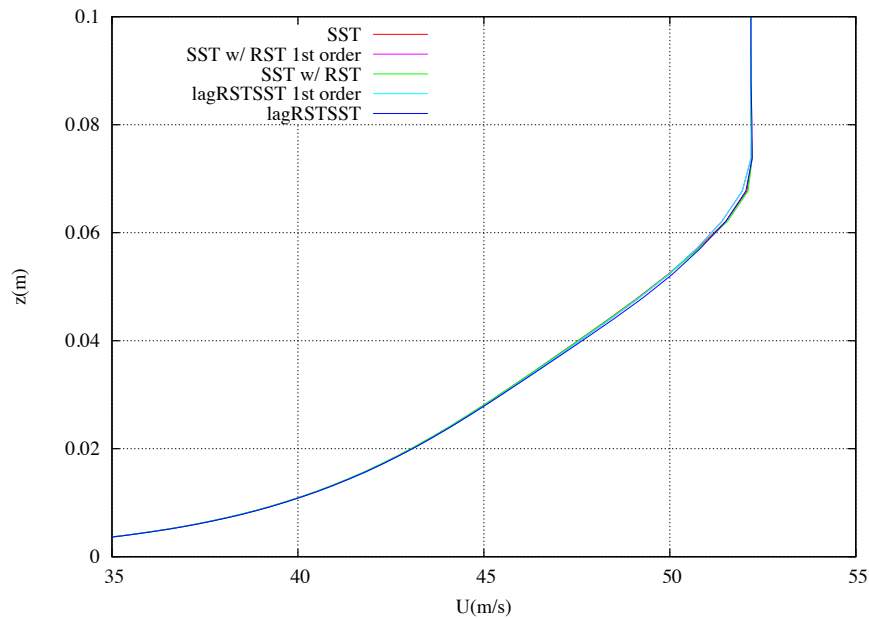
Figure 3.16. Velocity profiles for SST and lagRSTSST showing consistency between models.
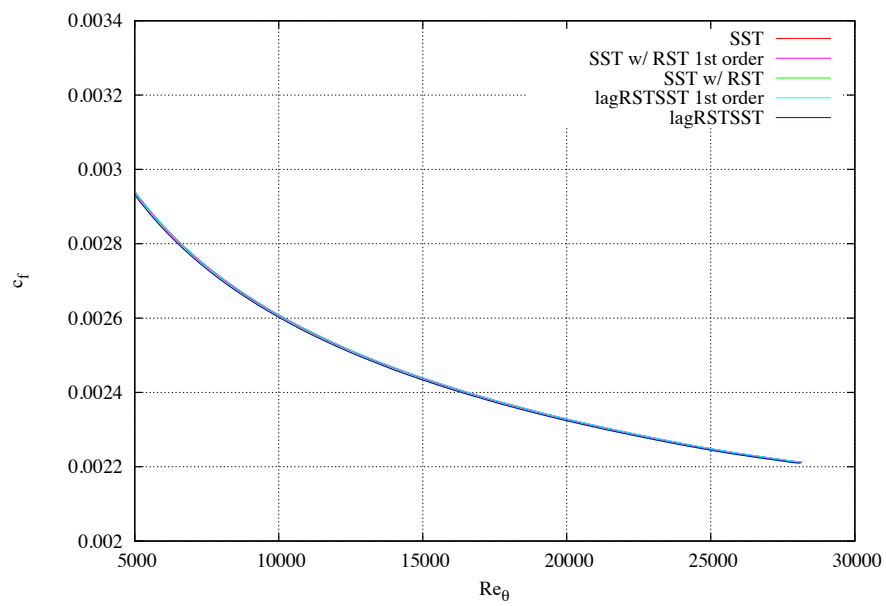
Figure 3.17. Skin friction verses Re_θ for SST and lagRSTSST showing consistency between models

3.1.4 lagRST Constant Selection

Figure 3.12 shows the lagRST model with varying coefficients compared to Osterlund's velocity profile data. As it was seen before with previous plots, low values of a_o and σ_k cause an inflection in the boundary layer profile that is not physical. The profiles that retain a shape without an inflection are $a_o = 0.35$ along with $\sigma_k = 0.8$ and both solutions with $\sigma_k = 1.5$.
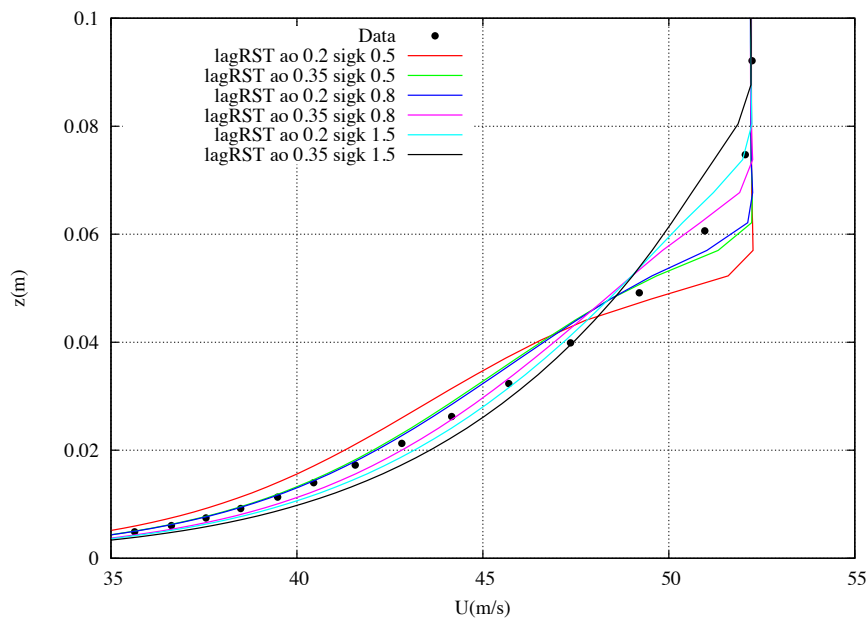
Figure 3.18. Velocity profiles for the lagRST compared to Osterlund's data.

Figure 3.13 shows the same data in law of the wall space. All the profiles match the data in the law of the wall region, but differ in the wake portion. This region will be explored in depth later.

Figure 3.20 shows a comparison of the C_f vs Re_θ for the lagRST model and the Osterlund data along with the Fernholz and Finley [90] correlation,
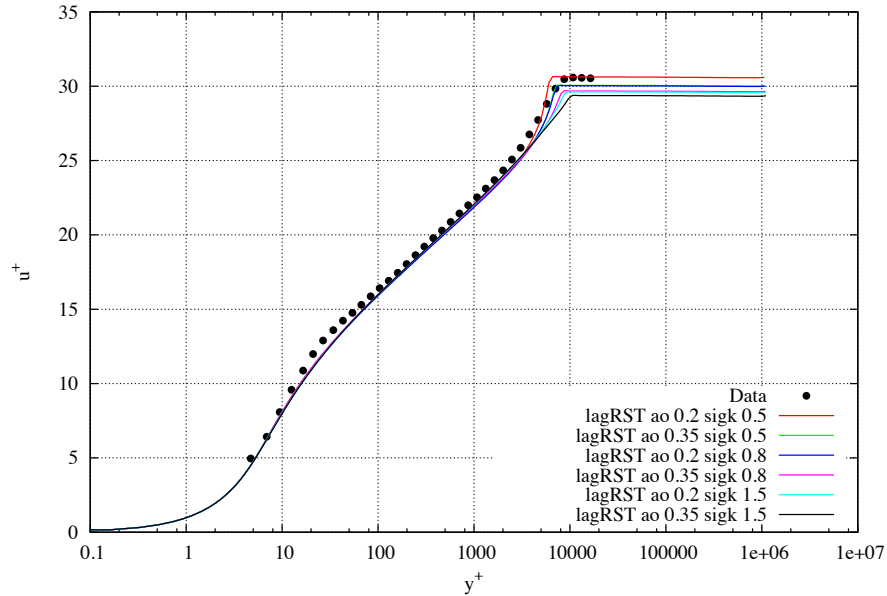
Figure 3.19. Velocity profiles in law of the wall space for lagRST compared to Osterlund's data

$$C_f = 2\left[\frac{1}{\kappa}ln\left(Re_\theta\right) + C\right]^{-2} \tag{3.1}$$

Osterlund used the flat plate data to propose modified values of κ and C, 0.384 and 4.08. The Karman- Schoenherr [91] relation,

$$C_f = \frac{1}{17*(log_{10}(x))^2 + 25.11*(log_{10}(x)) + 6.012} \tag{3.2}$$

was also plotted for comparison purposes. Watson et al. [92] concluded after high Reynolds number testing that Karman-Schoenherr was within 3% of high Reynolds number data. The data scatter was approximately 2%. They also show that Fernholz and Finley consistently under predict the other correlations by a few percent.

The errors between Osterlund's data, Fernholz and Finley (with calibrated constants from Osterlund), and Karman-Schoenherr are on the order of 5%. This is consistent with the findings of Watson et al. Based on the error in the data reported by Watson and the differences between the correlations, an error band of approximately $\pm\,5\%$ will be used to assess the models. Using $\sigma_k = 0.5$ and $a_o = 0.2$ provides the worst comparison to the correlations and the data. $\sigma_k = 1.5$ and $a_o = 0.35$ are above both correlations and the data, although the difference between the prediction and Karman-Schoenherr is less than 5%.
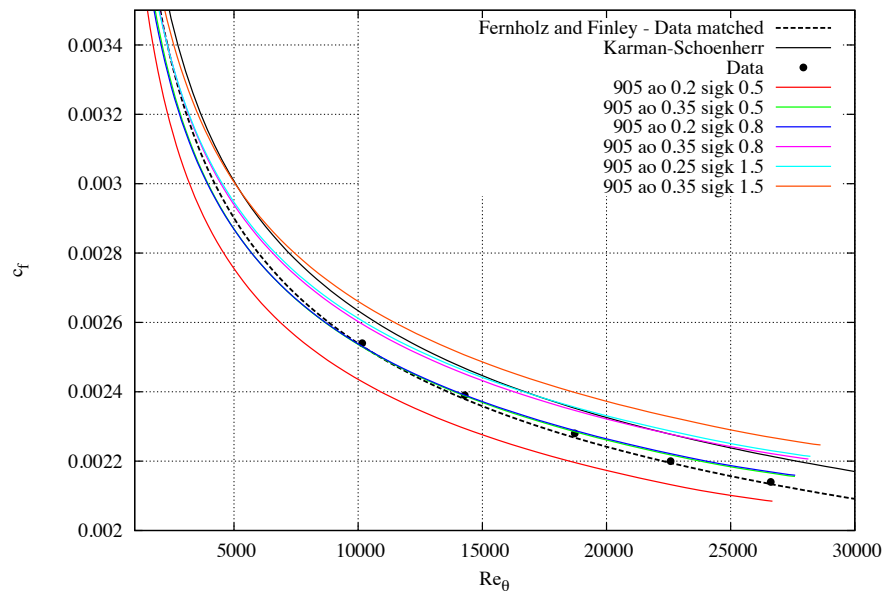
Figure 3.20. Skin friction comparison between Osterlund data, Fernholz and Finley, Karman-Schoenherr, and lagRST.

It is clear from the previous figures that the modeling constants have a large effect on the wake portion of the turbulence boundary layer predicted by the lag models. Figure 3.21 shows the Osterlund data with the lagRST model compared to Coles law of the wake [93]. The law of the wake is defined as

$$u^+ = \frac{1}{\kappa} ln y^+ + B + \frac{\tilde{\pi}}{\kappa} w\left(\frac{y}{\delta}\right) \tag{3.3}$$

where $w(y/\delta)$ is the wake function and can be approximated by $1 - cos(\pi y/\delta)$. Coles defined κ and B to be 0.41 and 5.0, respectively. Rohsenow et al. [94] defined $\tilde{\pi}$ as a constant of 0.55 for high Reynolds number such as the flow of Osterlund. The law of the wake correlation agrees very well with the data of Osterlund, but the lagRST model predicts a wake portion that does not propagate as low into the boundary layer and has a stronger peak than it should. Figure 3.22 is a repeat of the previous figure but it only shows the range of y^+ values where there are differences in u^+ between correlation, data, and prediction. The figure shows that when either a_o or σ_k is decreased the wake portion moves down into the boundary layer and increases in strength.
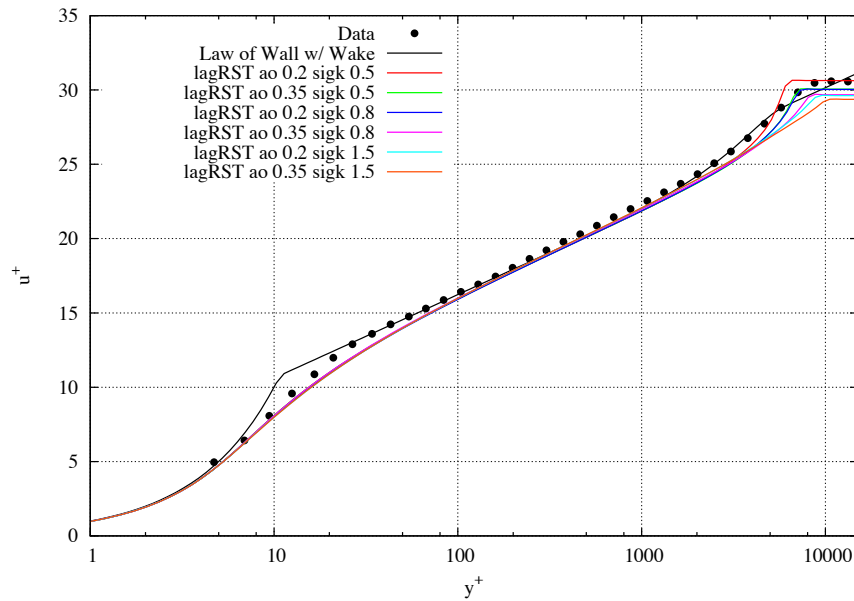
Figure 3.21. Velocity comparison in law of the wall space for lagRST with Osterlund and Cole's law of the wake.
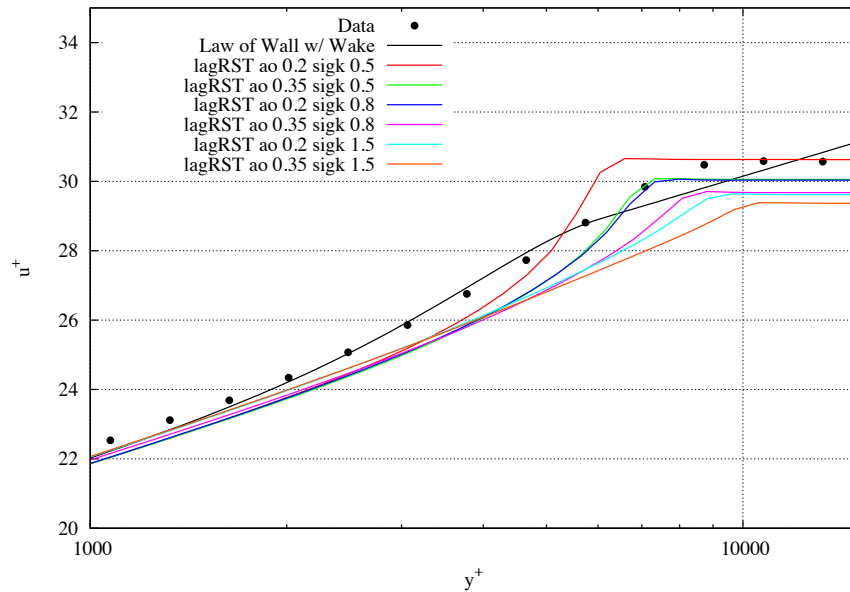
Figure 3.22. Velocity comparison in law of the wall space for lagRST with Osterlund and Coles law of the wake, zoomed into area of interest.

Figure 3.23 shows the Osterlund data and the lagRST model plotted as a wake correlation. Here the velocity decrement, $u_e^+ - u^+$ is plotted verses a function of the distance form the wall, $2 + log_{10}(y/\delta)$. The lower values of a_0 and σ_k are more accurate near the edge while the higher value of the constants match the data near the surface.

Based on the results in this subsection, several combinations of the constants can be discarded. The inflection in the velocity profiles removes σ_k values of 0.5 and low a_o values with $\sigma_k = 0.8$. The skin friction comparisons reinforce the removal of $a_o = 0.2$ with $\sigma_k = 0.5$ due to how much lower they are than the correlations and data. That leaves three sets of coefficients to assess, $a_o = 0.35$ with $\sigma_k = 0.8$ and $a_o = 0.2$ and $a_o = 0.35$ with $\sigma_k = 1.5$. Based on skin friction predictions, $a_o = 0.35$ and $\sigma_k = 1.5$ provide the largest difference between the data and the predictions. The two remaining combinations, $a_o = 0.2$ and $\sigma_k = 1.5$ verses $a_o = 0.35$ and $\sigma_k = 0.8$, are nearly identical and compare
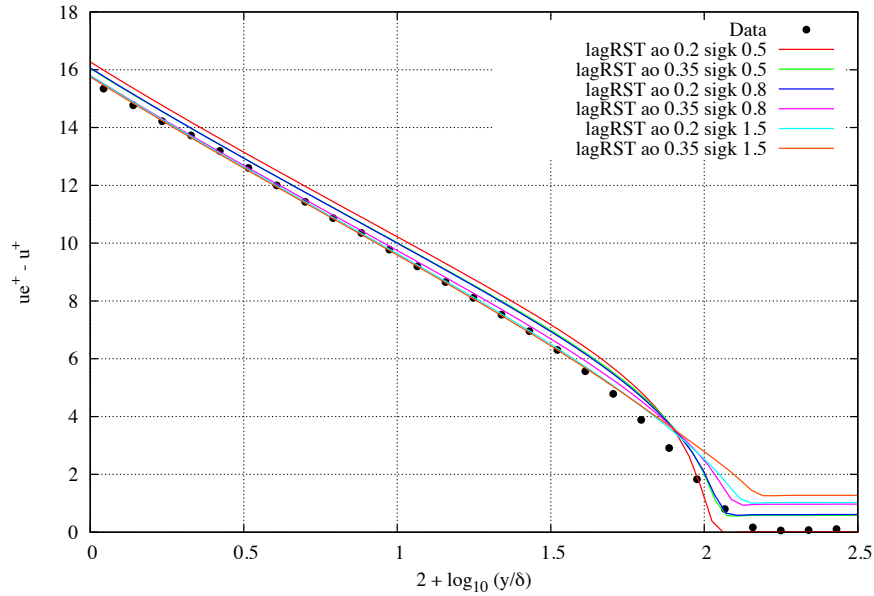
Figure 3.23. Velocity profiles for the lagRST model plotted with Oster-
lund's data plotted as a velocity decrement

extremely well to Karman-Schoennher and are within 5% of Osterlund's data. Further
analysis will be done to choose between those two constants.

Now that the coefficient sets have been reduced, the set of 1st order values of σ_k need to
be assessed. Figure 3.15 defined the first order value σ_k value for $a_o = 0.35$ and $\sigma_k = 0.8$.
Figures 3.24 and 3.25 define the first order value of σ_k for the remaining cases. Table 3.1.4
details the 1st order values for σ_k based on the constant values chosen above.

a_o	σ_k 2nd order	σ_k 1st order
0.2	1.5	1.2
0.35	1.5	1.35
0.35	0.8	0.55

Table 3.2 First order values of σ_k for the second order constant values of $a_o = 0.2$ and $\sigma_k = 1.5$ for the lagRST model.
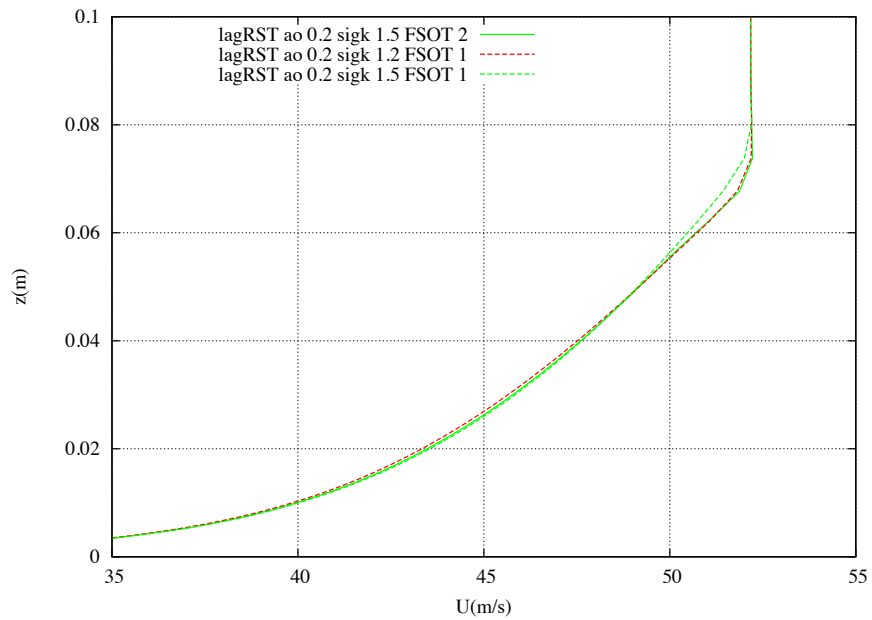
Figure 3.24. Velocity profiles for the second order constant values of $a_o = 0.2$ and $\sigma_k = 1.5$ for the lagRST model.
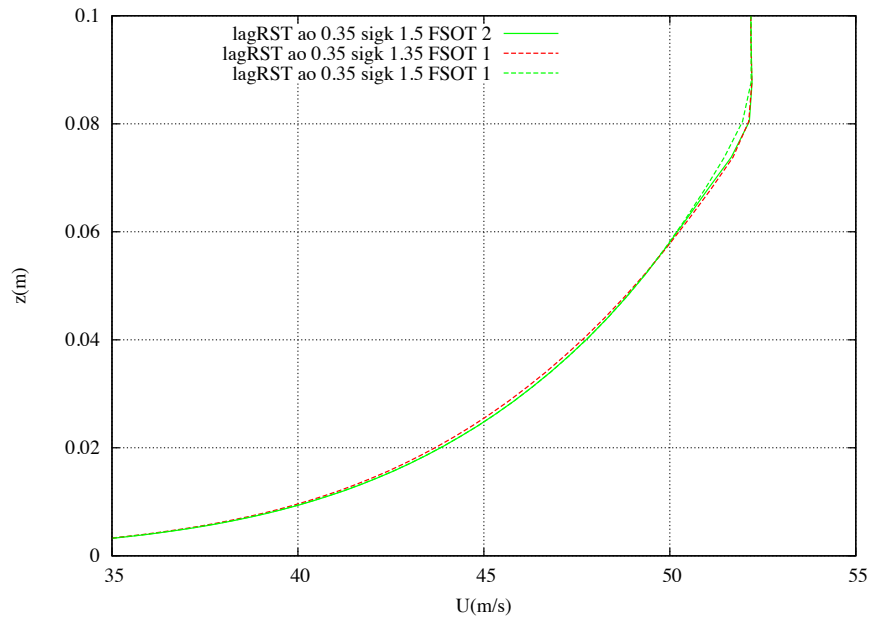
Figure 3.25. Velocity profiles for the second order constant values of $a_o = 0.35$ and $\sigma_k = 1.5$ for the lagRST model.

3.1.5   Model Comparisons

Figures 3.26 shows the lagRST model with the previously selection combinations a_0 and σ_k as well as the lagRSTSST model compared to the standard SST and Spalart All-maras models in the OVERFLOW code. The SA model has a fuller profile about one third to halfway up in the boundary layer, but then at the edge approaches the data nicely. The lagRST model with a_0 and σ_k of 0.2 and 1.5, respectively, is very close to the data. The error is all on the order of 5%. In addition, the inflection near the edge in the lagRST models is avoided based on the selection of constants.

Figure 3.27 shows the same results in law of the wall space. The SA model predicts the transition from the laminar sublayer to the law of the wall region much more accurately than all other models. However, the slope in the law of the wall region is slightly in error compared to the other models. On this scale, the SST models gives a very close result to the lag and lagRST models with constants a_0 and σ_k equal to 0.35 and 0.5, respectively. Figure 3.28 is the same data as the previous figure except Coles law of the wake is plotted and the scale is changed. The errors in the SA model are more apparent here. What is also evident from this plot is that although the SST model predicts nearly the same depth into the boundary layer of the wake region, the strength of the wake portion (i.e. the increase away from law of the wall) is smaller and thus could be said to have the characteristics of Coles law of the wake and the Osterlund data. Figure 3.29 is again the same data with a zoomed-in scale. It is more apparent here that the SST model predicts the shape of the wake region more accurately.

Figure 3.30 shows the results plotted as a velocity decrement verses distance from the wall. The SST model in general again over predicts the velocity profile for all values, although the shape of the curve is more accurate then the lagRST curves. The majority of the predictions are within 5% of other models with none of the models correctly predicting the shape of the wake portion of the boundary layer. There seems to be more curvature in the experimental data than is predicted by the simulations. A lower value of $a_o = 0.2$ was
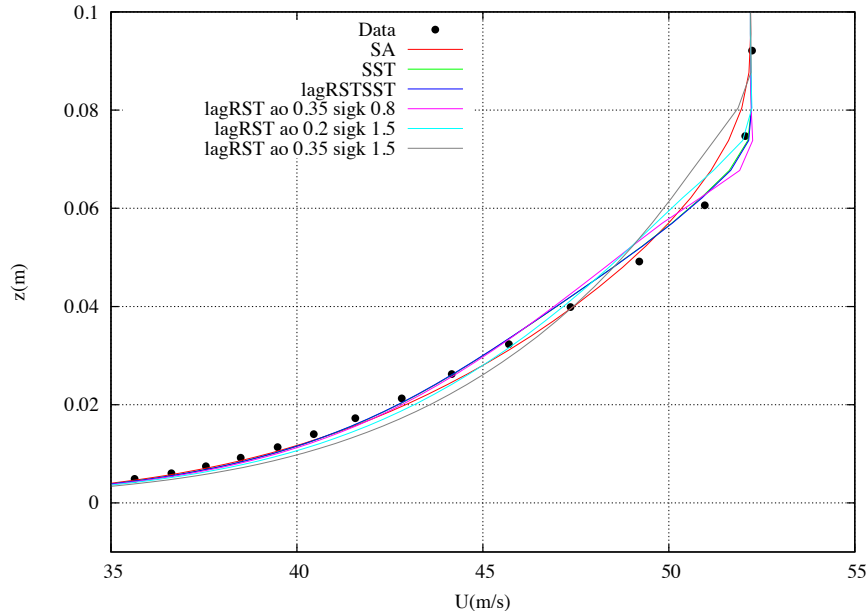
Figure 3.26. Velocity profiles comparing lag, lagRST, lagRSTSST, SST, and SA models

used for the lagRSTSST model to try and capture more of the correct profile shape, but it had very little affect.

Figure 3.31 shows the skin friction distributions for al the models represented in this section. The scatter in all the models is on the order of 2%. The comparisons to the Karman-Schoenherr relation are also on the order of 2%. All of the models over predict the data and the Fernholz and Finley correlation by as much as 10%.
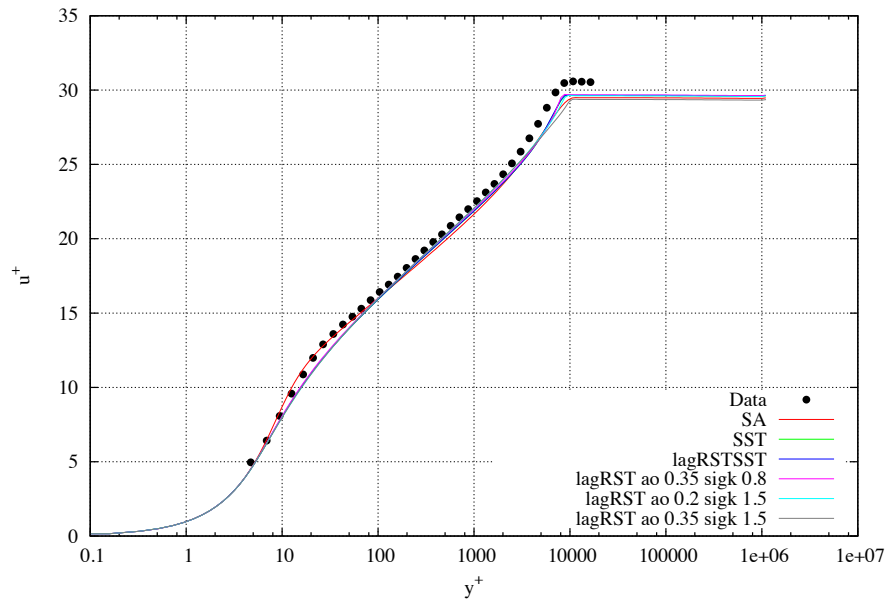
Figure 3.27. Velocity profile in law of the wall space comparing lag, lagRST, lagRSTSST, SST, and SA models
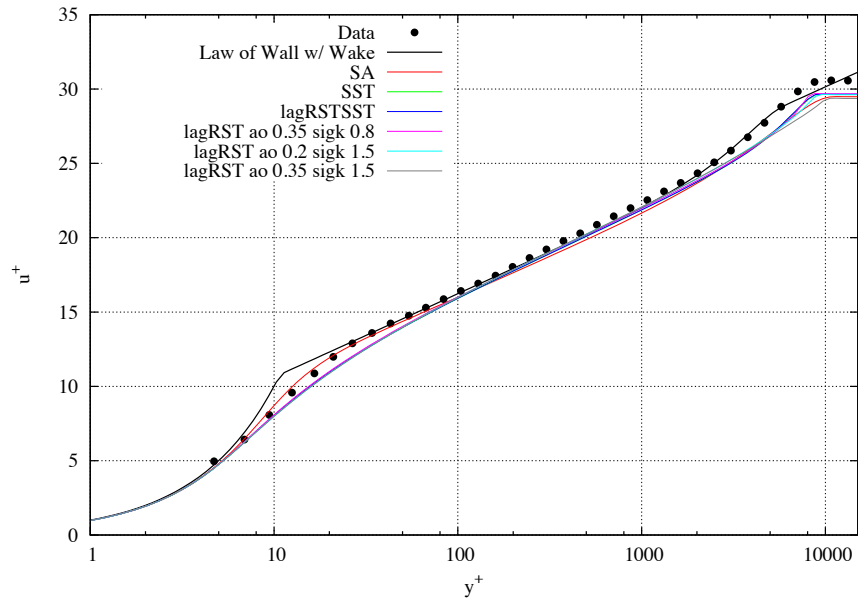
Figure 3.28. Velocity profile in law of the wall space comparing lag, lagRST, lagRSTSST, SST, and SA models with the addition of Cole's law of the wake.
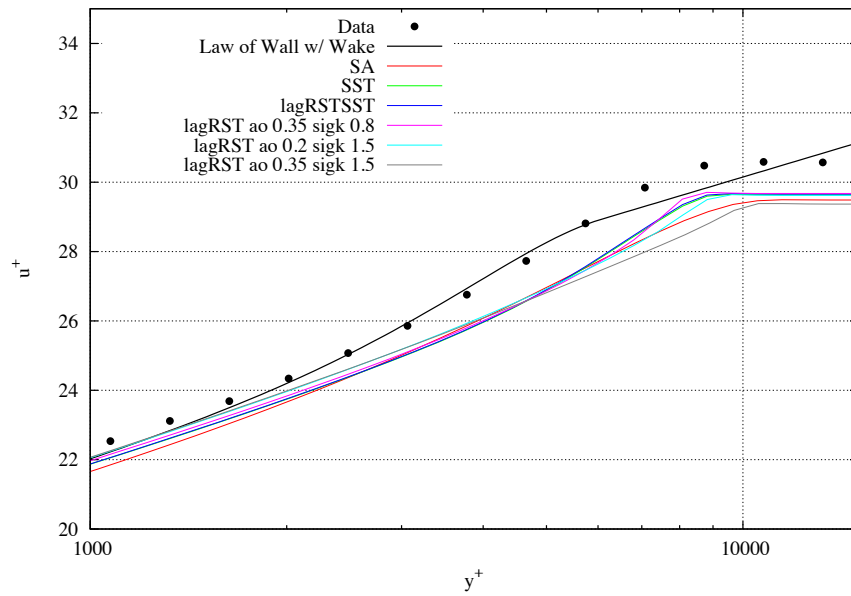
Figure 3.29. Velocity profile in law of the wall space comparing lag, lagRST, lagRSTSST, SST, and SA models with the addition of Coles law of the wake.
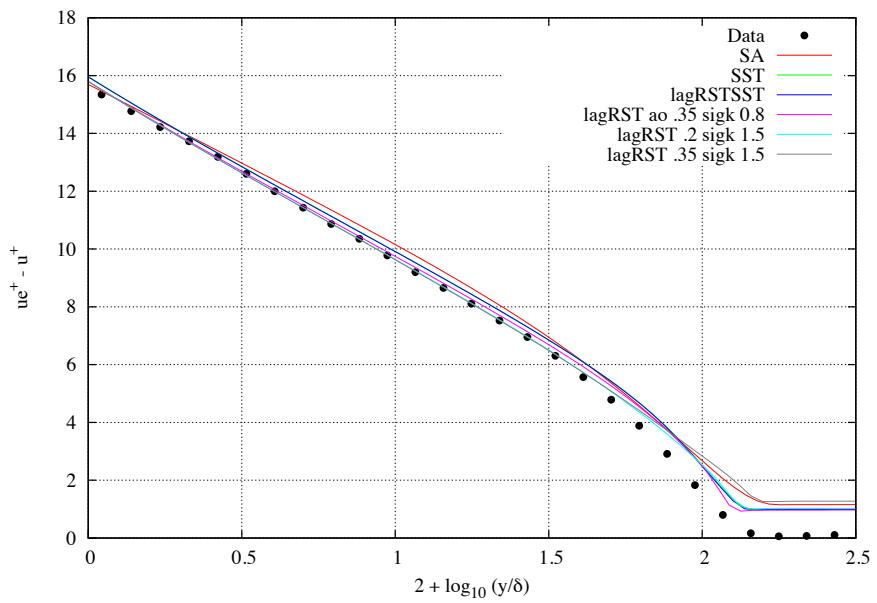
Figure 3.30. Velocity profiles plotted as a wake decrement showing comparison between SA, SST, lag, and lagRST
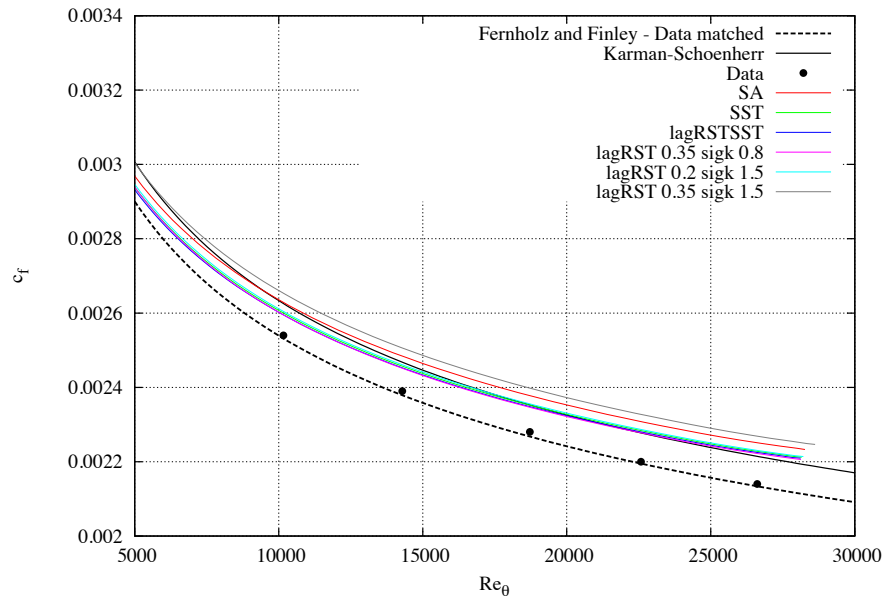
Figure 3.31. Skin friction comparison between Osterlund data, Fernholz and Finley, Karman-Schoenherr, and SA, SST, lagRSTSST, and lagRST.

3.2 Bell-Mehta Mixing Layer

Bell and Mehta [48] obtained data for a two-stream mixing layer with a velocity ratio of 0.6. They obtained data with both tripped and untripped boundary layers. For this comparison, only the tripped turbulent data will be used. They defined the shear-layer thickness using a least-squares fit of the mean data to the error function profile shape:

$$U^* = \frac{[1 + erf(\eta)]}{2} \tag{3.4}$$

where η is defined as

$$\eta = \frac{Y - Y_o}{\delta} \tag{3.5}$$

and Y_o is the centerline of the mixing layer and is defined from the error function fit. To compare to this data, the velocity profiles were extracted and then processed through least squares fit to calculate δ and Y_o. The upper velocity stream, U_{upper}, was set to $15m/s$ while the lower velocity stream, U_{lower}, was set to $9.0m/s$. The solution was initialized for all positive z values to U_{upper} and negative z values to U_{lower}. The inflow condition was set to the same velocity condition as the solution initialization and used an inflow/outflow condition. The upper and lower conditions were set to U_{upper} and U_{lower}, respectively and used the same inflow/outflow condition as the initial condition. The downstream boundary condition was set to extrapolation.

3.2.1 Grid Convergence

Three grids were generated in order to study grid convergence for this test case. The finest grid ran was 129 (axial) by 205. The grid was then decreased to 65 by 103 and 33 by 52. Figures 3.33 shows grid convergence for the lagRST and lagRSTSST models. For the lagRSTSST model, the medium grid (65 by 103) gets within 2% of the fine grid answer. For the lagRST again the medium grid gives excellent grid convergence and is within 1%.
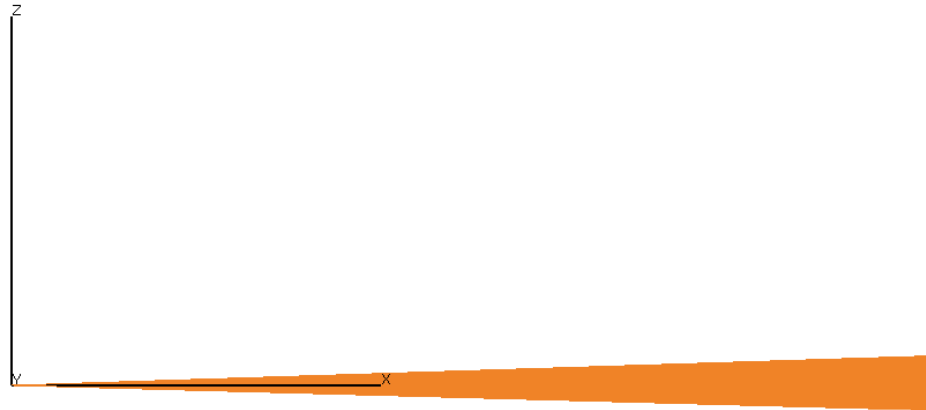
Figure 3.32. Computational domain for the mixing layer (flow from left to right).

3.2.2 Verification of the lagRST implementation

Figure 3.34 shows the lag based models, where 304 is the standard 3-equation lag model, 903 is the lag model with a RST implementation, and 905 is the lagRST model using a $\sigma_k = 1.5$ and $a_o = 0.35$. The lag and the lag using RST models compare nearly exactly to each other, which is expected. The lagRST model has a slightly higher growth rate than the lag and lag using RST. Convergence is obtained for the medium and fine grids. All the models compare very poorly to the data. Previous work by Olsen and Coakely /cite-Olsen:2001a

3.2.3 Verification of lagRSTSST implementation

Figure 3.35 shows two-equation SST model along with the SST model implemented with a Reynolds Stress tensor and the lagRSTSST model. All the models show excellent agreement for the medium and fine grids.
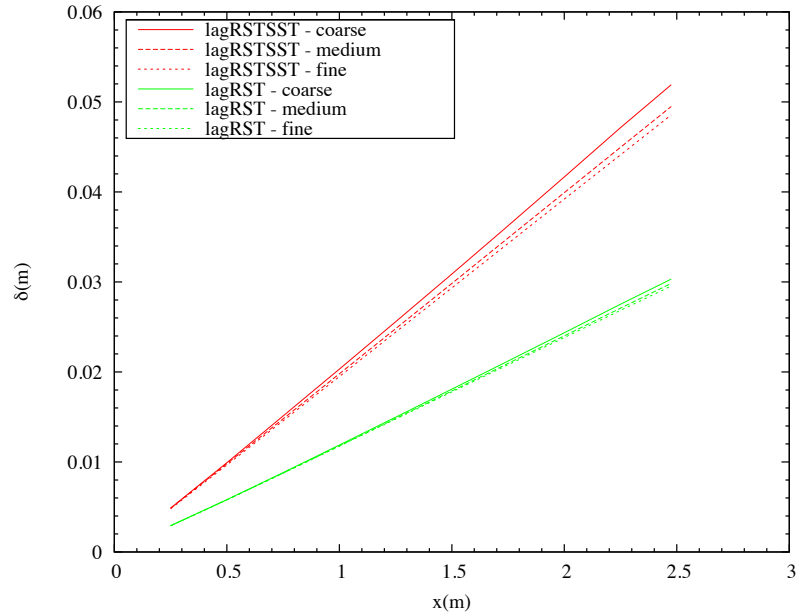
Figure 3.33. Grid convergence for the lagRST and lagRSTSST models compared to the mixing layer growth data for the fine (129 by 205), medium (65 by 103), and coarse (33 by 52) grids.

3.2.4 Model Comparisons

Figure 3.36 shows a comparison of the SST, lag, lagRST, and lagRSTSST models. The lagRSTSST compares very well with the standard two-equation SST model and the experimental data. The lagRST and lag model comparisons are very poor, even with large variations in σ_k. To date, there has been no explanation for this.

For the lagRSTSST model, a lower value of the lag constant, $a_o = 0.2$, was assessed for this case. It had little affect, but did increase the slope of the growth rate by 1.5%.
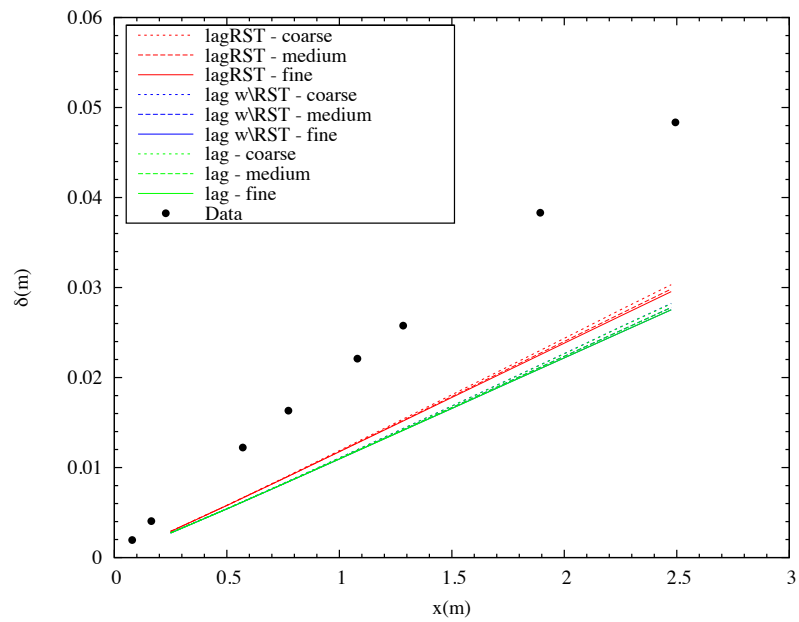
Figure 3.34. Grid convergence for the lag based models compared to the mixing layer growth data for the fine (129 by 205), medium (65 by 103), and coarse (33 by 52) grids.
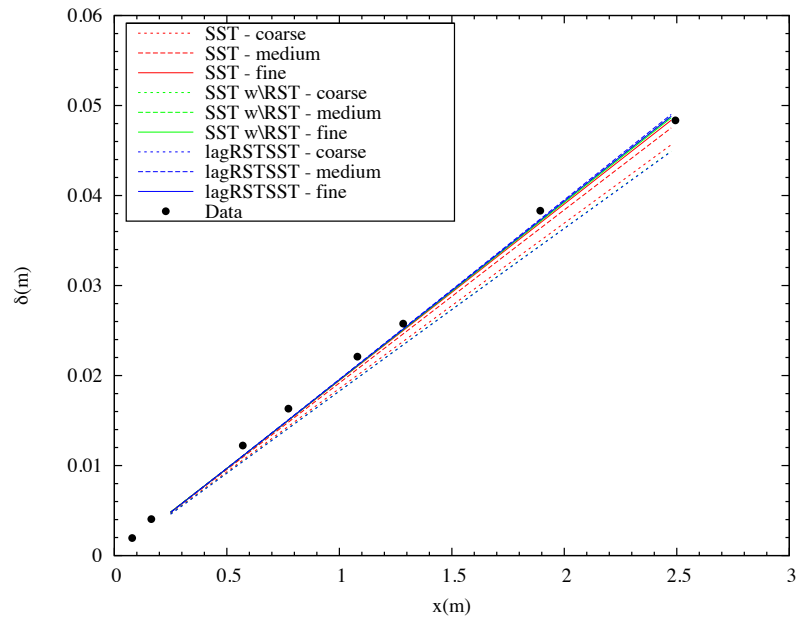
Figure 3.35. Grid convergence for the SST based models compared to the mixing layer growth data for the fine (129 by 205), medium (65 by 103), and coarse (33 by 52) grids.
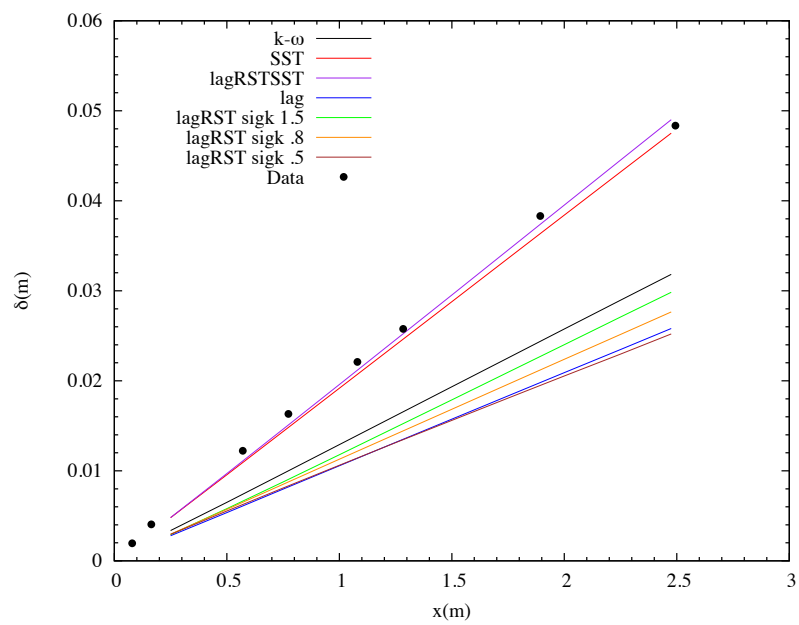
Figure 3.36. Mixing layer growth rate comparisons for the SST, lag, la-gRST, and lagRSTSST models.

3.3   Driver's CS0 Flowfield

Driver [49] executed an incompressible test of a turbulent separated boundary layer. The geometry is an axisymmetric cylinder with the downstream grid boundary defined by an external streamline, determined from the experimental data. The upstream boundary conditions were constant total pressure and temperature, with static pressure allowed to vary and velocity direction aligned with the cylinder axis. The outer streamline was treated as an inviscid wall. The viscous wall is no-slip and adiabatic. The downstream static pressure was adjusted in a similar fashion that Olsen and Coakley [5] used. They adjusted the downstream static pressure at the exit to match the experimental static pressure upstream of the interaction region ($x = -0.438m$). In addition, the upstream length was also taken from Olsen and Coakley [5] to match the experimental boundary layer thickness. This method was chosen so that comparisons could be made to the conclusions obtained in the original formulation of the lag model, and comparisons to the constants chosen for the lag model. The upstream grid length was modified so the boundary layer thicknesses matched at $x = -0.477m$, the same point where the pressure matching was done.

The calculations were made on the same grids used in the original analysis by Olsen and Coakley [5]. The fine grid had 200 (axial) by 160 (radial). The coarse grid was a factor of 2 reduction in grid points (100 by 80) and the medium grid had 150 by 120. Olsen used the grids referred to as fine and coarse in his study. Figure 3.37 shows the computational domain for this test case.
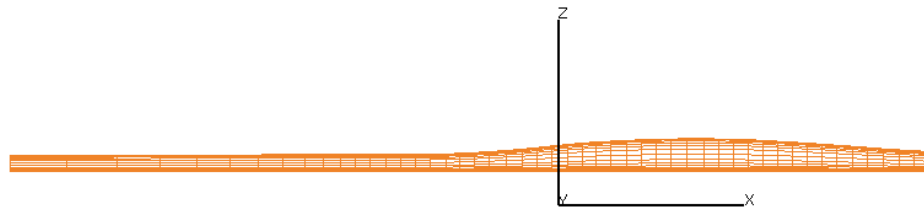
Figure 3.37. Computational domain, coarse grid pictured.

3.3.1 Grid Convergence

Figure 3.38 shows pressure distributions for the coarse, medium, and fine grids for the lagRST model with standard coefficients. There is some odd behavior with the medium grid in the pressure comparisons, as it does not give the same exact pressures as the coarse and fine grids. Figure 3.39 shows the skin friction plots. The medium grid gives nearly identical results to the fine grid.
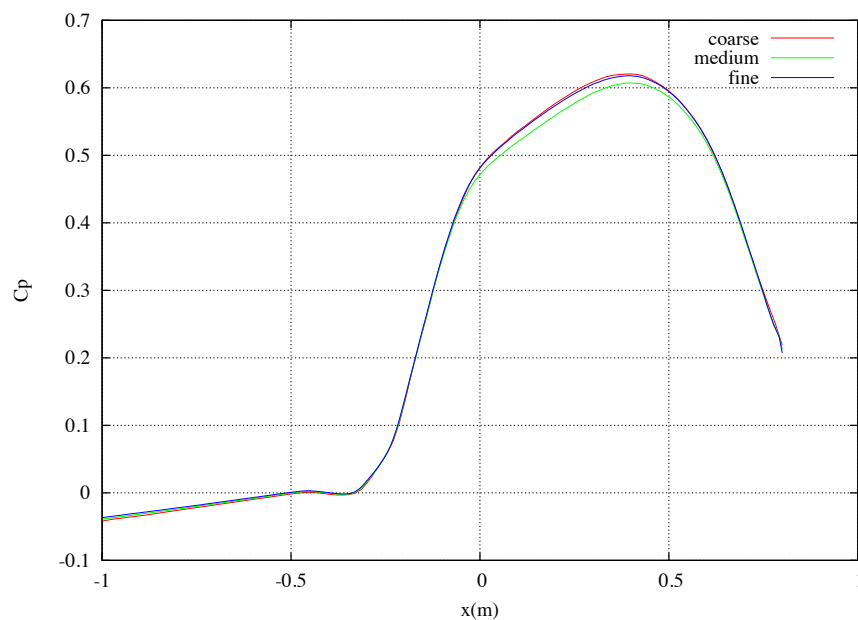
Figure 3.38. Pressure comparisons showing grid convergence for the lagRST model with standard coefficients.

Figure 3.40 and figure 3.41 show the pressure and skin friction plots for the lagRST model with the coefficient choice of $\sigma_k = 1.5$ and $a_o = 0.35$. These comparisons have very consistent pressure comparisons for all three grids and the skin friction comparisons are excellent for the medium and fine grids. The coefficient choice of $\sigma_k = 1.5$ and $a_o = 0.2$ is not pictured, but it has nearly identical convergence plots to this case.
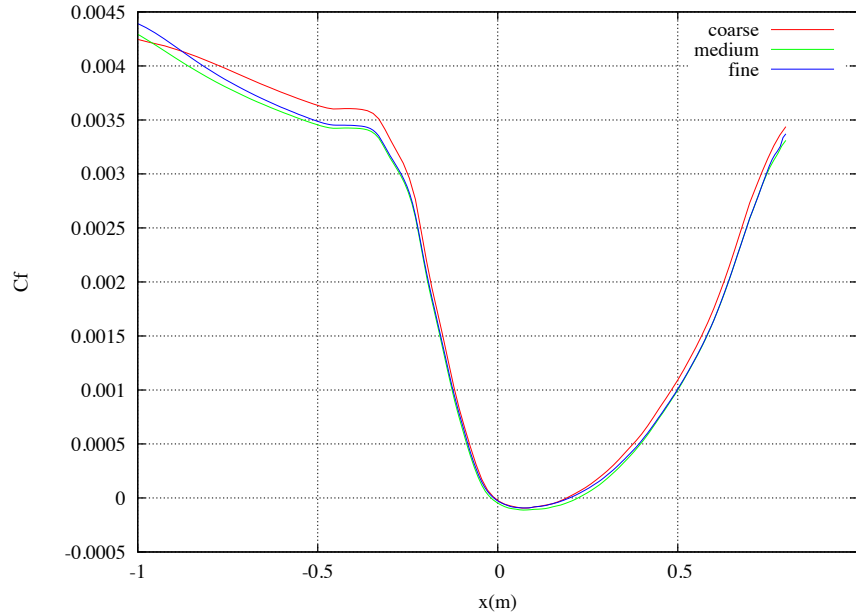
Figure 3.39. Skin friction comparisons showing grid convergence for the
lagRST model with standard coefficients.

Figure 3.42 and figure 3.43 show the pressure and skin friction distribution for the
lagRSTSST model. The model has excellent convergence behavior. There are mild differ-
ences well upstream, but once the adverse pressure gradient area starts all models are in
agreement.

The medium and fine grids for all cases matched the measured upstream boundary layer
thickness to within 10%.
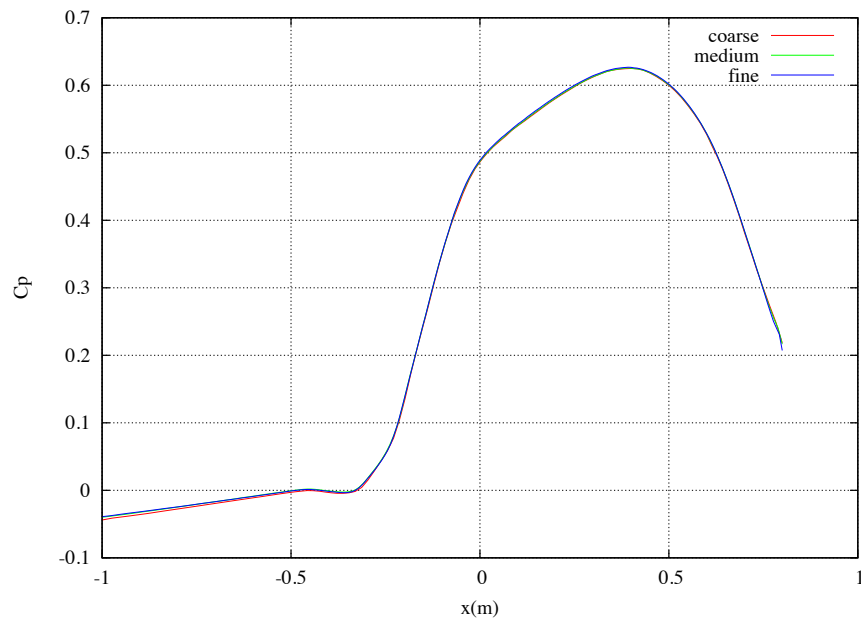
Figure 3.40. Pressure comparisons showing grid convergence for the la-gRST model with coefficients $\sigma_k = 1.5$ and $a_o = 0.35$.
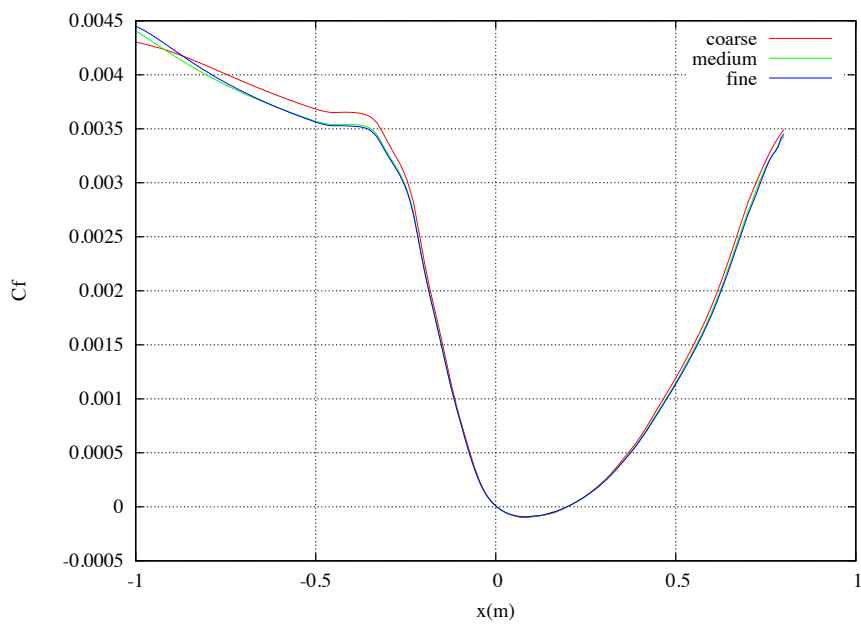
Figure 3.41. Skin friction comparisons showing grid convergence for the lagRST model with coefficients $\sigma_k = 1.5$ and $a_o = 0.35$.
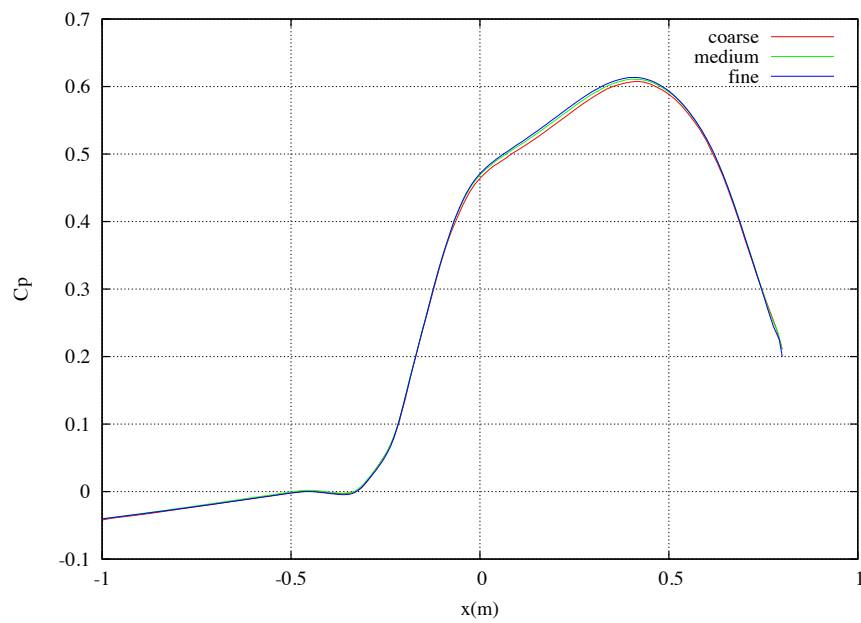
Figure 3.42. Pressure comparisons showing grid convergence for the lagRSTSST model.
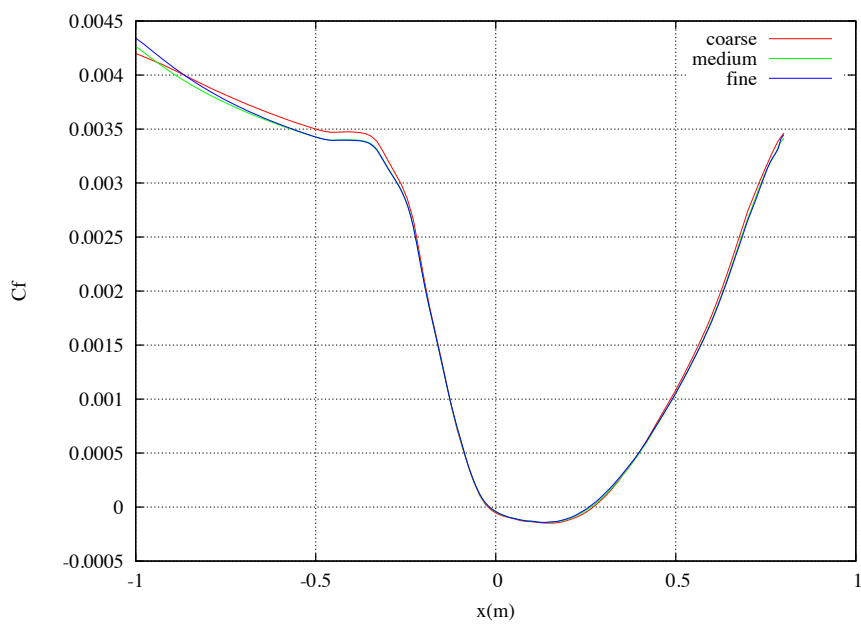
Figure 3.43. Skin friction comparisons showing grid convergence for the lagRSTSST.

3.3.2 Grid Convergence of Reynolds Stresses

Figure 3.44 shows the τ_{13} Reynolds Stress profile for SST model upstream of the separation point and figure 3.45 shows the same profile downstream of the separation zone. Even though the skin friction and pressure show excellent convergence for this case, the $\tau_1 3$ Reynolds Stress doesn't show quite the same convergence, especially near the edge of the boundary layer. Because the medium and fine grids didn't converge at the edge, an fourth grid was added. The grid appears to be slightly coarse at the edge, so the fine grid was ran doubled in the off-body direction to assess this. This grid is labeled "superfine". Note that for SST comparisons, the separation zone difference between the fine and superfine grid was less than 1%. The τ_{13} profile shows good grid convergence between the fine and superfine grids for both positions.
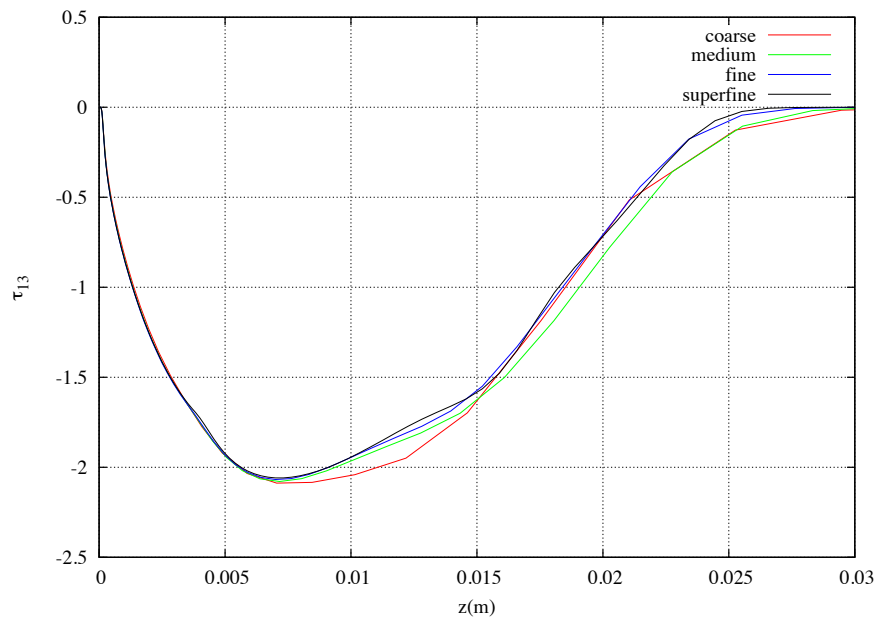
Figure 3.44. Grid convergence plots of τ_{13} for the SST model upstream of the interaction (x = -0.076m).
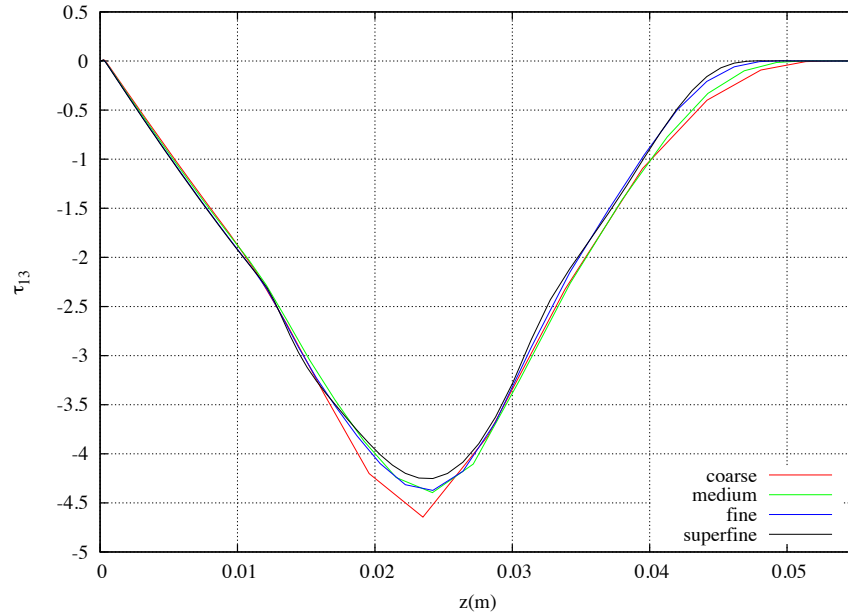
Figure 3.45. Grid convergence plots of τ_{13} for the SST model downstream of separation (x = 0.101m).

Figure 3.46 shows the τ_{13} Reynolds Stress profile for the lagRST model upstream of the interaction zone and figure 3.47 shows the same profile downstream of the separation zone. The medium and fine grid converge to with in a small percentage at the peak value within the boundary layer for both cases. Near the edge of the boundary layer, the solutions show even more dependence on the grid as seen for the SST profiles. For the upstream position, the superfine grid shows what appears to be a smoother profile at the edge than the medium and fine grids, but it still isn't as smooth as the SST predictions. Also, the separation zone prediction difference between the fine and superfine grids for the lagRST model are between $3 - 4\%$, which is higher than the SST model. The lagRST model is clearly more sensitive to the grid at the edge of the boundary layer than the SST model. This is most likely due to the lagRST model solving for each independent Reynolds Stress, which may be more sensitive than just using the eddy viscosity.

Even though there is a mild sensitivity to the grid for the lagRST model at the edge, the fine grid will be used for all computations since the difference is relatively small in its effect on the separation zone.
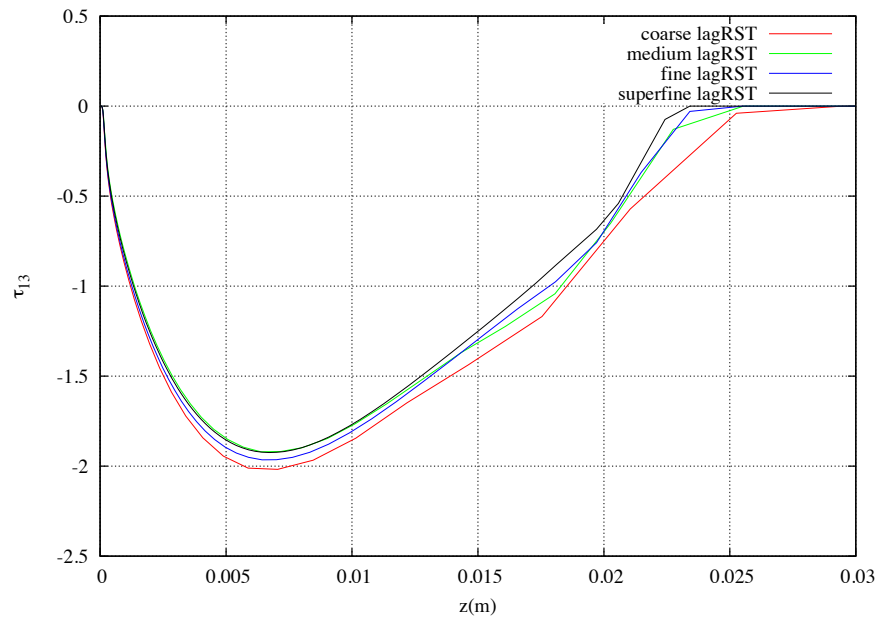
Figure 3.46. Grid convergence plots of τ_{13} for the lagRST model upstream of the interaction (x = -0.076m).
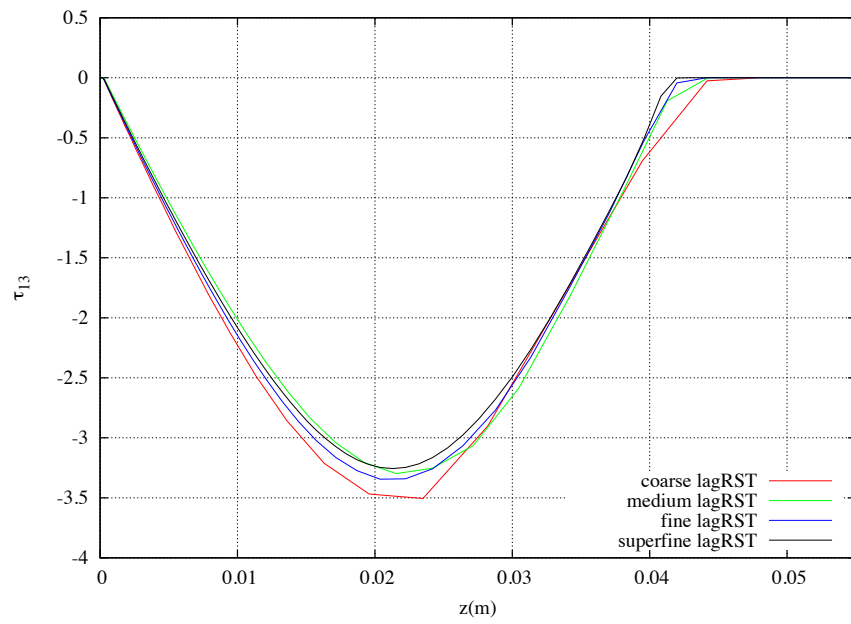
Figure 3.47. Grid convergence plots of τ_{13} for the lagRST model downstream of separation (x = 0.101m).

3.3.3 First Order Assessment

Olsen and Coakley [5] discovered the need to use a 2nd order upwind operator on the turbulence model convective terms to get a grid converged solution. They found that when comparing solutions between their two grids, referred to here are the coarse and fine grids, the 2nd order operator allowed for a near identical answer, while the 1st order operator had some variation. Figure 3.50 and figure 3.51 show the pressure and skin friction for the lagRSTSST model. The pressure comparisons do show a slightly tighter clustering of the 2nd order operator than for the 1st order operator, but it is on a very small scale. The skin friction comparisons show a very slight difference in the re-attachment region, but again the differences are on a very small scale. Although on a small scale, the comparisons do show that for the 1st order the coarse grids have a larger difference from the fine grids than the 2nd order. The fine grids for either order have nearly identical answers.

Based on this data, it seems that running second order terms is worthwhile, only because you can get a more accurate result on a coarser grid. The convergence behavior was not affected for the assessed cases.

Figure 3.48 and figure 3.49 show the pressure and skin friction for the lagRSTSST model. There is no odd behavior for the pressure comparisons for the medium grid for this model. The pressure comparisons do show a slightly tighter clustering of the 2nd order operator than for the 1st order operator, but it is on a very small scale. The skin friction comparisons show a very slight difference in the re-attachment region, but again the differences are on a very small scale. Although on a small scale, the comparisons do show that for the 1st order the coarse grids have a larger difference from the fine grids than the 2nd order. The fine grids for either order have nearly identical answers.
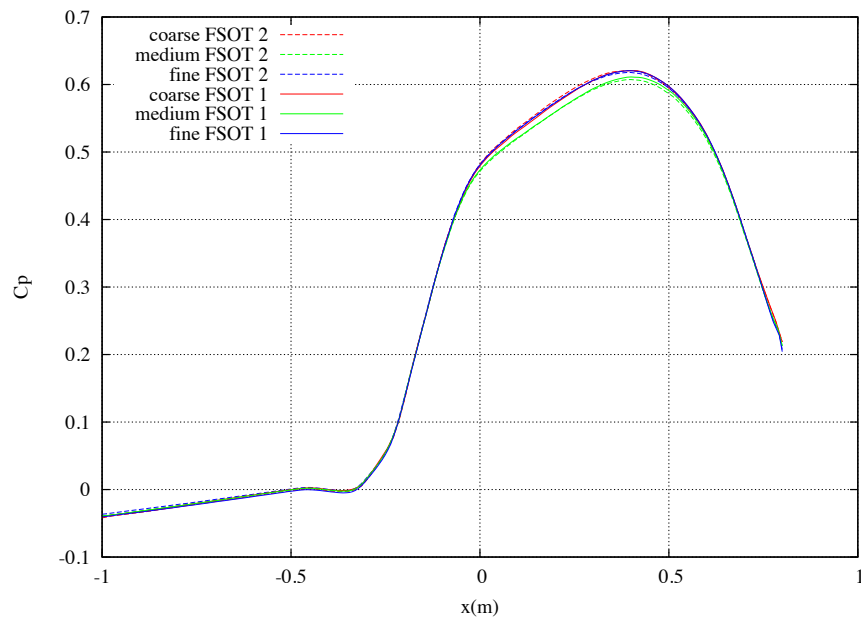
Figure 3.48. Pressure verses x for the lagRST model with first and second order turbulent convective terms.
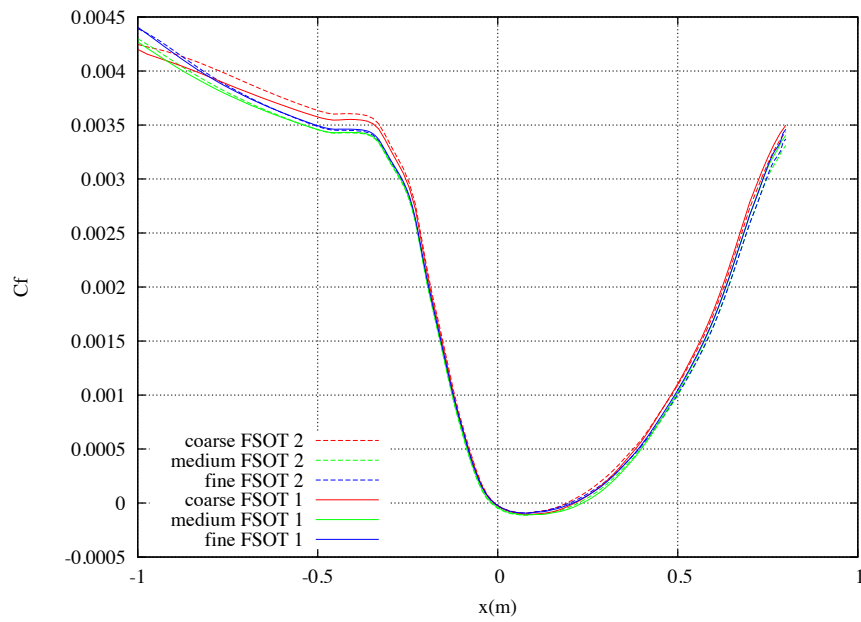
Figure 3.49. Skin friction verses x for the lagRST model with first and second order turbulent convective terms.
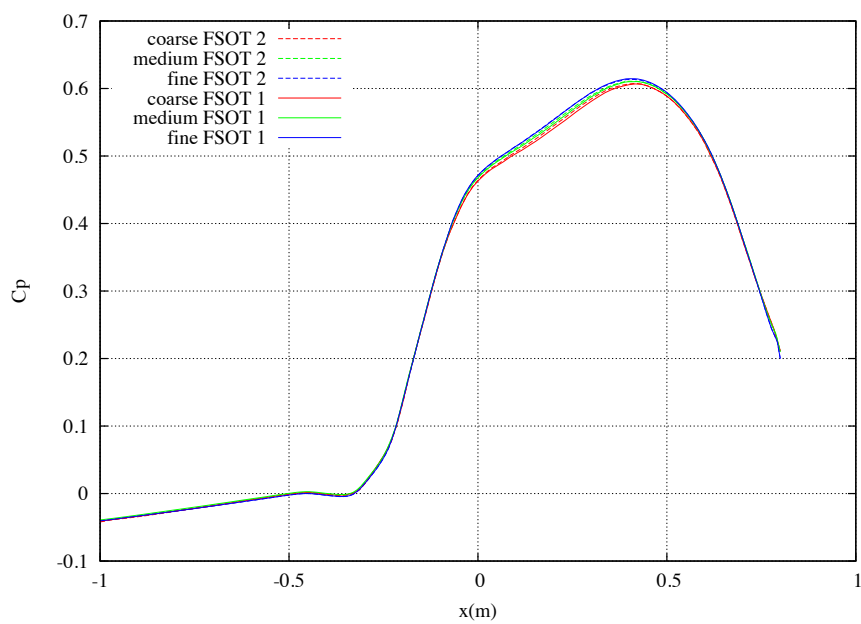
Figure 3.50. Pressure verses x for the lagRSTSST model with first and second order turbulent convective terms.
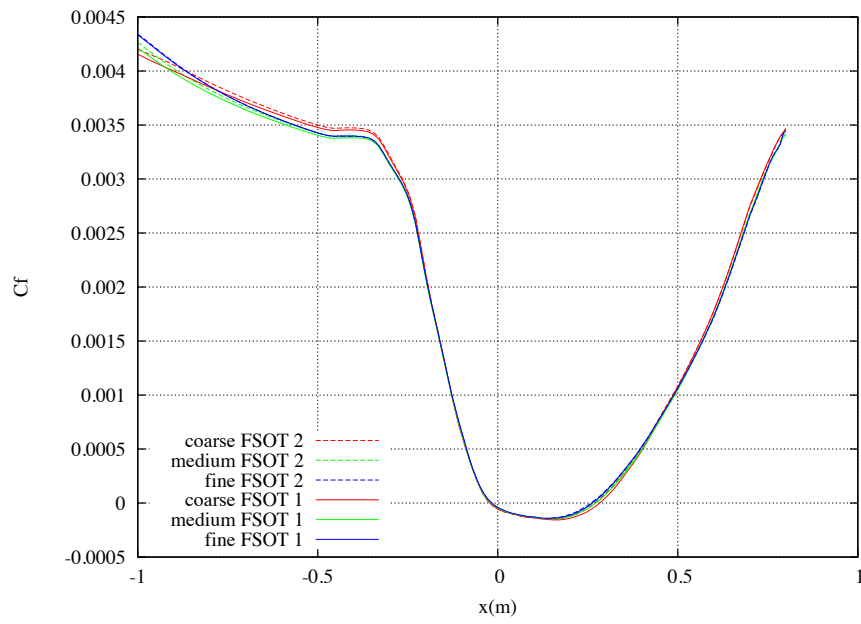
Figure 3.51. Skin friction verses x for the lagRSTSST model with first and second order turbulent convective terms.

3.3.4 Results

In previous sections, the lagRST coefficients have been reduced to three sets of choices. For ease of reference, table 3.3 shows the new naming convention for the lagRST based models for the three different sets of coefficients.

Figure 3.52 shows the pressure distribution verses axial distance for the SST, lag, lagRST, and lagRSTSST models. For the lagRST models, lagRST-2 matches the pressure more accurately. This is the smallest value of a_o, 0.2. However, all the lagRST models are an improvement over the baseline $k - \omega$ model. The lag and lagRST-2 provide the best prediction for these models. The SST based models provide the best overall prediction of pressure. The lagRSTSST model has a lower prediction of pressure in the interaction region than the SST model. Overall, adding the lag equation improves the predictions for the baseline models.

The lagRSTSST model was assess with a lag constant of $a_o = 0.2$ for this case. It had less than a 1% change on the size and location of the separation zone.

lagRST model name	σ_k	a_o
lagRST-1	0.8	0.35
lagRST-2	1.5	0.2
lagRST-3	1.5	0.35

Table 3.3 Model naming convention for lagRST models

Figures 3.53 and 3.54 detail the skin friction distribution on the cylinder. There is insufficient data to exactly characterize the separation zone length using skin friction, so the experimental separation length was determined with oil flow interferometry to be approximately from $x = 30mm$ to $x = 220mm$. This was within $\pm 25mm$ of the mean flow data. Table 3.4 lists the separation and reattachment points as well as separation length for all models.
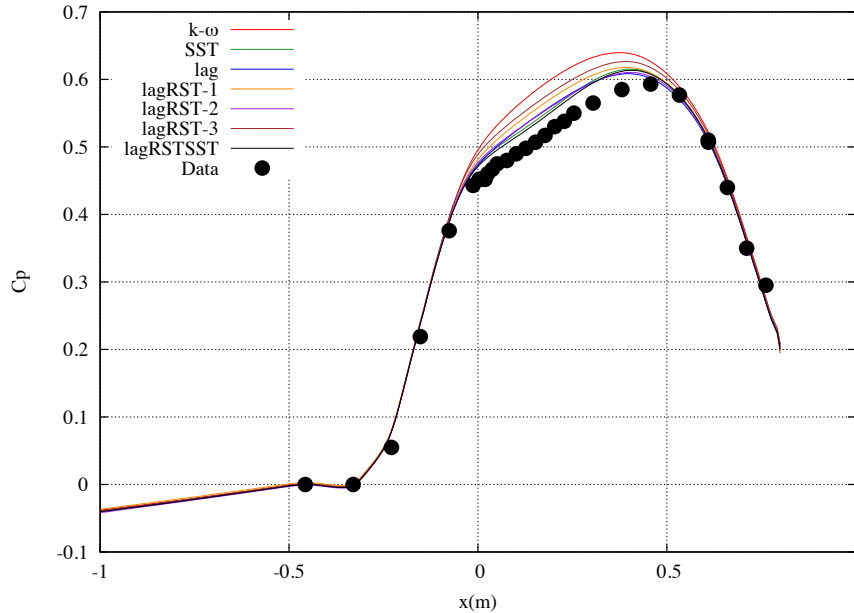
Figure 3.52. Pressure verses x for the lag, lagRST, and lagRSTSST models compared to $k - \omega$ and SST.

All the $k-\omega$ based RST models provide a more accurate separation zone length predic-tion than the SST based models. By far the best comparison comes form the lagRST model with $a_0 = 0.35$ with either value of σ_k chosen (lagRST-1 or lagRST-3). It is interesting to note that the baseline $k - \omega$ model is the only one which predicts a smaller separation zone length. The lagRSTSST model provides the worst separation zone length prediction of any model. The majority of the models do a better job characterizing the reattachment point than they do the separation point. None of the models provide a prediction of the separation point that is lower than 12%, whereas two of the the models provide reattachment below this value.
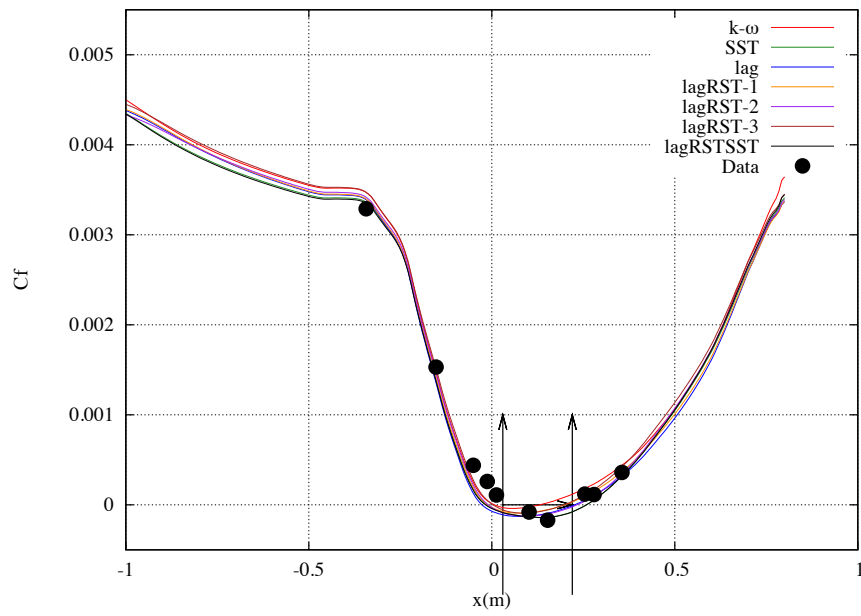
Figure 3.53. Skin friction verses x for lag, lagRST, and lagRSTSST models compared to $k - \omega$ and SST, with the separation noted by arrows.
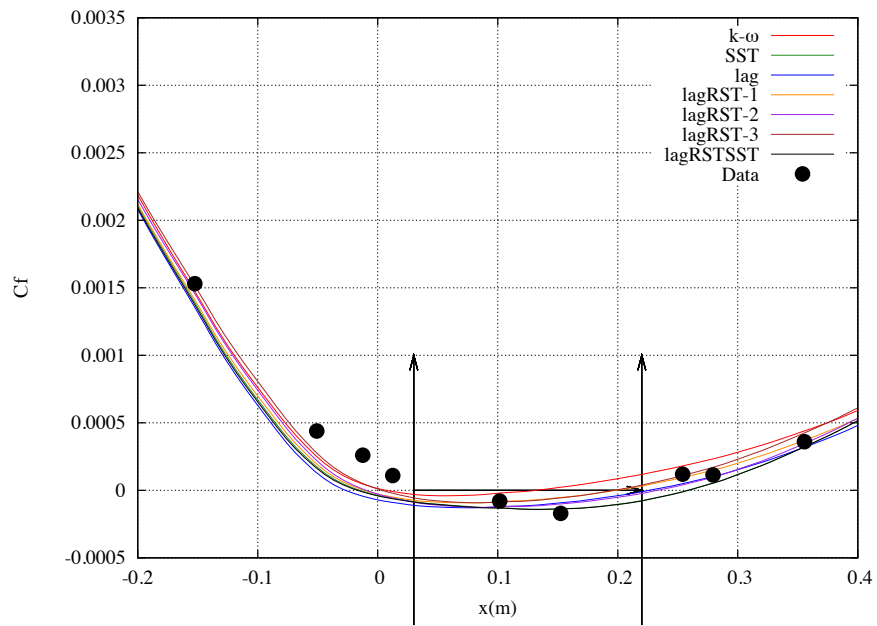
Figure 3.54. Zoomed in view of the skin friction verses x for lag, lagRST, and lagRSTSST models compared to $k - \omega$ and SST.

Model	Separation Point	Reattachment	Zone length
Data	0.03m $\pm$ 0.025	0.22m $\pm$ 0.025	0.19m $\pm$ 0.025
k-ω	0.00708 (-12.1%)	0.131 (-46.6%)	0.124 (-34.5%)
SST	-0.015 (-23.6%)	0.258 (20.0%)	0.273 (43.6%)
lag	-0.0269 (-29.9%)	0.226 (3.16%)	0.253 (33.1%)
lagRST-1	-0.011 (-21.6%)	0.199 (-11.2%)	0.210 (10.4%)
lagRST-2	-0.00955 (-20.8%)	0.233 (6.67%)	0.242 (27.5%)
lagRST-3	0.00328 (-14.1%)	0.197 (-12.2%)	0.194 (1.8%)
lagRSTSST	-0.0168 (-24.6%)	0.259 (20.4%)	0.276 (45.0%)

Table 3.4 Table of data indication location and extent of the separation zone with percent error compared to the tunnel data and non-dimensionalized by the separation zone length (all data values are in meters). A negative percent error indicates the separation or reattachment point occurred too early and the separation zone length is too small. Values larger than 25% are highlighted in red.

(a) x = -0.457m   (b) x = -0.330m
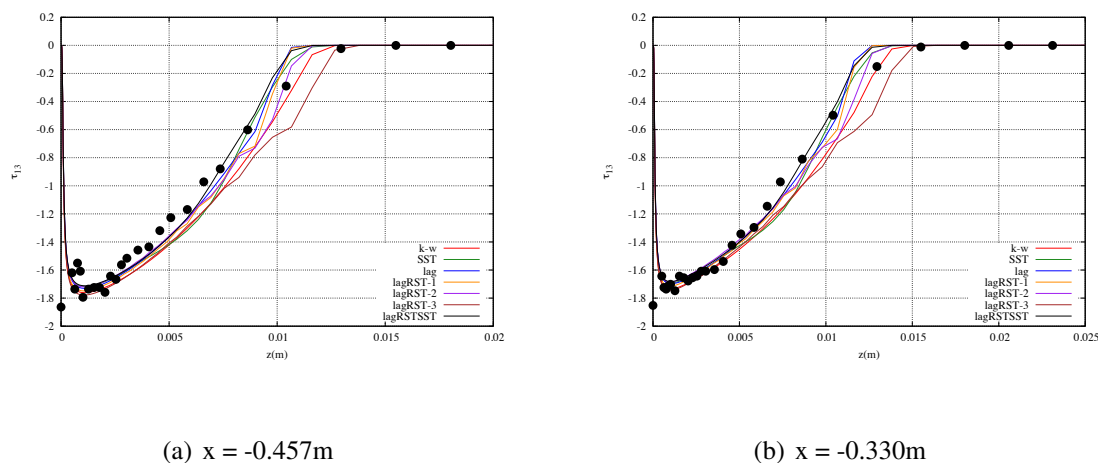
Figure 3.55. τ_{13} Reynolds Stress comparisons in the zero pressure gradient upstream portion of the incoming turbulent boundary layer.

3.3.5 Reynolds Stress Profiles

The next set of figures provide comparisons of the τ_{13} component of the Reynolds Stress tensor at multiple axial locations. The plots are grouped into regions of similar interactions. Figure 3.55 shows the profile upstream of the interaction in the zero pressure gradient region. It is difficult to say which model does the best in this region, although the dependence of the lagRST to the grid at the boundary layer edge is shown here. In general, all the models predict the peak value well. None of the models match the shape of the profile exactly, but the lag, lagRST-1, and lagRSTSST models do not over predict the thickness of the profile.

Figure 3.56 provides the axial locations that are in the adverse pressure gradient portion of the flow upstream of the separated flow region. The lagRST-3 and the lagRSTSST provide the best comparisons to the peak value as the plots approach the separation point. It is worth noting that as separation approaches, the two SST based models have a peak that shifts up in the boundary layer, while the $k - \omega$ based models do not shift quite as quickly. The shift of the peak up into the boundary layer agrees better with the SST based models. The standard SST overpredicts the peak value more than the other models. It is worth

noting that the by adding the lag equations to the baseline SST model, the lagRSTSST model greatly improves the prediction of the peak value. The general behavior of all lag models in this flow type is to reduce the peak value and bring it more in line with the experimentally obtained values.

Figure 3.57 shows the profiles in the separation region. The peak value from the experiment between the three plots matches different models at different locations, so it is difficult to say which model predicts the peak most accurately. The predictions of the peak value location still vary between the two types of models, but near the end of separation the difference gets smaller. However, near the end of the separation zone, the peak value has shifted up in to the boundary layer, thus no model matches the distribution correctly. The baseline SST model over predicts the peak value approximately 20%.

Figure 3.57 shows the profiles in the re-attachment region. The experimental data shows a much broader curve than any of the predictions do. The SST based models tend to get closer to the peak value, but the spread in the profile is too small for all the models. The lag based models have an affect on the baseline, but it is to reduce the peak value, which heads away from the experimental data for this position.
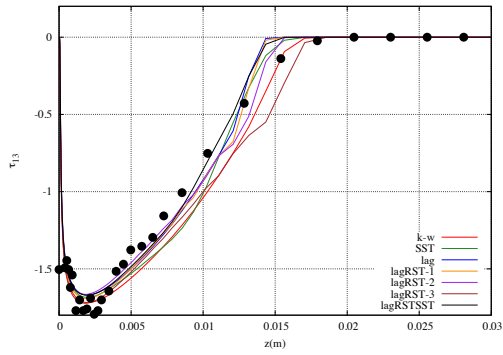
(a) x = -0.228m
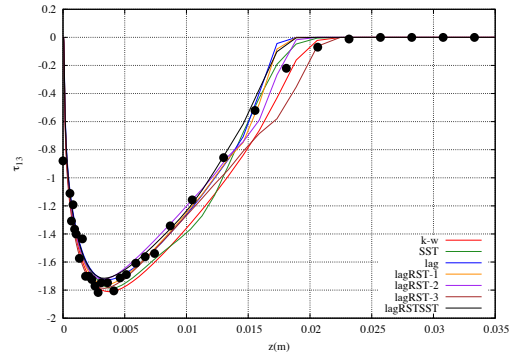
(b) x = -0.152m
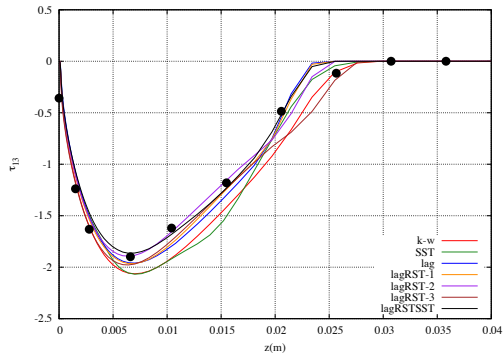
(c) x = -0.076m
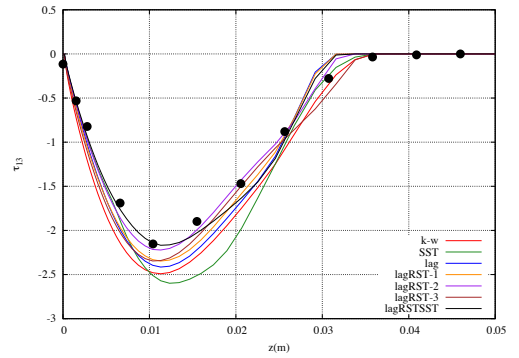
(d) x = -0.012m
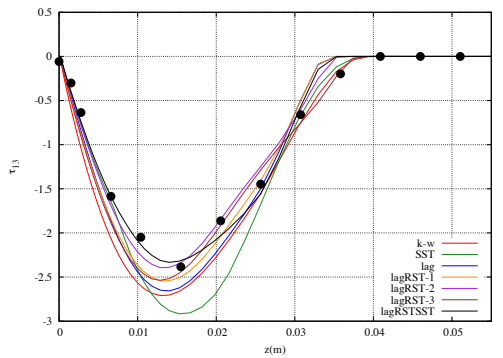
(e) x = 0.012m
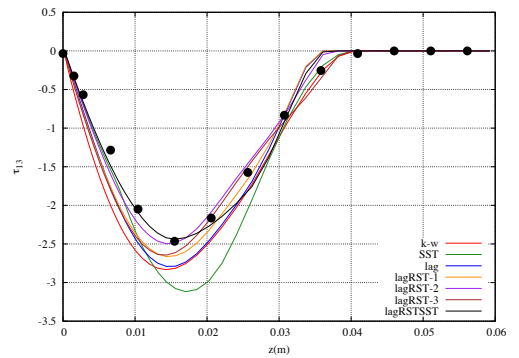
(f) x = 0.025m

Figure 3.56. τ_{13} Reynolds Stress comparisons in the adverse pressure gradient portion upstream of separation.
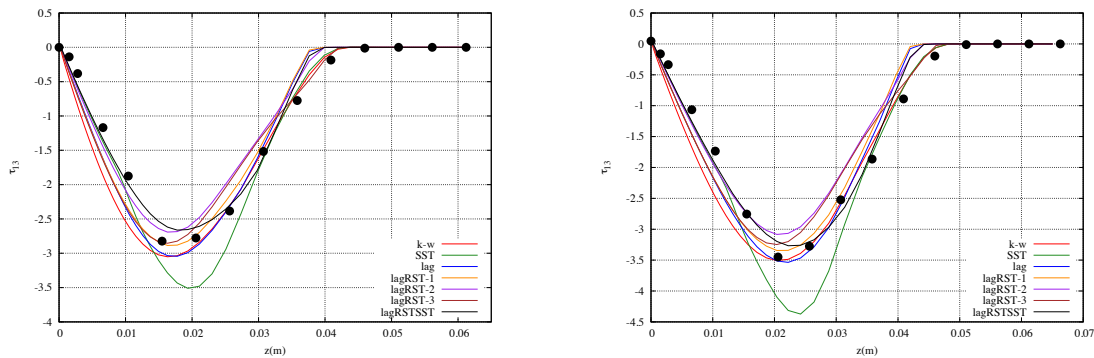
(a) x = 0.050m

(b) x = 0.101m
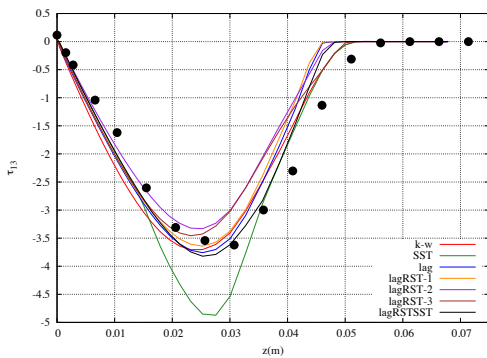
(c) x = 0.152m

Figure 3.57. τ_{13} Reynolds Stress comparisons in the separated portion of the boundary layer.
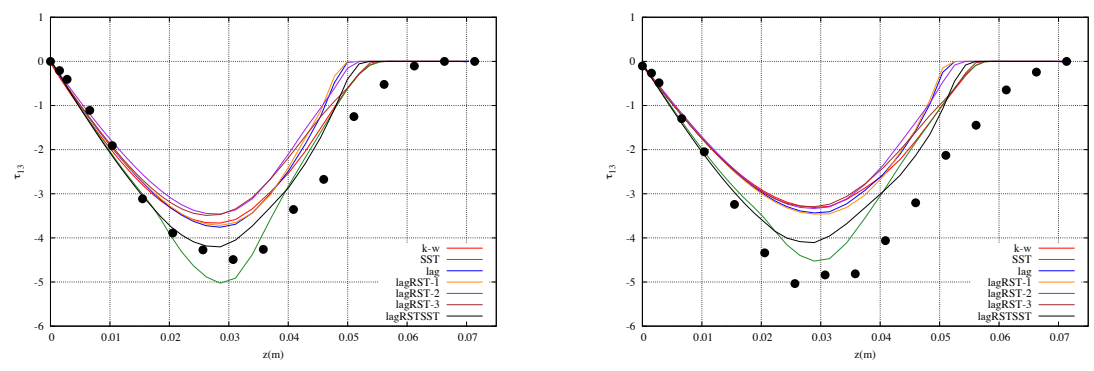
(a) x = 0.228m

(b) x = 0.304m

Figure 3.58. τ_{13} Reynolds Stress comparisons in the reattached portion of the boundary layer.

3.4 Transonic Bump

This test case, done by Bachalo and Johnson [50], is a transonic interaction on an axisymmetric cylinder with a circular arc bump. The upstream boundary conditions were constant total pressure and temperature, with static pressure allowed to vary and velocity direction aligned with the cylinder axis. The outer edge of the flowfield was extended approximately 10 bump cord lengths away from the cylinder surface and utilized a characteristic boundary condition. The viscous wall was no-slip adiabatic with the downstream static pressure held at p_{inf}. To maintain consistency with Olsen and Coakley [5], the upstream length of the cylinder was maintained at they value they used, which provided a boundary layer thickness of approximately 1 cm at the location of the bump, which was the same approximate thickness measured in the test.

3.4.1 Grid Convergence

Three grids were chosen for this case. A coarse grid with dimensions of 96 (axial) by 101 (off-body), medium grid with dimensions 192 by 151, and a fine grid with dimensions 390 by 201. Wall spacings that translated to y^+ values less than 0.2, 0.1, and 0.05 were used for the coarse, medium, and fine grids, respectively.

Figure 3.59 shows the pressure comparisons for the lagRST-1 model for the various grid resolution cases. Figure 3.60 is the same figure only zoomed in on the interaction region. The medium and fine grid give nearly identical results. The other models (lagRST-2, lagRST-3, and lagRSTSST), all had similar convergence behavior, if not better. The medium grid provides adequate grid convergence for this test case.

Figure 3.61 shows the pressure comparisons for the lagRSTSST model for the various grid resolution cases. Figure 3.62 is the same figure only zoomed in on the interaction region.
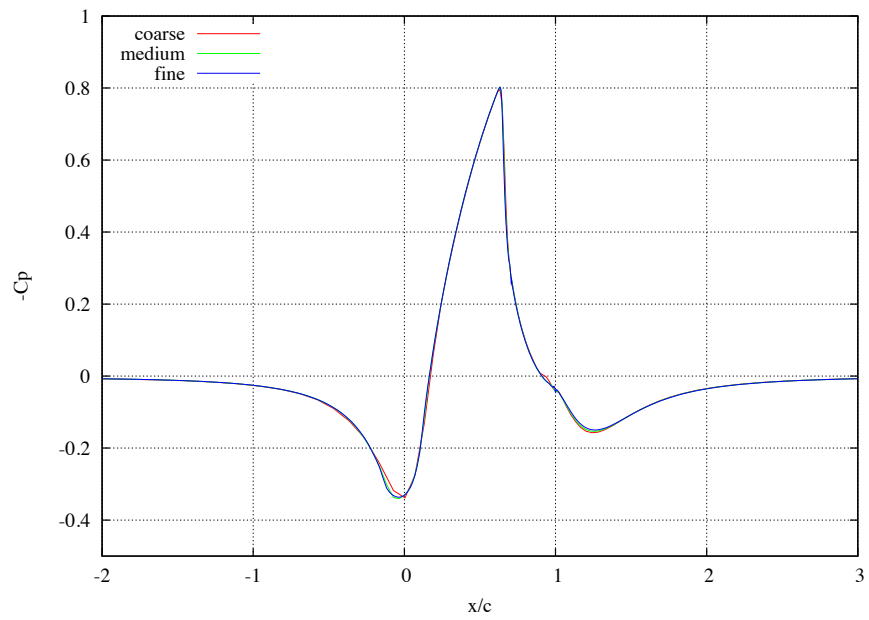
Figure 3.59. Pressure plots for the lagRST-1 model showing grid convergence.
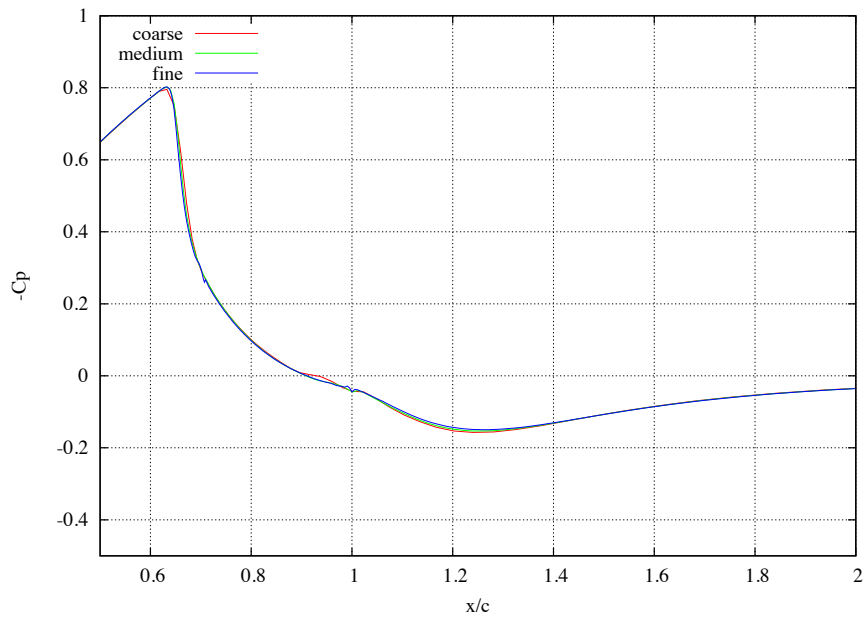
Figure 3.60. Pressure curves for the lagRST-1 model showing grid convergence zoomed in on the separation zone.
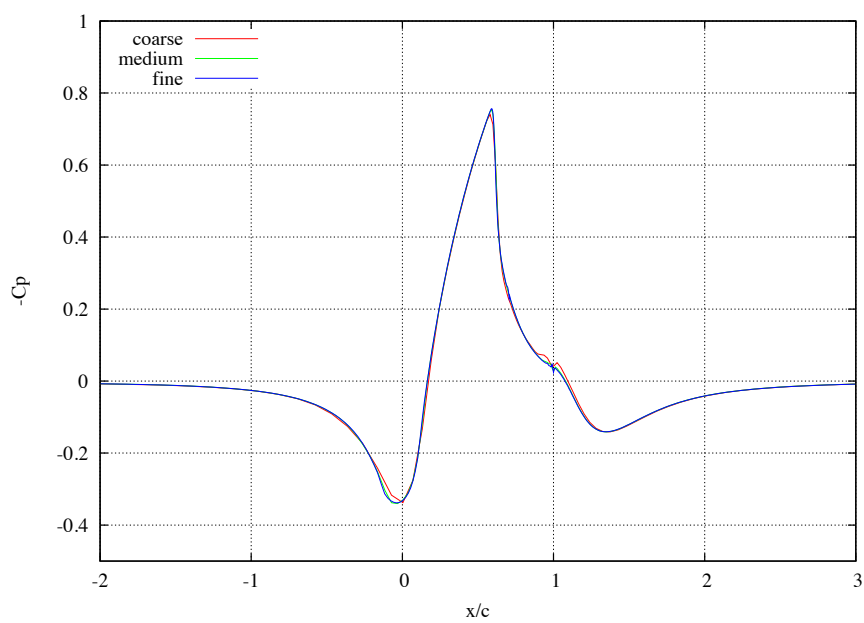
Figure 3.61. Pressure plots for the lagRSTSST model showing grid convergence.
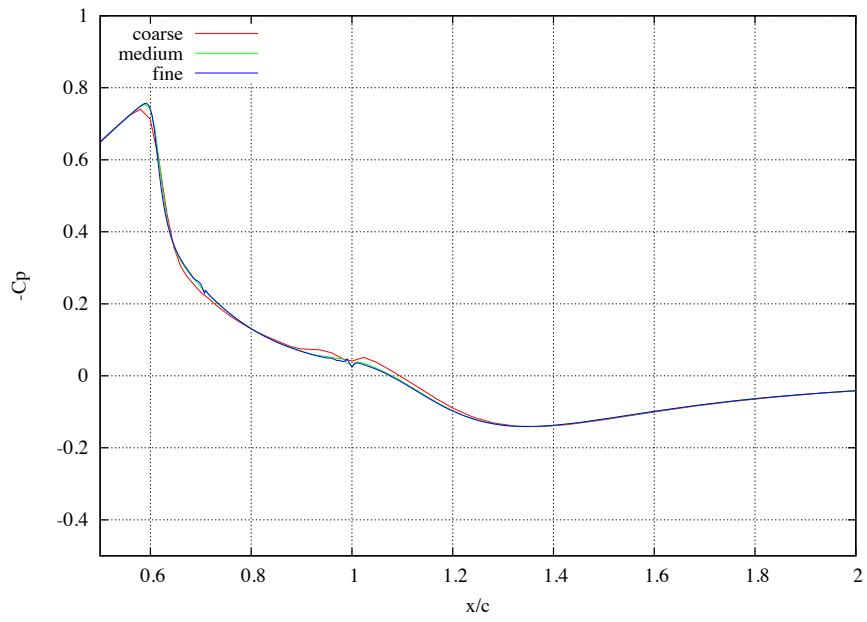
Figure 3.62. Pressure curves for the lagRSTSST model showing grid convergence zoomed in on the separation zone.

Velocity Profiles

Figure 3.63 shows the velocity profile upstream of the bump for the lagRST-1 model for the various grid resolutions. Figure 3.64 shows the velocity profile downstream of reattachment. All other models showed similar convergence behavior. The medium grid again provides excellent grid convergence.
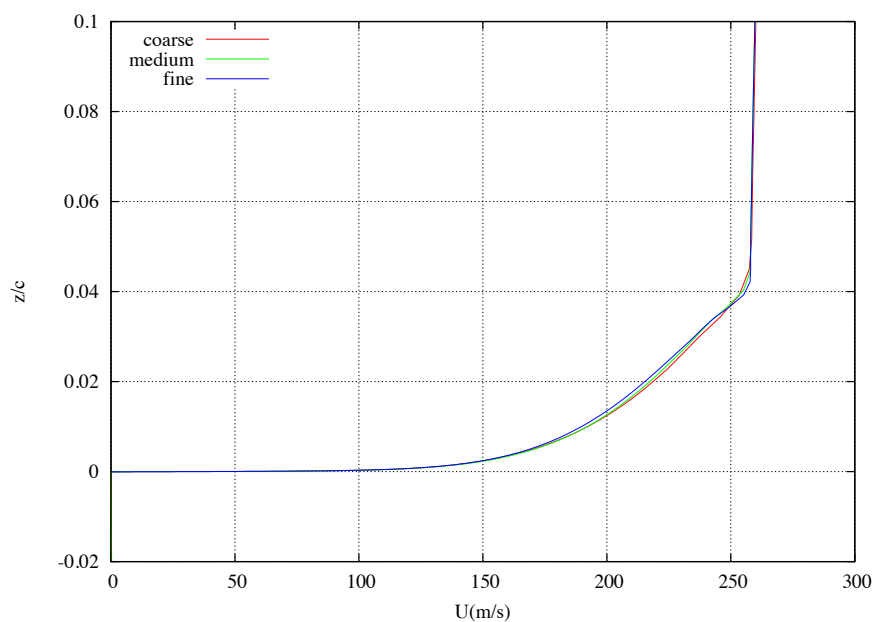
Figure 3.63. Velocity profiles for the lagRST-1 model showing grid convergence upstream of the bump.
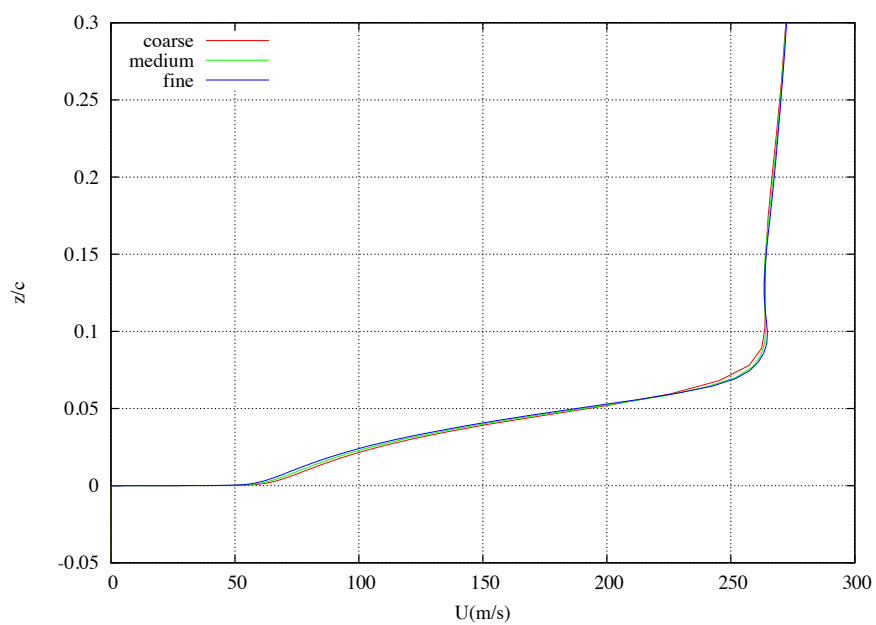
Figure 3.64. Velocity profiles for the lagRST-1 model showing grid convergence downstream of the separation zone.

Reynolds Stress Profiles

Figure 3.65 shows the τ_{13} Reynolds Stress profile upstream of the bump for the lagRST-1 model for the various grid resolutions. Figure 3.66 shows the velocity profile downstream of reattachment. The grid convergence between the medium and the fine grid is much better for this case than for previous test case. However, the sensitive behavior at the edge which keeps the profiles from having a smooth transition outside the boundary layer edge is still apparent. All other models had similar, if not better grid convergence. The medium grid again provides adequate grid convergence.
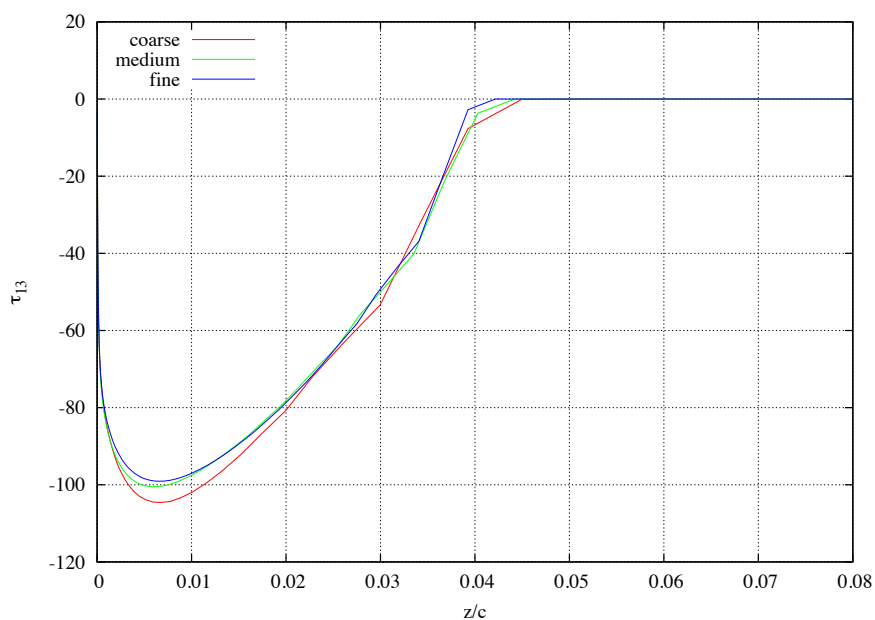
Figure 3.65. Reynolds stress profiles for the lagRST-1 model showing grid convergence upstream of the bump.
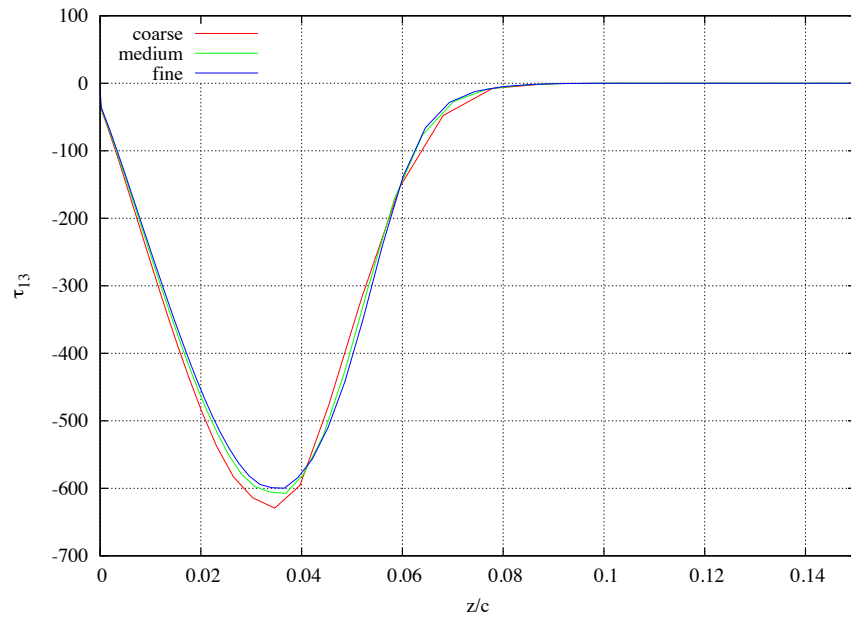
Figure 3.66. Reynolds stress profiles for the lagRST-1 model showing grid convergence downstream of the separation zone.

3.4.2 Results

Figure 3.67 shows the pressure comparisons for the lagRST based models as well as the k-ω, SST, and lag models. Figure 3.68 shows the same data, just zoomed-in on the interaction region. The prediction of the shock location for all the models shows some large variations. The two outliers are the k-ω and the lagRSTSST models. The k-ω predicts a very late shock location and the lagRSTSST predicts it very early. The SST and the lagRST-2 models give nearly identical answers. They predict a slightly upstream location for the shock. The lag and lagRST-1 also give nearly identical answers to each other, and provide a very accurate prediction of the shock location. The lagRST-3 also gives a very accurate shock location.

None of the models predict the right pressure behavior in the separation zone ($x = 0.71m - 1.1m$). The lagRSTSST model has the closest comparison. However, none of the models predict the steep drop off in pressure just after re-attachment that is present in the experimental data.

Besides shock location, perhaps the more important comparison to make is of the separation zone length. Table 3.5 shows the observed separation and attachment points as well as separation zone lengths and the associated values for these for each turbulence model. As of the abstract submission, error bars on the experimental observations have yet to be identified (noted as "x" in Table 3.5). The table indicates the k-ω model provides an accurate prediction of the separation zone, but this only refers to the extent of the separation. Previous figures have shown that the pressure prediction in the separation zone from this model is under predicted. The lag and lagRST-1 models provide the best characterization of the separation zone length, with the worst comparisons coming from the SST and the lagRSTSST models. The lagRST-3 and lagRST-2 models (which both use a larger value of σ_k), also have a large error in the prediction. The lagRSTSST model was assessed with a lag constant value of $a_o = 0.2$. This had no effect on separation and less than 0.1% change on the separation zone length and position.
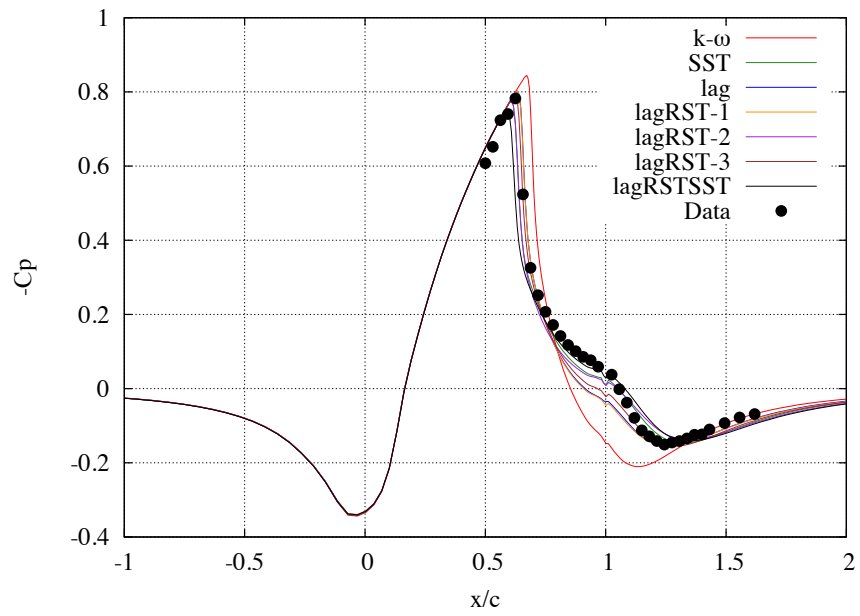
Figure 3.67. C_p verses axial location for all turbulence models compared to the experimental data.
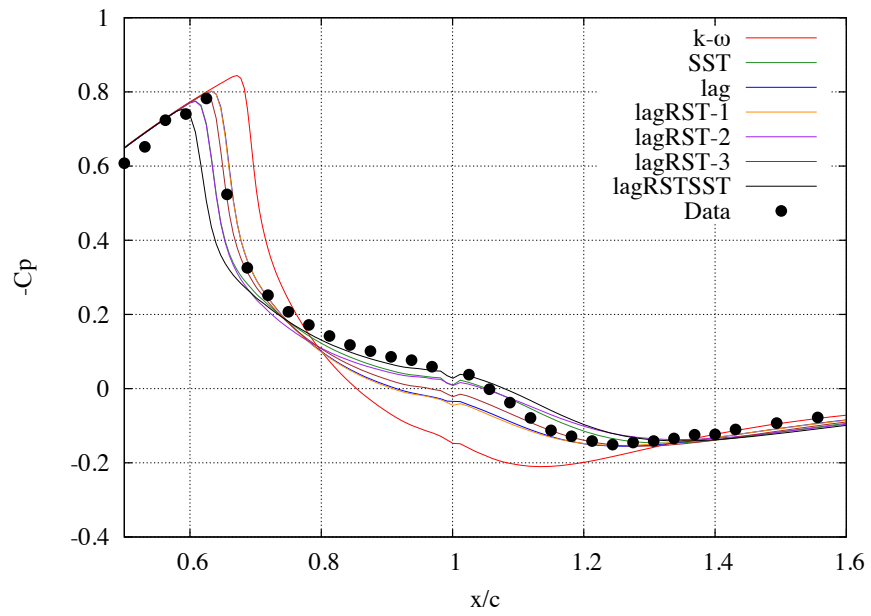
Figure 3.68. Zoomed in view of C_p verses axial location for all turbulence models compared to the experimental data.

Model	Separation Point	Reattachment	Zone length
Data	$0.71 \pm x$	$1.1 \pm x$	$0.39 \pm x$
k-ω	0.701 (-3.03%)	1.05 (-13.8%)	0.346 (-10.8%)
SST	0.645 (-17.4%)	1.18 (21.6%)	0.539 (39.0%)
lag	0.666 (-11.9%)	1.12 (4.64%)	0.452 (16.6%)
lagRST-1	0.668 (-11.4%)	1.12 (4.14%)	0.210 (10.4%)
lagRST-2	0.646 (-17.1%)	1.19 (21.9%)	0.539 (39.1%)
lagRST-3	0.659 (-13.7%)	1.15 (12.5%)	0.5 (26.3%)
lagRSTSST	0.632 (-20.8%)	1.19 (23.3%)	0.556 (44.1%)

Table 3.5 Table of data indication location and extent of the separation zone with percent error compared to the tunnel data. The percent error is nondimensionalized by the separation zone length for consistency. A negative percent error indicates the separation or reattachment point occurred too early and the separation zone length is too small. Values over 25% are highlighted in red.

(a) x/c = -0.250

(b) x/c= 0.563

(c) x/c= 0.625
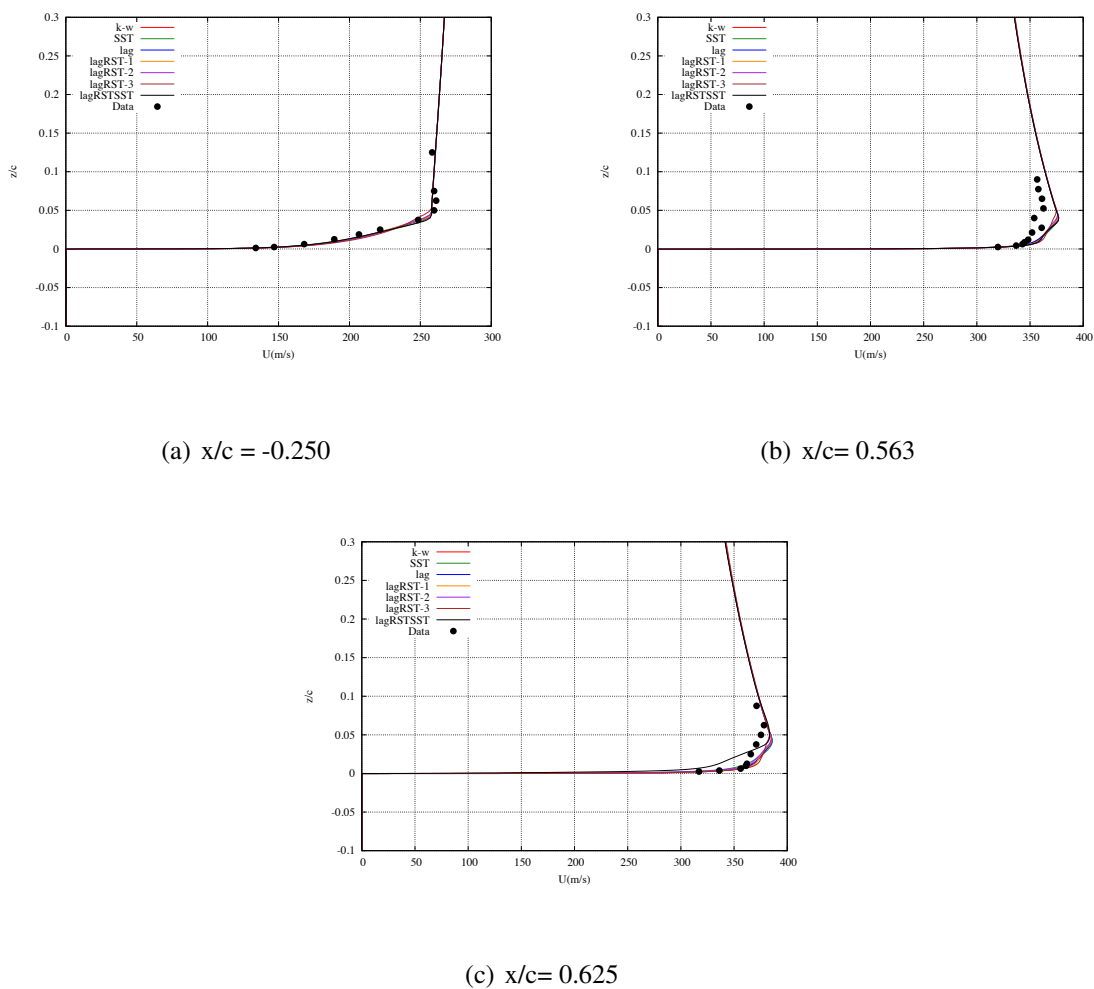
Figure 3.69. Velocity profile comparisons upstream of the shock.

U-velocity profiles

Figure 3.69 shows the velocity profiles for all the turbulence models upstream of the shock location. Note that the lagRSTSST model predicts the shock very close to $x/c = 0.625$, so there is a noticeable change in the velocity profile in figure 3.69(c) that is not evident in the other models. All of the other models have very similar profiles in this region.

Figure 3.70 shows the velocity profile near the shock location. It is evident here that many of the models do a poor job of predicting the shock location. The lagRSTSST, lag, and lagRST-2 have the shock too far upstream, whereas the $k - \omega$ has the prediction too far downstream. This same behavior was noted in the C_p profiles. The lagRST-1 and lag models have the closest prediction to the experimental data, but the curvature of the profile is not as steep as indicated in the experimental data.
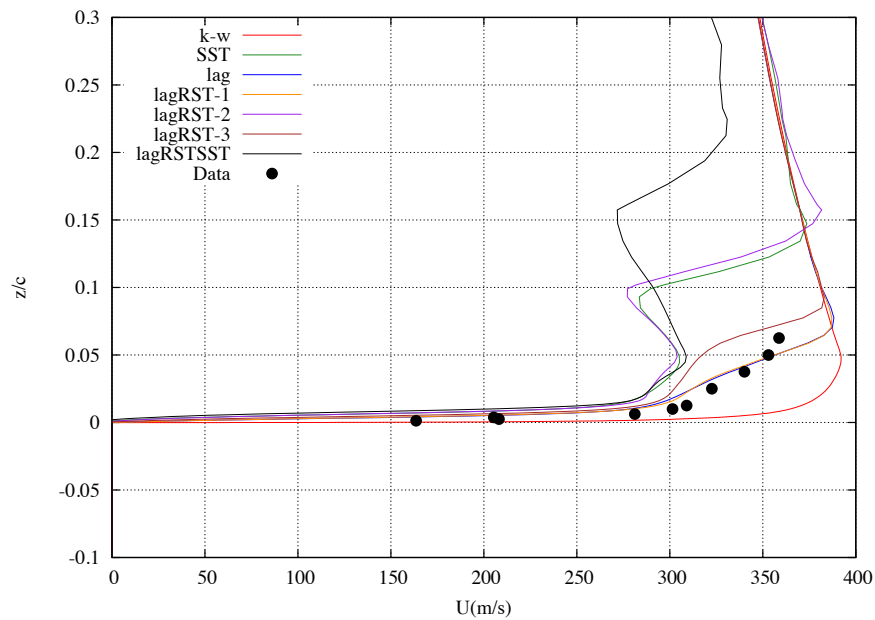
Figure 3.70. Velocity profile near shock x/c = 0.688

Figure 3.71 shows the velocity profile comparisons downstream of the shock. It is evident from figure **??** that the $k-\omega$ model has the shock positioned near this location, because the velocity profile is not well behaved as the other models are. In general, the remaining models have similar behavior. The lagRSTSST predicts the highest velocity near the edge of the interaction and the lagRST-1 predicts the lowest velocity. This correlates with the

(a) x/c = 0.750   (b) x/c= 0.813
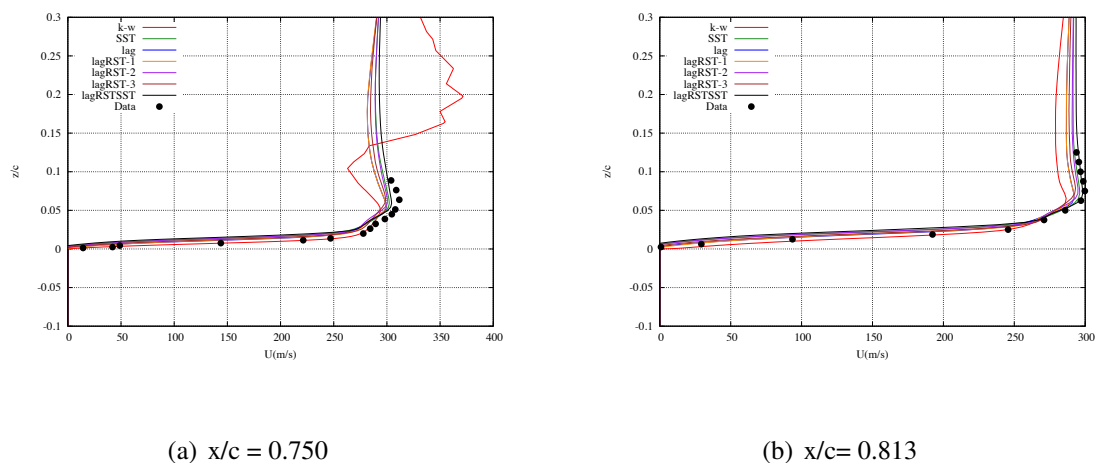
Figure 3.71. Velocity profile comparisons downstream of the shock.

pressure predictions in the interaction region, shown in figure 3.68. The lagRSTSST had the highest pressure and the lagRST-1 had the lowest.

Figure 3.72 details the velocity profiles for all the models in the separation zone. The $k-\omega$ model has a large under prediction of the velocity. However, the remaining models all predict the shape of the profile and all get within 5% of the peak velocity. The lagRSTSST has the most accurate profile shape of the models, especially near the boundary layer edge.

Figure 3.73 shows the velocity profiles for all the models downstream of the separation zone. Figure 3.73(a) shows the $k-\omega$ model provides the worst comparison while the other models tend to all do about the same. Figure 3.73(b) shows that the $k-\omega$ tends to match the behavior near the wall better while the other models tend to match the behavior near the boundary layer edge. Figure 3.73(c) shows profiles that continue this trend, as the $k-\omega$ model provides excellent comparisons near the wall and does about as well as the other models near the edge. It is hard to differentiate between the other models in this particular region.

Figure 3.73
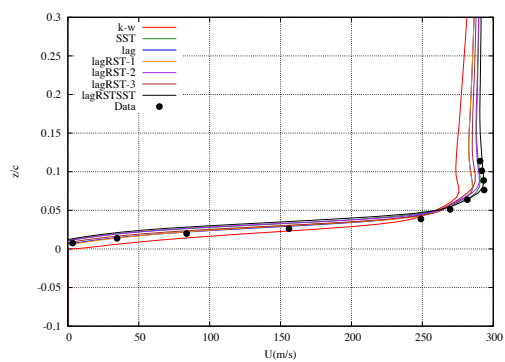
(a) x/c = 0.875
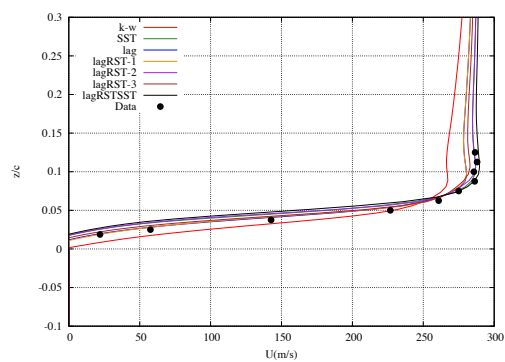
(b) x/c=0.938
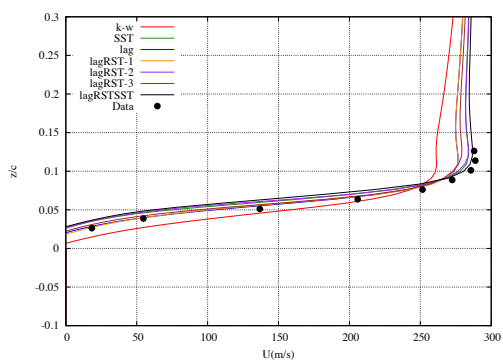
(c) x/c= 1.0

Figure 3.72. Velocity profiles in the separation zone.
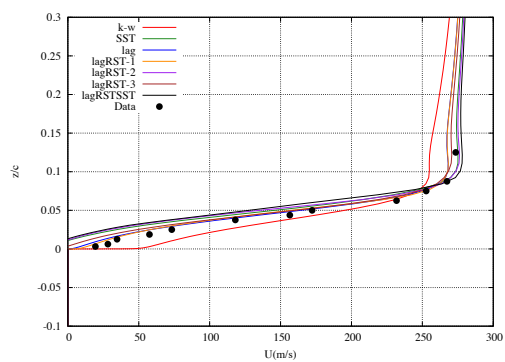
(a) x/c = 1.125
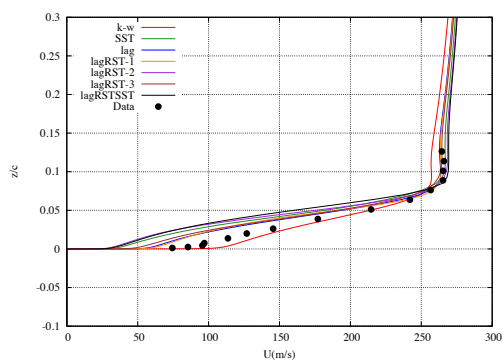
(b) x/c= 1.250
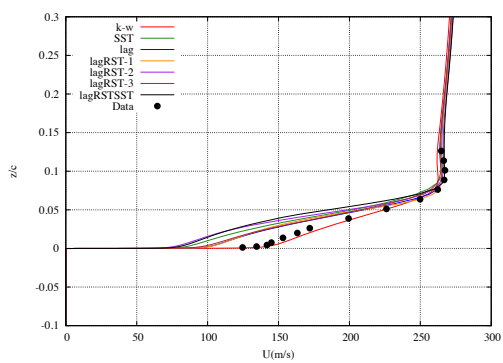
(c) x/c= 1.375

Figure 3.73. Velocity profiles downstream of the separation zone.

RST profiles

Figure 3.74 shows the τ_{13} Reynolds Stress profile upstream of the experimentally observed shock. Figure 3.74(a) shows the profile in the constant pressure gradient portion of the incoming turbulent boundary layer. All of the models predict a thinner profile and predict a lower peak than the experimentally observed values. Figures **??** and 3.74(c) show the profiles in the positive pressure gradient portion. For both axial positions, the models predict the profile shape near the wall well, but out towards the edge of the boundary layer and outside it, the data does not match the profiles. It is difficult to draw any conclusions based on these profiles because of the poor agreement. The Reynolds Stress lag models do change the behavior of the τ_{13} profile shape near the edge. These models reach a local minimum like the experimental data does, and then they do increase in value again to have a second local maximum. This does follow the trend in the wind tunnel data. The equilibrium models do not show this second peak. The experimental data does not behave as anticipated at higher values of $\frac{x}{c}$, as it does not go to zero.

Figure 3.75 shows the τ_{13} profile near the experimentally observed shock location. The turbulence models all predict near the same peak value (except the SST model), but the location of this peak value is variable for all models. This is consistent with the shock prediction location seen in the pressure profiles. The models with the worst prediction of the shock location tend to have the largest variation from the experimental peak location. The Reynolds Stress lag models do again predict the second local maximum as seen in the experimental profiles, but it does not match the experimental data.

Figure 3.76 details the τ_{13} Reynolds Stress downstream of the shock but upstream of the experimentally observed separation zone. The experimental data does go to zero outside the boundary layer, contrary to its behavior upstream of the shock wave. For these locations, the equilibrium baseline models get closer to the experimentally observed peak than the lag models. The $k - \omega$ model has the best prediction of the shape. This is not expected because the $k - \omega$ model had the worst predictions for the velocity profiles and the C_p for this region. The remaining predictions are all clustered around the same values.

(a) x/c = -0.250

(b) x/c= 0.563

(c) x/c= 0.625
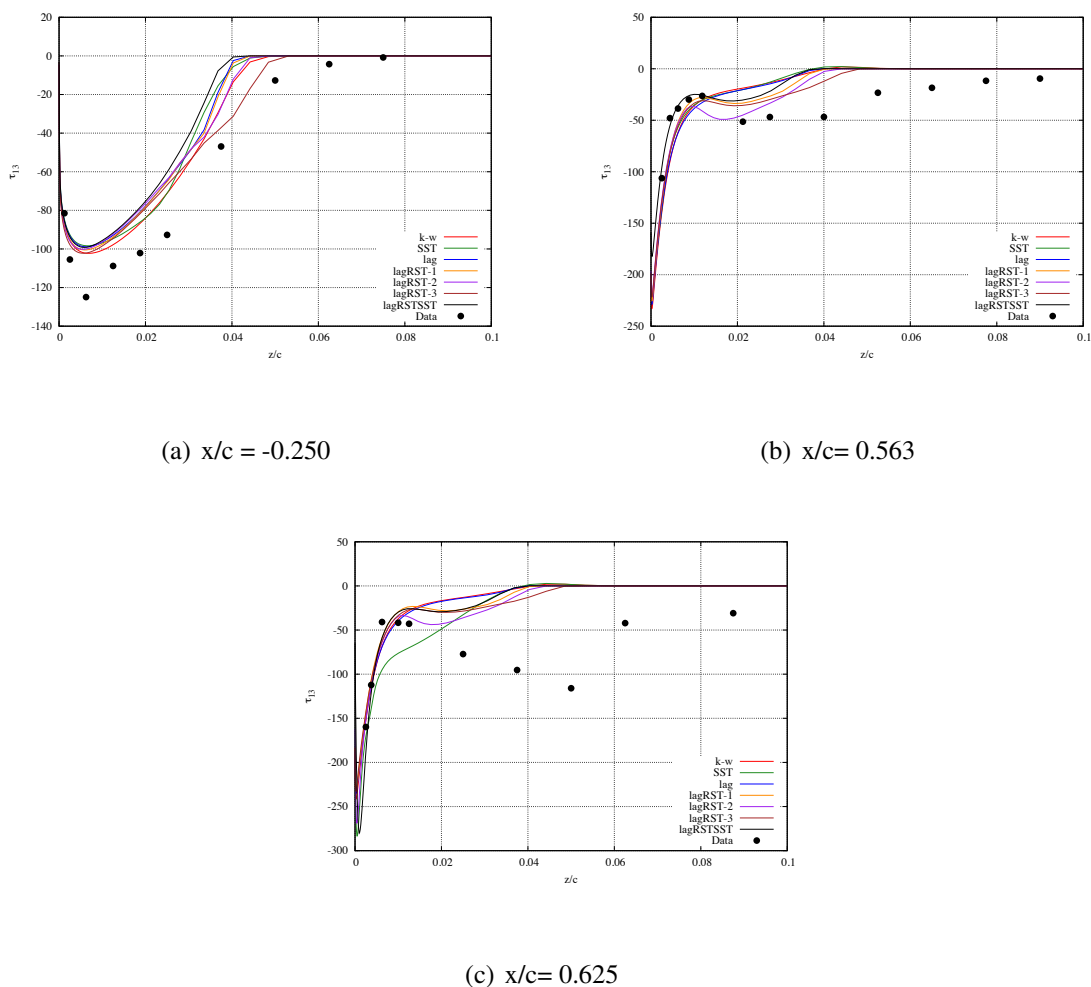
Figure 3.74. Reynolds Stress profile comparisons upstream of the shock.

Figure 3.77 compares the predictions to the experimentally observed value of τ_{13} in the separation zone. For all three locations, all the computations do a poor job of predicting the peak value. The $k - \omega$ model predicts the peak location too close to the wall, whereas the remaining models predict it near the same location. The lagRSTSST model does shift the peak away from the wall slightly more than the lagRST based models. The lagRST based models seem to have the best prediction of this location of the peak.

Figure 3.78 shows the final three τ_{13} Reynolds Stress comparisons, downstream of reattachment. Figure 3.78(a) still has the same large under prediction that the separation zone
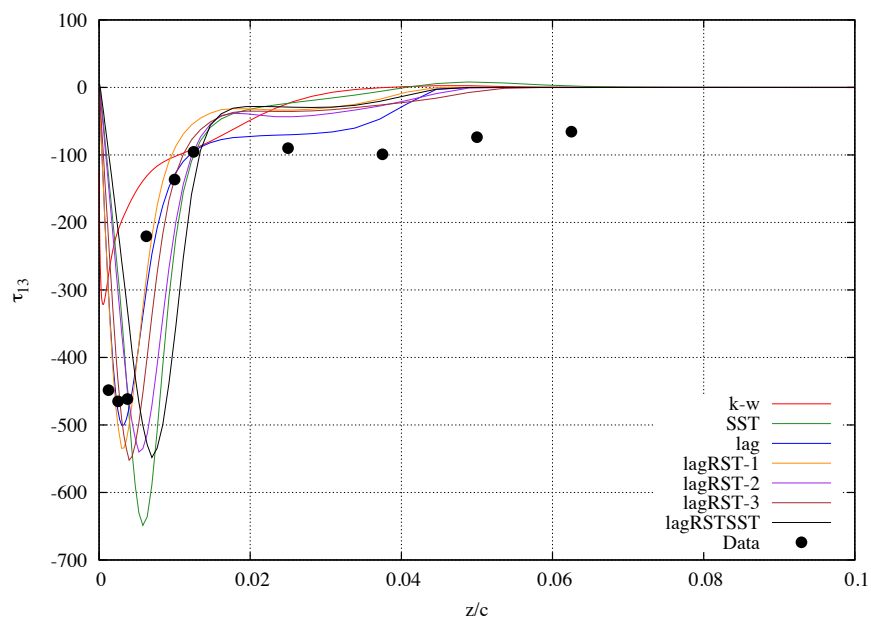
Figure 3.75. Reynolds Stress profile near the experimentally observed shock.
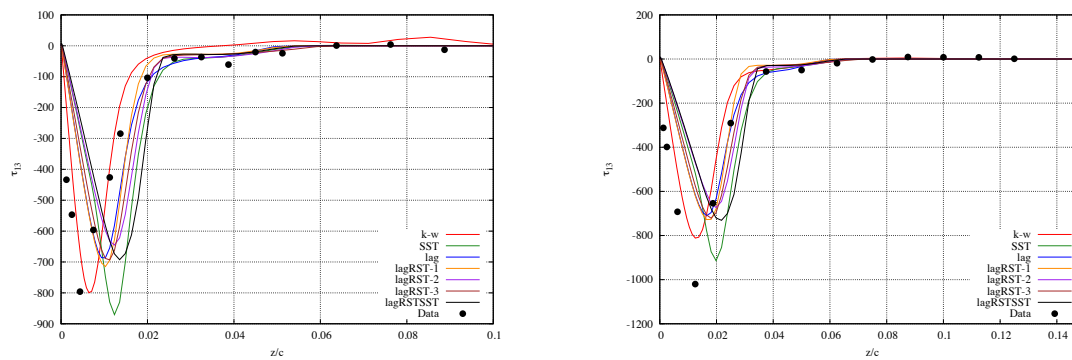
(a) x/c = 0.750

(b) x/c= 0.813

Figure 3.76. Reynolds Stress profile comparisons downstream of the shock.

(a) x/c = 0.875

(b) x/c=0.938

(c) x/c= 1.0
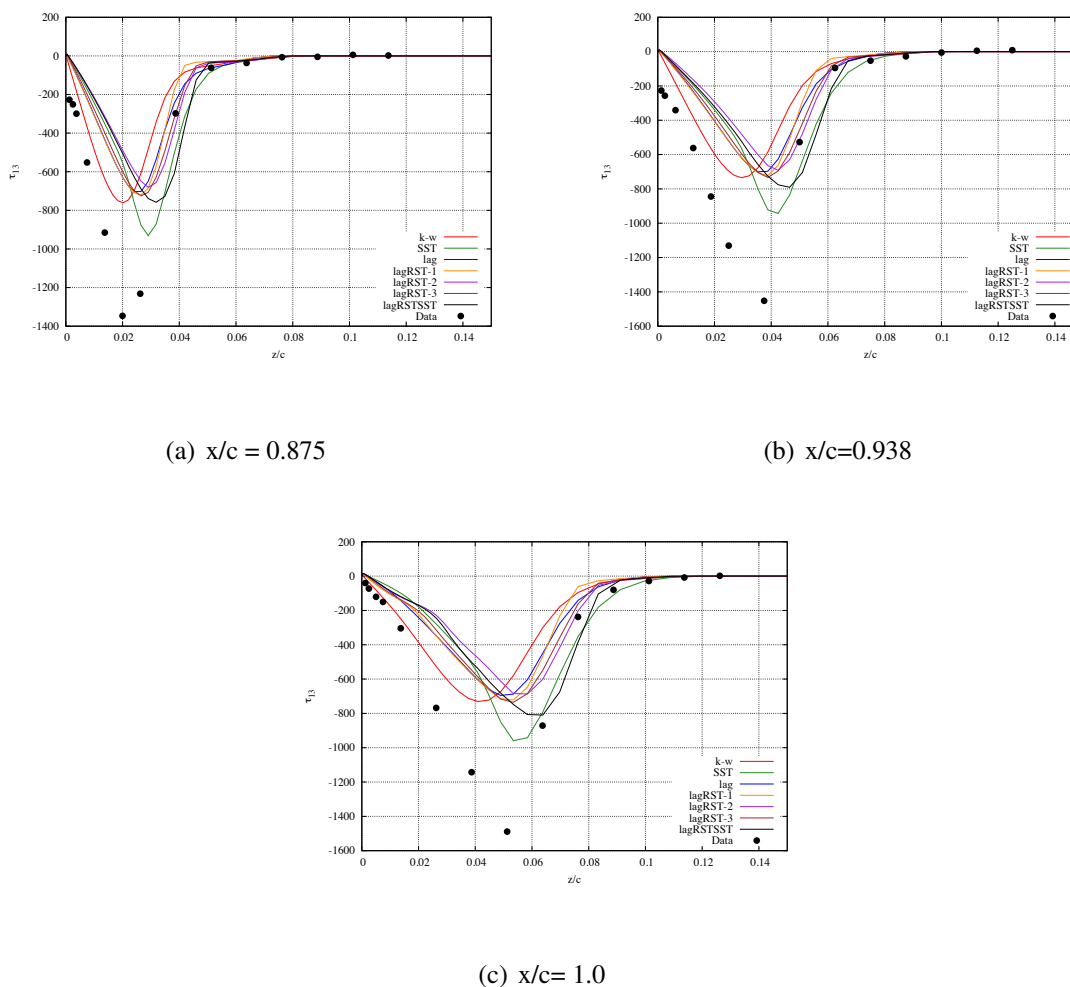
Figure 3.77. Reynolds Stress profiles in the separation zone.

plots had. Figures 3.78(b) and 3.78(c) provide much better comparisons. The SST based models predict the peak to within about 10%, but have the peak value too high in the boundary layer. There is little difference between the SST and the lagRSTSST models here. The $k - \omega$ based models all predict lower values of the peak, but have the peak prediction location near the experimentally observed value. The lagRST based models do predict a higher peak value than the lag and $k-\omega$ models do, even the best prediction is low by around 25%. However, this error does get smaller as the location gets further away from the reattachment point.
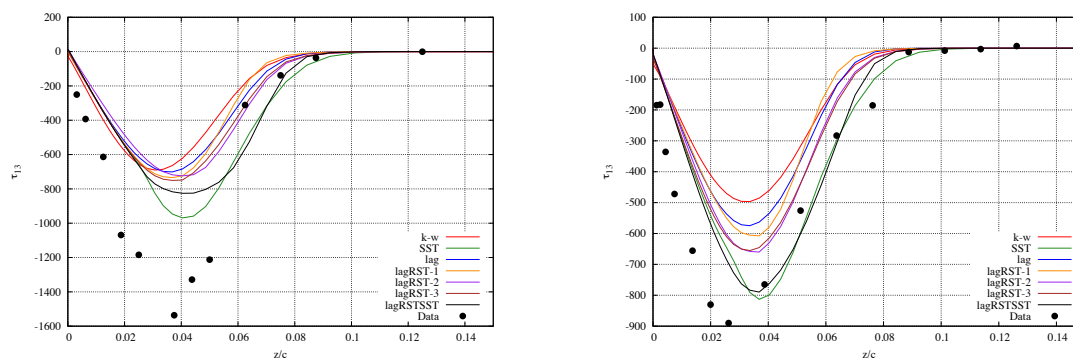
(a) x/c = 1.125

(b) x/c= 1.250
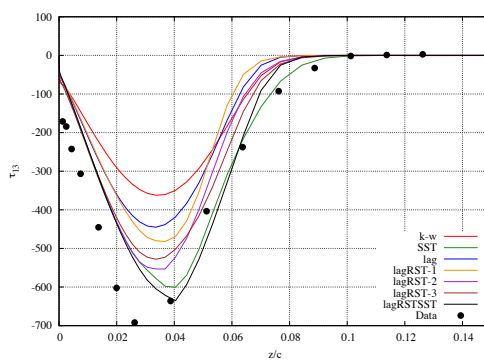
(c) x/c= 1.375

Figure 3.78. Reynolds Stress profile donwstream of the separation zone.

4. Major Test Cases

4.1 Shock Impinging on a Turbulent Boundary Layer

Schulein [40, 41] conducted a ($M_\infty = 5$) wind tunnel test in the DLR Gottingen Ludwieg Tube facility, using air as the test gas. The nominal freestream conditions for this test are listed in table 4.1. The measured values included wall pressure, skin friction (by an oilflow technique), and wall heat transfer (infrared camera measurements and semi-infinite wall gages). The quoted experimental uncertainties are approximately 2% for pressures, 10% for skin friction, and 20% for heat flux. The upstream boundary layer was fully developed and assessments by Brown [21] show that it adheres to standard turbulent correlations.

Condition	Value
P_T	2.12 MPa
T_0	410K
T_w	300K
Re/m	$36x10^7$
U_∞	830 $\frac{m}{s}$
$H_{0,\infty}$	0.41 $\frac{MJ}{kg}$

Table 4.1 Nominal test conditions for Schulein's experiment.

Schulein tested four configurations, starting from a 2D nominal zero-pressure gradient flat plate boundary layer and then adding a shock generator with 3 different angles, $6°$, $10°$, and $14°$. Brown [21] did an exhaustive study of all three angles and provided recommendations for which cases to run. Other comparisons to this dataset are available in the literature, including Fedorova et al. [95] and Steelant [96]. For this study, the 2D boundary layer will be assessed to ensure proper momentum thickness matching and quality of the

upstream profile before the interaction. Then the only shock generator angle to be assessed will be the $14°$ case. This case is fully separated.

An issue that plagues most cases that have this configuration is the shock generator is not relatively "long" compared to the nominal boundary layer thickness. This allows the expansion waves that emanate from the tail of the shock generator to interfere with the separation region, making the interaction more complex and not allowing for the various topological features of the SWTBLI flowfield to develop. Schulein was able to have a $\frac{L_{gen}}{\delta_0} \approx 1000$, which is a large enough ratio to provide ample space for the interactions to set up.

4.1.1 Grid System

The initial grid system was identical to the set ran by Brown [21]. Table 4.2 gives the dimensions and y^+ values for each grid system provided by Brown. Figure 4.1 shows the grid for the $14°$ SWBLI, where flow would be from left to right. The blue line indicates the viscous wall of the shock wave generator. The adjacent boundary conditions to the shock generator were set to inviscid walls, and the opposite wall was set to a viscous, isothermal wall.

Grid System	streamwise	offbody	y^+
coarse	529	129	0.1
medium	1057	257	0.05
fine	2113	513	0.025

Table 4.2 Grid dimensions and y^+ values for the nominal set of grids.
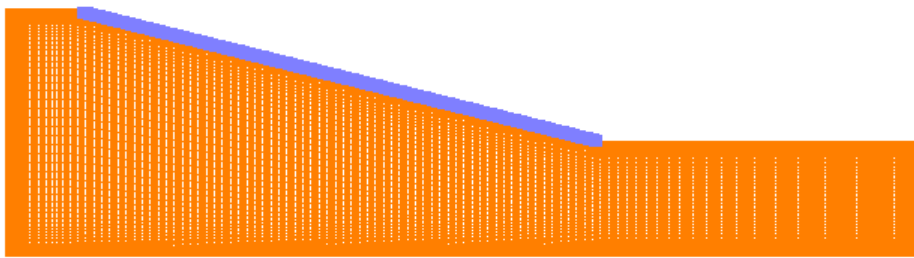
Figure 4.1. Coarse grid for the $14°$ SWBLI case (blue line indicates the shock generator).

4.1.2 Flat Plate Boundary Layer Results

This cases will follow the standard method used in all other cases. The incoming turbulent boundary layer will be generated on the actual geometry by transitioning the simulation in order to match the momentum thickness calculated from the obtained velocity profiles. This is not the method Brown [21] used, as he numerically set the transition point based on the experimentally observed location. This method did not work in OVERFLOW, as there is no way to control the transition zone length. In particular, each turbulence model behaves differently in this transition zone, which made the results vary based on the model. Therefore, the previous method of setting the transition point to match the experimentally provided θ was used. The main reason this method is used is to provide the best estimate of the of the incoming turbulent boundary layer coming into the interaction region.
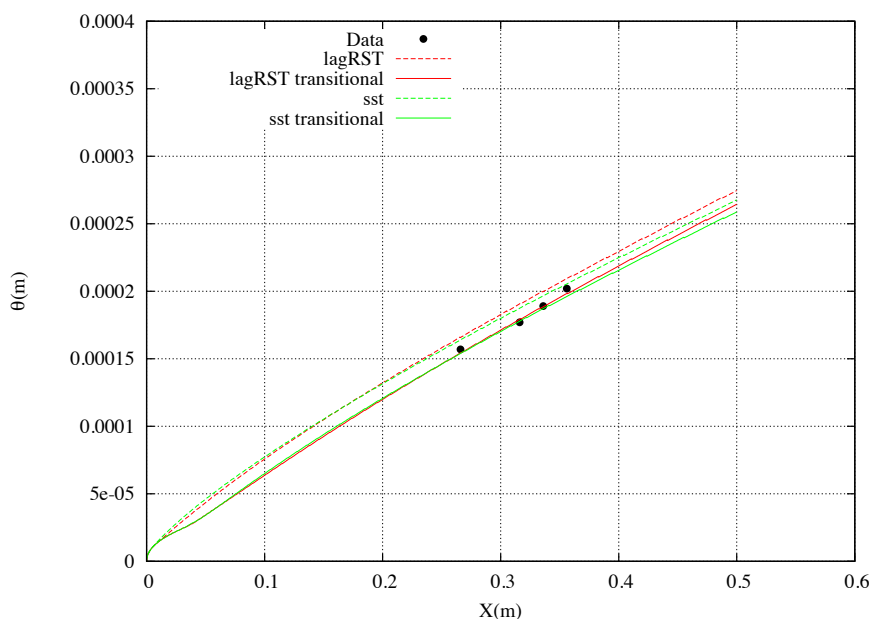
Figure 4.2. Momentum thickness verses axial distance for the sst and lagRST-1 models compared to Schulein's 2D boundary layer data.

Figure 4.2 shows the matching process for the SST and lagRST-1 models. The dashed lines are the fully turbulent cases while the solid lines have been tripped to match θ. Both cases were transitioned at different axial locations in order to match θ. The same process was done for all other turbulence models, but will not be shown here.

Figure 4.3 shows the skin friction for the tripped and fully turbulent profiles. The data has a very large transitional overshoot and transition zone. This again shows the difficulty in actually predicting the transition zone and further justifies θ matching. This profile shows that once sufficiently downstream, the tripping process makes little difference on the value of skin friction (shown by the small differences between the dashed and solid lines of the same color). As previously discussed, each model behaves quite differently around the trip location. In fact, the red and green dashed lines show that even fully turbulent cases behave differently, in regards to where the simulation actually goes turbulent. Even though this behavior exists, for this case the Reynolds number is sufficiently high that downstream of the interaction, the transition effects on skin friction are minimal. The simulations both underpredict the skin friction, but Brown [21] observed the same behavior.

Figure 4.4 shows the heat flux for the same profiles. Unlike skin friction, the simulation predictions go through the scatter in the data. The same behavior downstream exists much like skin friction, where the transitioning of the simulation has little effect on the downstream data comparisons.
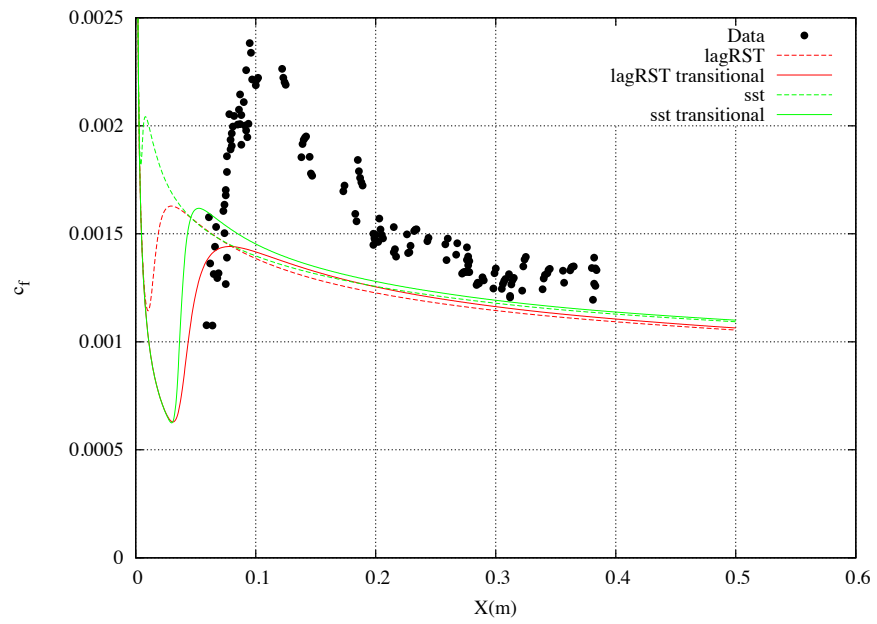
Figure 4.3. Skin friction coefficient verses axial distance for the sst and lagRST-1 models compared to Schulein's 2D boundary layer data.
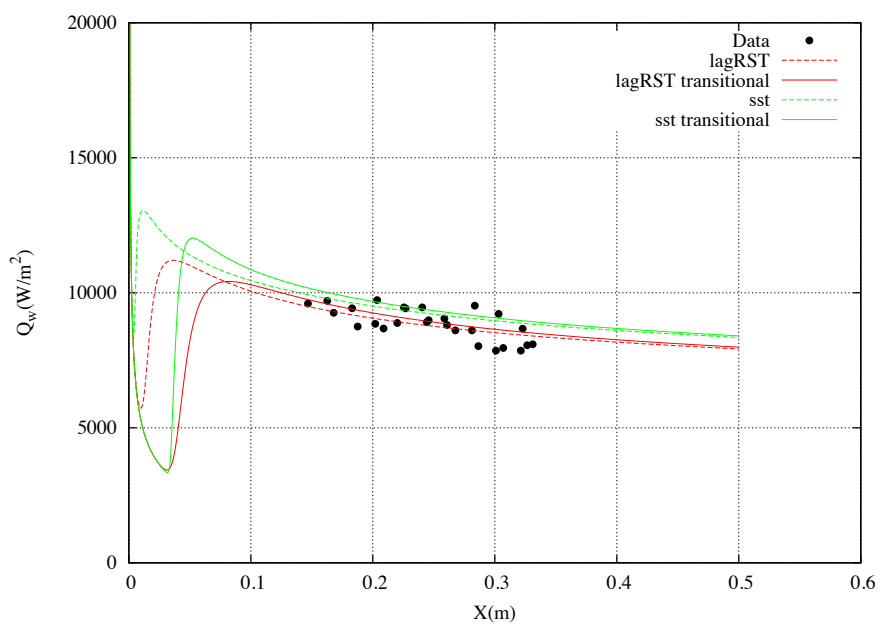
Figure 4.4. Heat flux verse axial distance for the sst and lagRST-1 models compared to Schulein's 2D boundary layer data.

4.1.3 Grid Convergence

The baseline set of grids ran for this case were provided by Brown [21]. The dimensions were previously listed in table 4.2. All grid resolution cases were ran fully turbulent, as to avoid sensitivities to transition location and the transition zone. Figure 4.5 shows the pressure distribution or all three grids for the SST model. The medium and fine grid show excellent grid convergence, even for the separation location. Figures 4.6 and 4.7 shows the skin friction and heat flux for the same cases. For all plots, the medium and fine grids provide excellent grid convergence behavior.
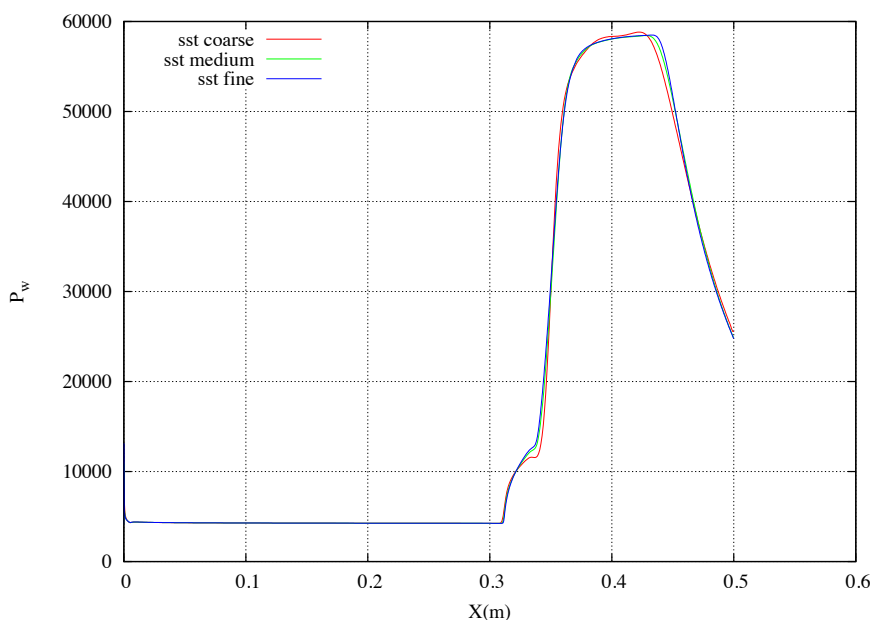
Figure 4.5. Pressure distribution for the SST model for the coarse, medium, and fine grid.

Although the SST model obtained grid convergence with the medium and fine grid, the lagRST-1 model did not have the same properties. Figure 4.8 shows the pressure distribution for the lagRST-1 model on all three grids along with two other grids that will be discussed. The coarse, medium, and fine grids don't converge, in fact the difference
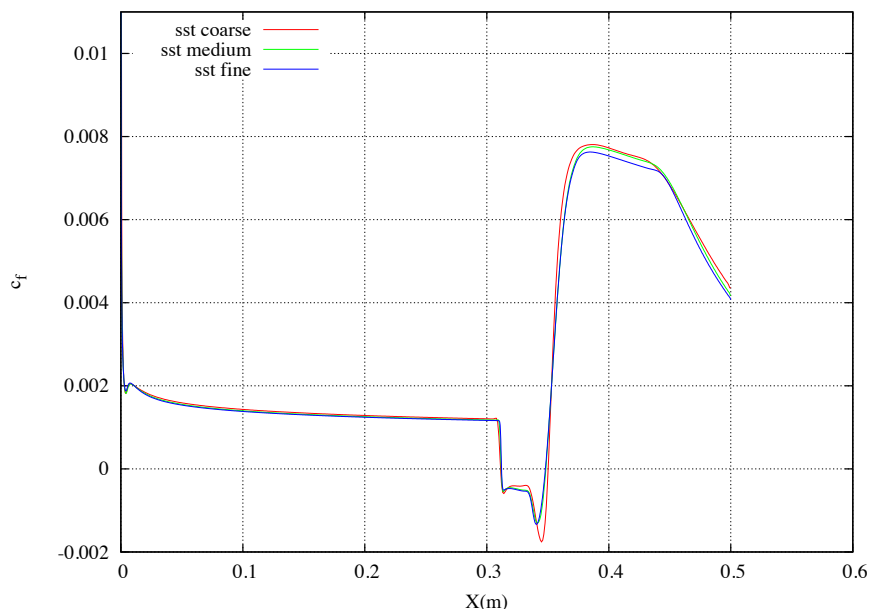
Figure 4.6. Skin friction distribution for the SST model for the coarse, medium, and fine grid.

between the lines gets larger as the grid is refined. After this result was obtained, it was determined that doubling the grid again off of the fine grid would most likely cause numerical issues with OVERFLOW (this is typically the case when the grid has more than 500 points in the boundary layer), so a focused grid was built to assess this. Even though the medium grid is very fine in the streamwise direction, it was apparent that the shock impinging on the wall could be diffused because it was crossing the grid lines diagonally. The lagRST model could be more sensitive to this since Reynolds Stresses are being modeled and now just eddy viscosity. The Reynolds Stress model will be more sensitive to a complicated Strain field than an eddy viscosity model, i.e. less variation to resolve. To test this, a modified grid system was developed. The grid labeled "shock grid" was built by taking the baseline fine grid and then re-clustering the streamwise points around the shock and the interaction zone. This is labeled "shock grid medium" in the plots. That grid was then doubled in the
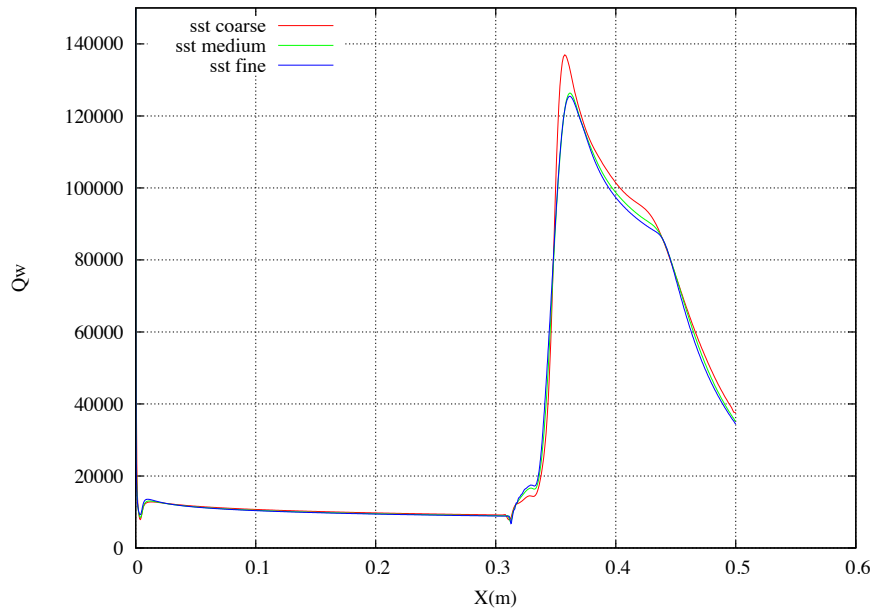
Figure 4.7. Heat flux distribution for the SST model for the coarse, medium, and fine grid.

streamwise direction only and labeled "shock grid fine". Figure /ref905gc1 clearly shows that the baseline fine grid and the two new grids converge to the same profile.

Figures 4.9 and 4.10 show the skin friction and heat flux for the same cases. These results show the same general trends as figure /ref905gc1. The baseline fine grid is grid converged.

Based on these results, the fine grid will be used for data analysis. Note that although not shown here, the SST model was assessed for the two "shock grids" and the same convergence behavior was obtained as shown above.
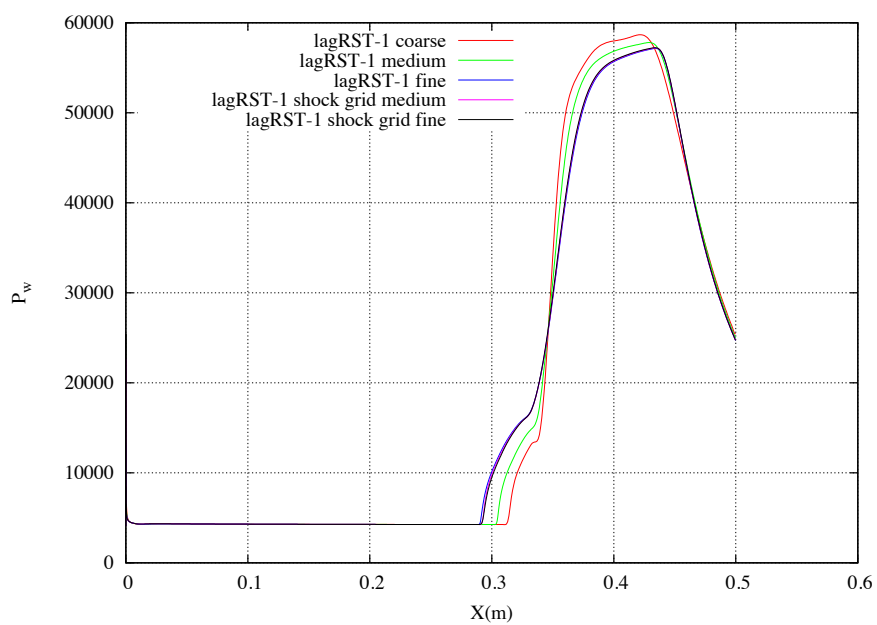
Figure 4.8. Pressure distribution for the lagRST-1 model for the coarse, medium, and fine grid along with the two "shock grids".
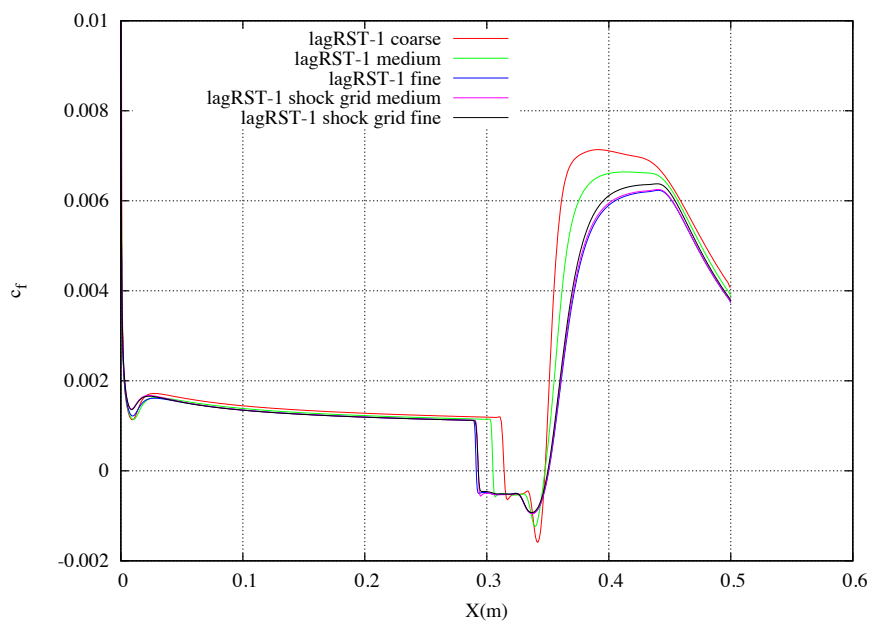
Figure 4.9. Skin friction distribution for the lagRST-1 model for the coarse, medium, and fine grid along with the two "shock grids".
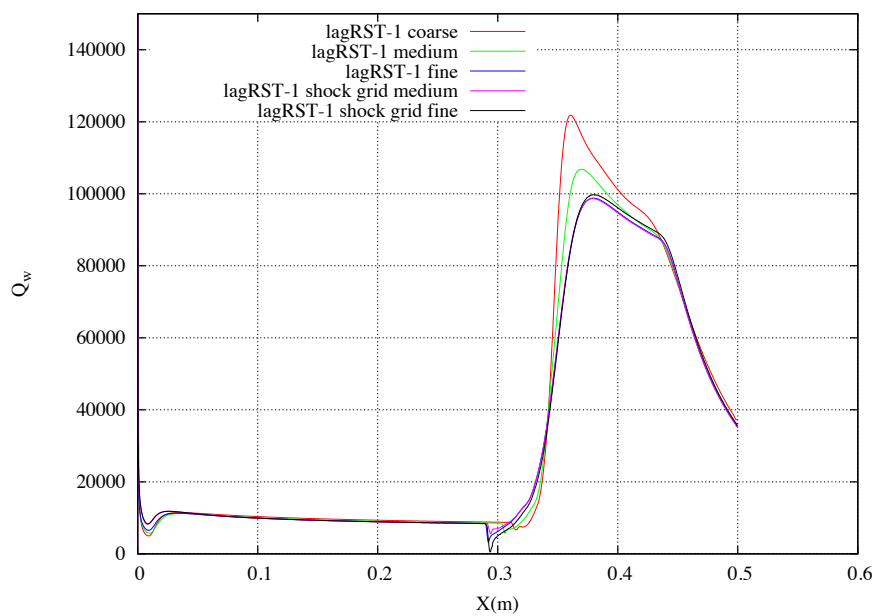
Figure 4.10. Heat flux distribution for the lagRST-1 model for the coarse, medium, and fine grid along with the two "shock grids".

4.1.4 $14°$ **SWBLI Data Comparisons**

Table 4.3 lists the separation and reattachment point along with the separation zone length for each model ran. The SST model has by far the best characterization of the separation zone length and location. The percent errors are less than 1% for all three data values. The remaining models do a very poor job prediction the separation point, with the majority of the models having percent errors of over 30%. The reattachment point is well characterized by all the models. ************** Is there physics involved here forcing it to a point?*****************. The separation zone length has the same characteristics as the separation point uncertainties. The SST provides an extremely accurate answer and the remaining models have percent errors greater than or equal to 30%.

Model	Separation Point	Reattachment	Zone length
Data	0.314m	0.348m	0.034m
SA	0.327 (39.2%)	0.349 (4.2%)	0.0221 (-35.0%)
SST	0.314 (0.6%)	0.348 (0.7%)	0.034 (0.1%)
lag	0.300 (42.5%)	0.349 (3.5%)	0.0496 (46.0%)
lagRST-1	0.296 (52.9%)	0.351 (7.7%)	0.0546 (60.7%)
lagRST-3	0.301 (39.5%)	0.348 (7.0%)	0.0498 (46.6%)
lagRSTSST	0.304 (29.1%)	0.348 (0.7%)	0.0441 (29.8%)
lagRSTSST low a_o	0.295 (56.6%)	0.35 (4.9%)	0.0549 (61.5%)

Table 4.3 Table of data indicating location and extent of the separation zone with percent error compared to the tunnel data and non-dimensionalized by the separation zone length (all data values are in meters). A negative percent error indicates the separation or reattachment point occurred too early or the separation zone length is too small.

Although the SST model nearly perfectly matched the separation zone extent, the it does underpredict the pressure plateau in the separation zone. Figure 4.12 compares the wall pressure distribution for all the models. The SA and SST models clearly miss the pressure plateau by around 30%. This is in contrast to the lagRSTSST and the lag models
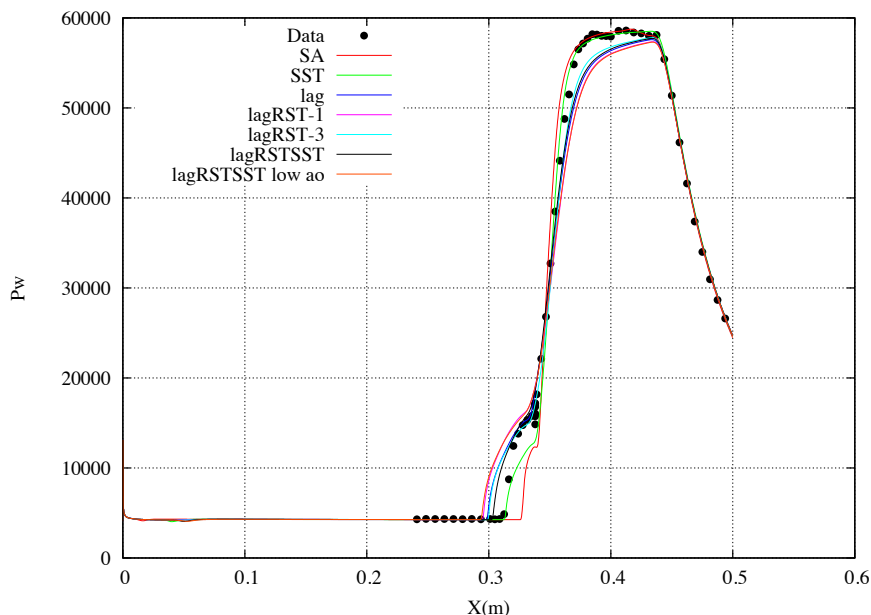
Figure 4.11. Pressure distribution comparisons for all turbulence models on the fine grid.

which match the pressure plateau very well. The lagRST-1, lagRST-3, and lagRSTSST with the low a_o overpredict the pressure plateau, but by a small percentage. The opposite behavior is true for the pressure peak behind the reflected shock. The SA and SST models predict the peak very well, whereas all the lag models underpredict the peak across the plateau region until the very end of the region. The SA and SST models predict the very flat pressure profile measured in the wind tunnel data.

Figure **??** shows the skin friction distributions for all models ran. Just as the comparisons to the undisturbed boundary layer showed (figure 4.3), the skin friction is well underpredicted by all models. It is worth noting that Brown [21] notes the same under prediction for this case. Brown uses a second method to calculate the skin friction to check the magnitudes, which brought the skin friction results down by 20% - 30%. He analyzed the log-law region of pitot probe surveys, which he claims provides an equally accurate

Figure 4.12. Skin friction distribution comparisons for all turbulence models on the fine grid.

result in areas where the flow is attached. For this particular case, he believes that there may be instabilities in the oil flow due to the high shear rates in this area, which would lead credence to the delta between the two methods. The green dots show these results, which do have excellent agreement with the SST model. In this plateau region, the SST model has the largest deviation from the other models. The lag based models all have the same shape, with the lagRSTSST having a slightly higher skin friction than the $k - \omega$ based models, or the lagRSTSST with the lag constant, a_o, set to 0.2.

Figure 4.13 shows the heat flux comparisons for all the models. All of the models over predict the heat flux by atleast 25%, if not substantially more. The SST model has the worst behavior just downstream of the reflected shock, showing an extremely large overshoot in this region. The lag based models have this overshoot, but the magnitude is much smaller. The SA model doesn't have this overshoot, but still over predicts the heat

Figure 4.13. Heat flux distribution comparisons for all turbulence models on the fine grid.

flux. One important item to notice from figure 4.13 is that the lagRSTSST model largely removes the overshoot of the SST model. In fact, towards the end of the plateau region, the two models predict the same heat flux. So although lagging the Reynolds Stress negatively affects the separation zone prediction, it makes a large improvement on the over prediction of heat flux.

4.2 Massively Separated Wake of an Orion Capsule
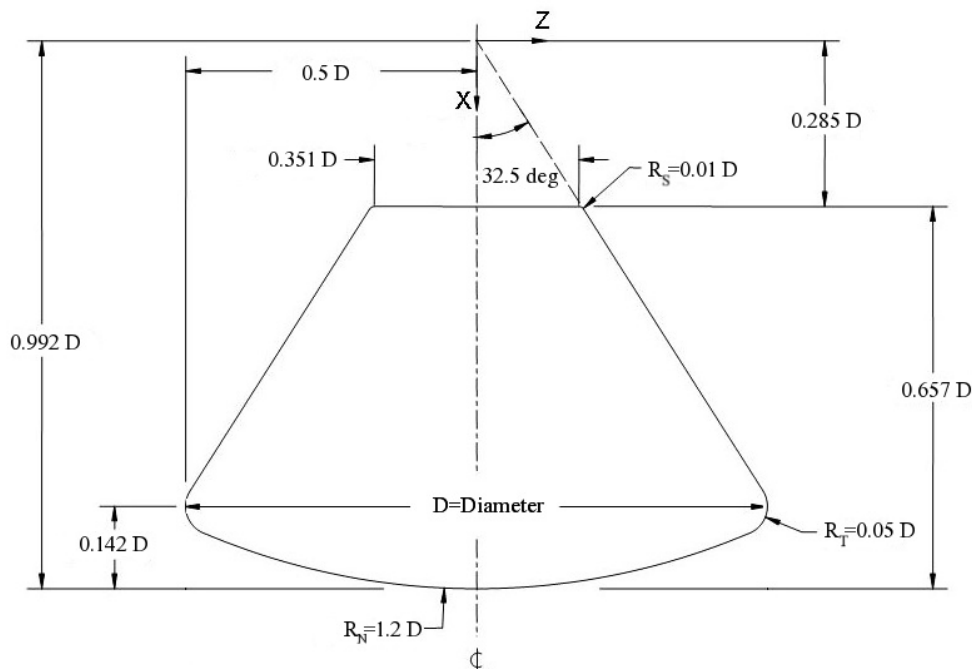
Figure 4.14. Outer Mold Line Geometry

As part of the CEV (now Orion) program, an experimental study [51, 52] of the CEV geometry (shown in figure 4.14) was conducted at the Ames Unitary Plan Wind Tunnel (UPWT) [97] in the 11-foot Transonic Test Section and the 9X7 foot Supersonic Test Section. Test data were obtained for conditions at $0.3 \leq M_\infty \leq 2.5$, $140° \leq \alpha \leq 170°$, and $1.0 \times 10^6 \leq Re_D \leq 5.3 \times 10^6$. The angle of attack is focused around the trim condition. Three models were constructed during this test, one 7.66% scale and two 3.0% scale models. The larger model included pressure taps and unsteady pressure transducers and an internal balance. One 3.0% model was designed exclusively for force and moment data (internal balance), and the other was designed solely for taking pressure data. Boundary layer trips were applied to the model using CadCut trip dot tape. This study will compare to the $Re_D = 5.3 \times 10^6$ case at $M\infty = 0.95$. This condition was investigated only with the larger model in the 11-foot Transonic Test Section. The 3% models provided Reynolds
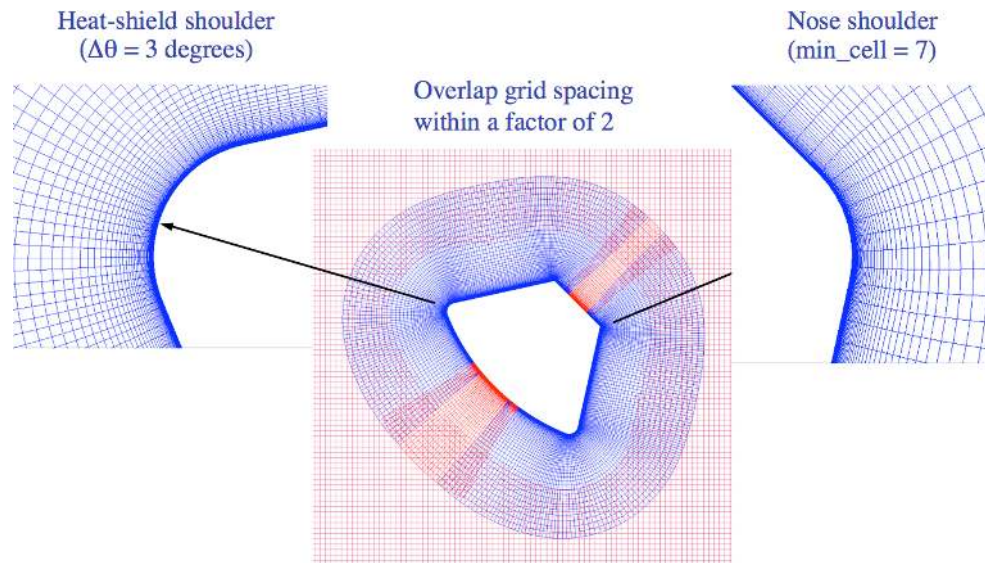
Figure 4.15. Near Body Grid System

number comparison, and allowed comparison between test run in two different facilities, which helped quantify uncertainty. Three different angles of attack were assessed, $142.4°$, $154.4°$, and $170.4°$.

Through unpublished results and internal reports, the Orion Aerosciences team has shown that the choice of turbulence model makes a large difference on the wake behavior, which directly affects the C_D of the capsule. Therefore, this study will focus on comparisons with C_D and C_L. In addition, pitch plane contour images will be used to show the wake size and its state. Internal reports also show that the sting and wall interference effects, as currently modeled, are a secondary effect in relation to the turbulence model choice, so they will be ignored here. Including these details would also drives the grid requirements up significantly.

4.2.1 Grid System

The grid system used was the same grid system employed by Olsen et al. [8]. This is a three zone grid system, shown in figure 4.15. The near body grid system is made up of

an axi-symmetric grid (in y-z) that is rotated around the x-axis and two H-grids that are overset on the axis points to remove the singularities from the grid-system. The standard overset grid methodology within overflow [98] was used to generate the near body grids. Initial wall normal spacing for the medium grid was $4 \times 10^{-6}D$, which gave an initial Δy^+ of less than 1.5 at every point. The near field grid system extended out approximately $\frac{1}{2}$D from the capsule. The near body grids were then enclosed using with cartesian box grids using the off-body grid generation capability internal to OVERFLOW [99, 100]. The wake box grid the enclosed the near body grids extended upstream of the capsule a little less than two capsule diameters and downstream over 5 capsule diameters. The automatic techniques generated 30, 36, and 45 box grids for the coarse, medium and fine grids, respectively. An image of the medium grid system is shown in figure 4.16. The domain extended approximately 16 capsule diameters in each direction.

Grid System	Capsule Grids	Box Grids	Total
coarse	230,352	1,014,386	1,244,738
medium	1,788,565	4,636,564	6,425,129
fine	13,402,440	3,232,258	45,725,698

Table 4.4 Number of grid points for the Orion grid system.

4.2.2   Solution Procedure

Simulations were done using multigrid and grid sequencing, and completed with a time accurate simulation using dual time integration, to assess the steadiness of the flowfields. The time histories of the integrated forces were used to assess whether the flowfields were steady or unsteady as well as when the solutions were checked to be sure that they were adequately time resolved. Previous work by Olsen et al. [8] showed that in general, supersonic cases tended to be steady, and subsonic cases unsteady. This statement came from comparisons for a set of supersonic cases ($M_\infty = 1.4$) and a set of subsonic cases
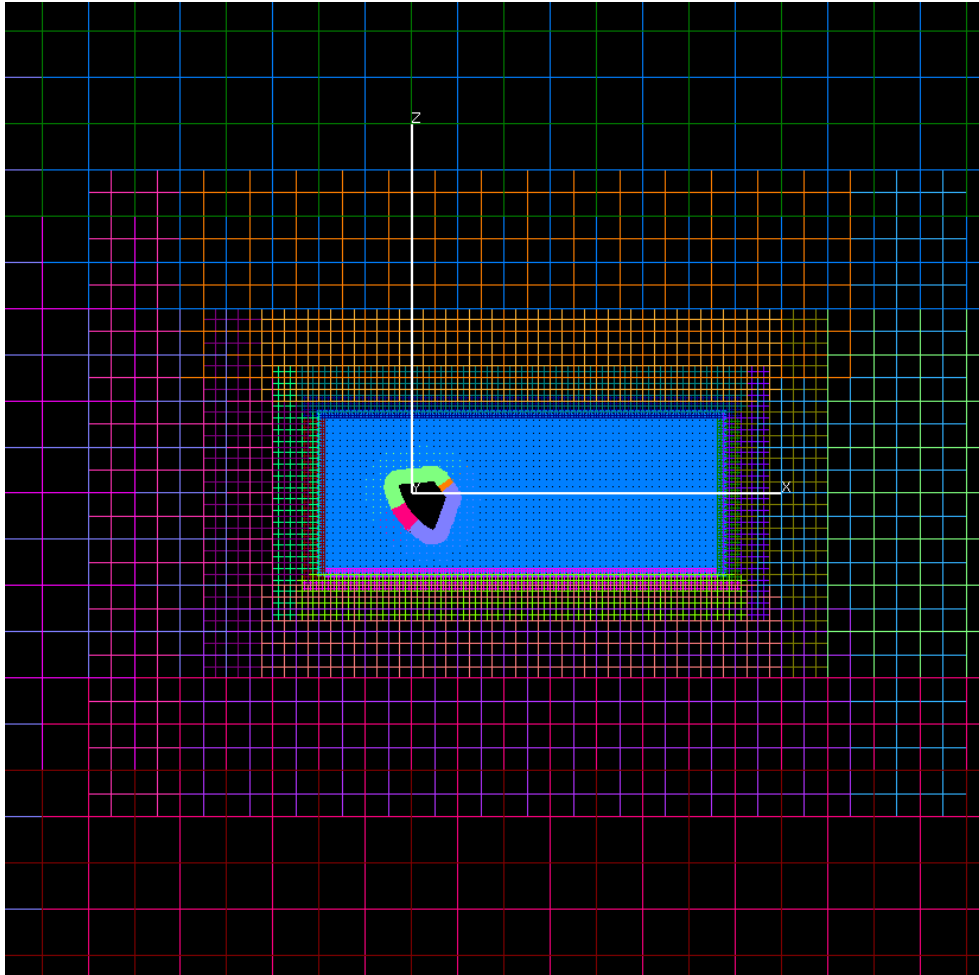
Figure 4.16. Cartesian box grids enclosing the Orion near body grid system.

($M_\infty = 0.95$). Since this study will concentrate on the $M_\infty = 0.95$ cases, all cases will be simulated assuming unsteady flow conditions.

4.2.3 Grid Convergence

Due to the significant amount of computer time taken to run the cases, grid convergence was not assessed for every turbulence model. Grid convergence was assessed for the lagRST-1 model at all three chosen angles of attack and the lagRSTSST model was assessed at $154.4°$ and $170.4°$.

Table 4.5 C_L and C_D for the $\alpha = 170.4°$ set of cases.

Model	Alpha	grid	C_D	C_L
lagRST-1	170.4°	coarse	1.10	0.18
lagRST-1	170.4°	medium	1.08	0.17
lagRST-1	170.4°	fine	1.09	0.18
lagRSTSST	170.4°	coarse	1.22	0.20
lagRSTSST	170.4°	medium	1.19	0.19
lagRSTSST	170.4°	fine	1.19	0.20

Table 4.5 shows the C_L and C_D for $\alpha = 170.4°$. The results show for both the lagRST-1 and the lagRSTSST that grid convergence is obtained with the medium grid. Even the coarse grid results are nearly identical to the medium grid. It is expected that this is due to both models producing steady solutions for this case. The experimental results did have unsteady characteristics in the wake, but none of the computations showed this. This will be discussed in upcoming sections. The extend of the wake grid was also assessed by increasing its downstream distance by 20%. This had less than a 1% change on C_D or C_L and did not affect the unsteadiness of the wake.

Table 4.6 C_L and C_D for the $\alpha = 154.4°$ set of cases.

Model	Alpha	grid	C_D	C_L
lagRST-1	154.4°	coarse	1.09	0.49
lagRST-1	154.4°	medium	1.06	0.46
lagRST-1	154.4°	fine	1.04	0.46
lagRSTSST	154.4°	coarse	1.06	0.49
lagRSTSST	154.4°	medium	1.03	0.46
lagRSTSST	154.4°	fine	1.01	0.45

Table 4.6 shows the C_L and C_D for $\alpha = 154.4°$. Again, the medium and fine grid results are nearly identical, but for this case, the coarse grid results have more variation. The lagRST-1 model did produce an unsteady result, whereas the lagRSTSST model produced a steady result. The medium grid again provides a grid converged result.

Table 4.7 C_L and C_D for the $\alpha = 142.4°$ set of cases.

Model	Alpha	grid	C_D	C_L
lagRST-1	142.4°	coarse	1.02	0.65
lagRST-1	142.4°	medium	0.87	0.59
lagRST-1	142.4°	fine	0.88	0.60

Table 4.7 shows the C_L and C_D for $\alpha = 142.4°$. Due to computing constraints, the lagRST-1 model was the only one used for this α. The coarse grid results for this case are very different than the medium and fine. However, again the medium and fine grid provide very similar results. This will be discussed more in upcoming sections, but the large deviation from the coarse grid is most likely due to the solution becoming more unsteady as the α gets smaller. The numerical oscillations were larger at this condition, and the experimental results showed more unsteadiness.

Based on this set of comparisons, the medium grid provides a grid converged solution and will be used for comparisons to the experimental data.

4.2.4 Flowfield Characteristics

Results were obtained on the medium grid at the three previously discussed α conditions for a suite of turbulence models, ranging from baseline models to the lagRST based models. The standard OVERFLOW versions of Spalart Allmaras and SST were ran along with the standard lag model. In addition, the lagRST-1, lagRST-2, and lagRST-3 were ran along with the lagRSTSST with the normal lag constant (a_o) and a lower value of the lag constant, $a_o = 0.2$. All results were averaged over a time interval containing a minimum of

two oscillations. If an oscillation was not identified (either because the result was steady or the oscillation was not periodic), the time averaging interval was 3000 iterations. With the chosen time advancement parameters, a typical oscillation of the wake took at most 350 iterations.
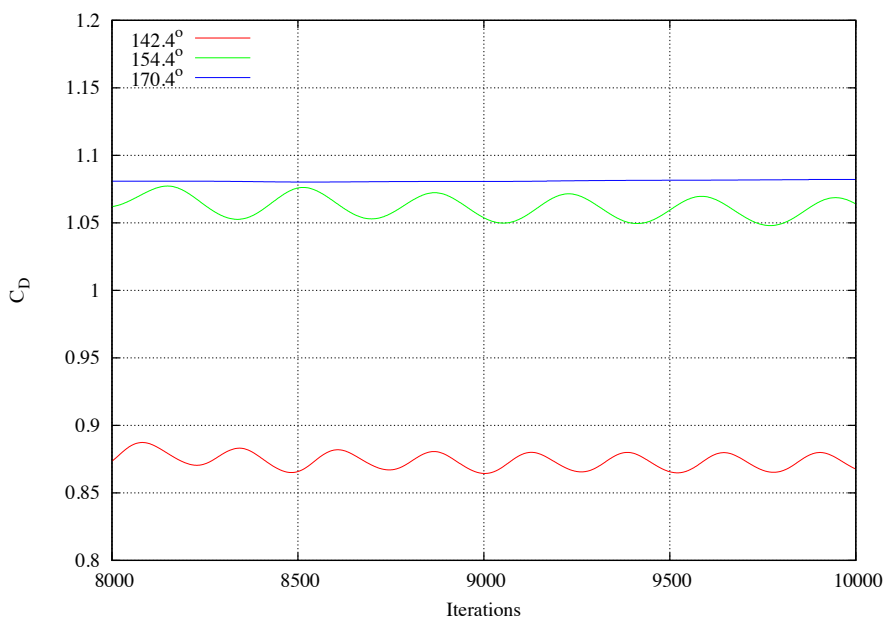
Figure 4.17. Time history of C_D (plotted vs iteration) for the lagRST-1 model at all α's.

********FIX THIS DISCUSSION************ Figure 4.17 shows a typical time history of C_D for the lagRST-1 model at each α (the lagRST-3 model had similar behavior). The oscillation is periodic, indicating a consistent shedding behavior in the wake. The frequency of the oscillation increases going from $\alpha = 142.4°$ to $\alpha = 154.4°$. The amplitude of the oscillation goes to zero as the α approaches $170.4°$. Once at the highest α, the oscillation damps out and the C_D results become steady. Only a subset of the models had an oscillating C_D at the lower α's, but every model produced a non-oscillating C_D profile at $\alpha = 170.4°$. Figure 4.18 shows all Mach contours for all three alpha conditions. In

(a) 142.4°   (b) 154.4°   (c) 170.4°

(d) Mach Contour Legend   (e) Mach Contour Legend   (f) Mach Contour Legend
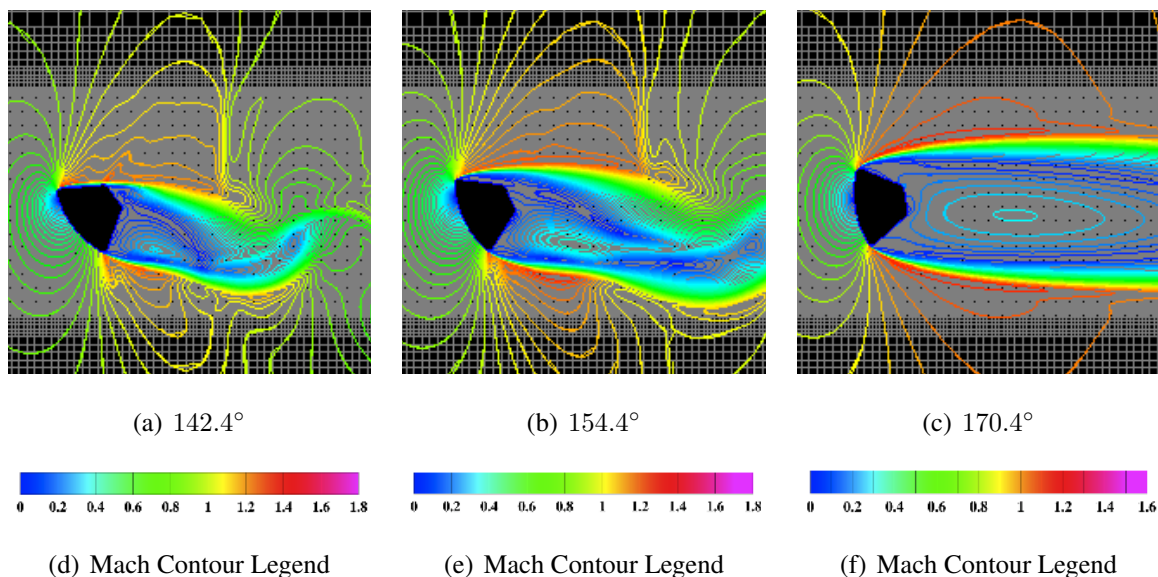
Figure 4.18. Mach contours in the pitch plane for the lagRST-1 model showing the wake at all three α's.

general, an oscillating C_D profile correlates to a wake that is shedding. This can be seen by comparing figures 4.18(a) and 4.18(b) with figure 4.18(c). At $\alpha = 170.4°$, the C_D time history is steady, and the wake is symmetric and has no shedding. At the two lower α's, the Mach contours show an asymmetric wake that is shedding, which correlates to previously seen oscillating C_D time history. This behavior will generally be the case for all solutions. If the wake is shedding, the C_D time history will be oscillating. There is however, one exception to this. Figure 4.19 compares the lag model with the lagRST-1 model at $\alpha = 142.4°$. The lag model has a steady C_D time history (variation in C_D of less than 0.5%), but figure 4.19(a) clearly shows the wake is oscillating. If you compare figure 4.19(a) with figure 4.19(b), it is apparent that the re-circulation zone in the wake of the capsule is closing for the lag model before the shedding is occurring. In contrast, the lagRST-1 simulation does not predict the re-circulation zone to close before the shedding begins. It stands to reason that if the re-circulation zone is closed, then the C_D time history will be steady even if the wake oscillates downstream of the zone closure.

(a) lag

(b) lagRST-1

(c) Mach Contour Legend
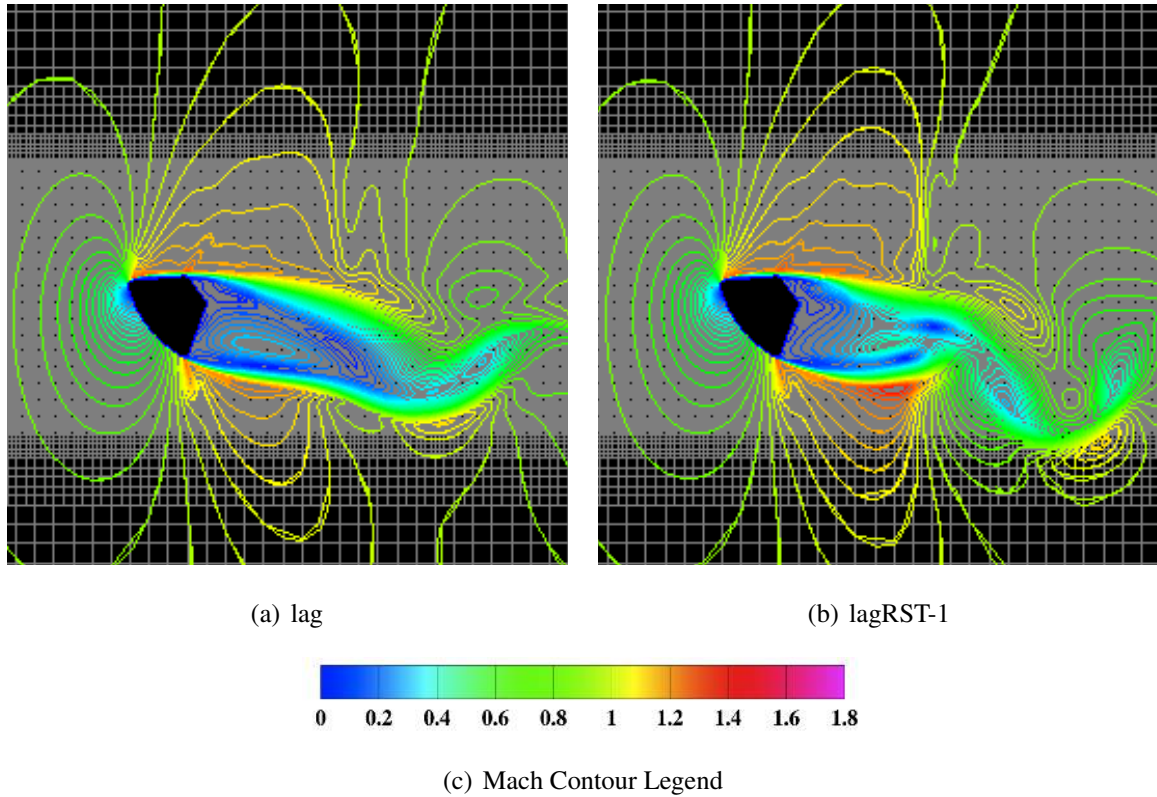
Figure 4.19. Mach contours in the pitch plane for the lag and lagRST-1 models showing the wake at $\alpha = 142.4°$.

In contract to the lagRST-1 model, the lagRST-2 model shows an unsteady but non-periodic behavior in C_D. Figure 4.20 shows the C_D time history over 2000 iterations. The solutions are not periodic and are not oscillating about a mean value. Although the results will not be shown here, a more detailed study of this model and its convergence behavior was done. It was found that the model does not produce the expected periodic behavior and the model has difficulty converging to a mean value. This behavior is most likely caused by the lower value of a_o used in the lagRST-2 model ($a_o = 0.2$). For the lagRST implementation, this choice of coefficient causes convergence issues and will not be recommended for future use.
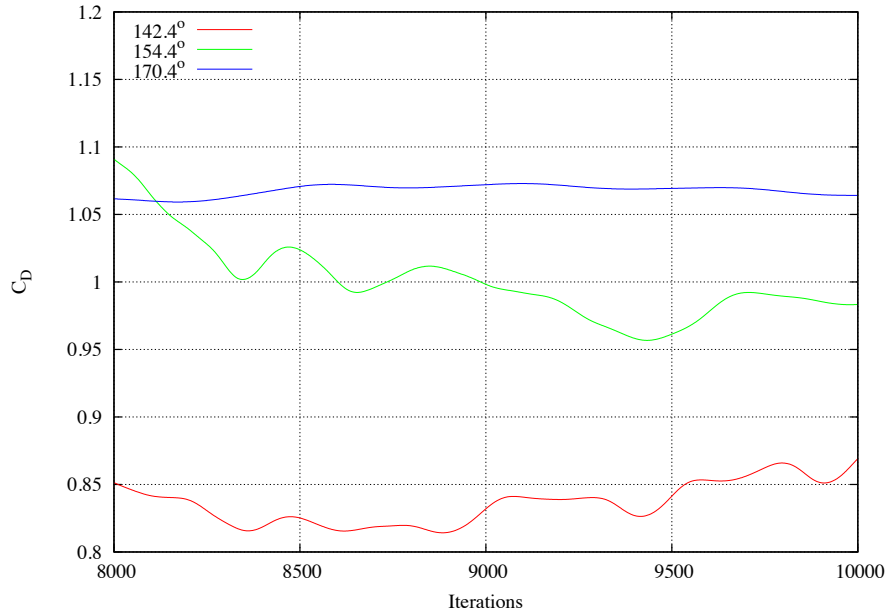
Figure 4.20. Time history of C_D (plotted vs iteration) for the lagRST-2 model at all α's.

4.2.5   Comparison with Experiment

Table 4.8 shows the C_L and C_D results for all turbulence models ran on the medium grid and the percent difference from the wind tunnel results.

The Spallart Allmaras and SST models by far have the highest percent error at the lower α's. Figure 4.21 compares Mach contours for the the Spallart Allmaras and SST results at $\alpha = 142.4°$ to the lag model, which has the lowest percent error. The Spalart Allmaras model has a noticeably thicker wake. This larger wake increases the disturbance to the flowfield, and thus increases the C_D (indicated by a very large negative percent error). The Spallart Allmaras and SST models also both have stronger shocks than the lag model. This also accounts for higher drag by reducing P_t. For the SA and SST models, the precent error reduces as the angle of attach increases. However, for the SA model, even at $\alpha = 170.4°$ where the wake is more well behaved the predictions are still off by approximately 20%.

(a) Spalart Allmaras

(b) SST

(c) lag

(d) Mach Contour Legend
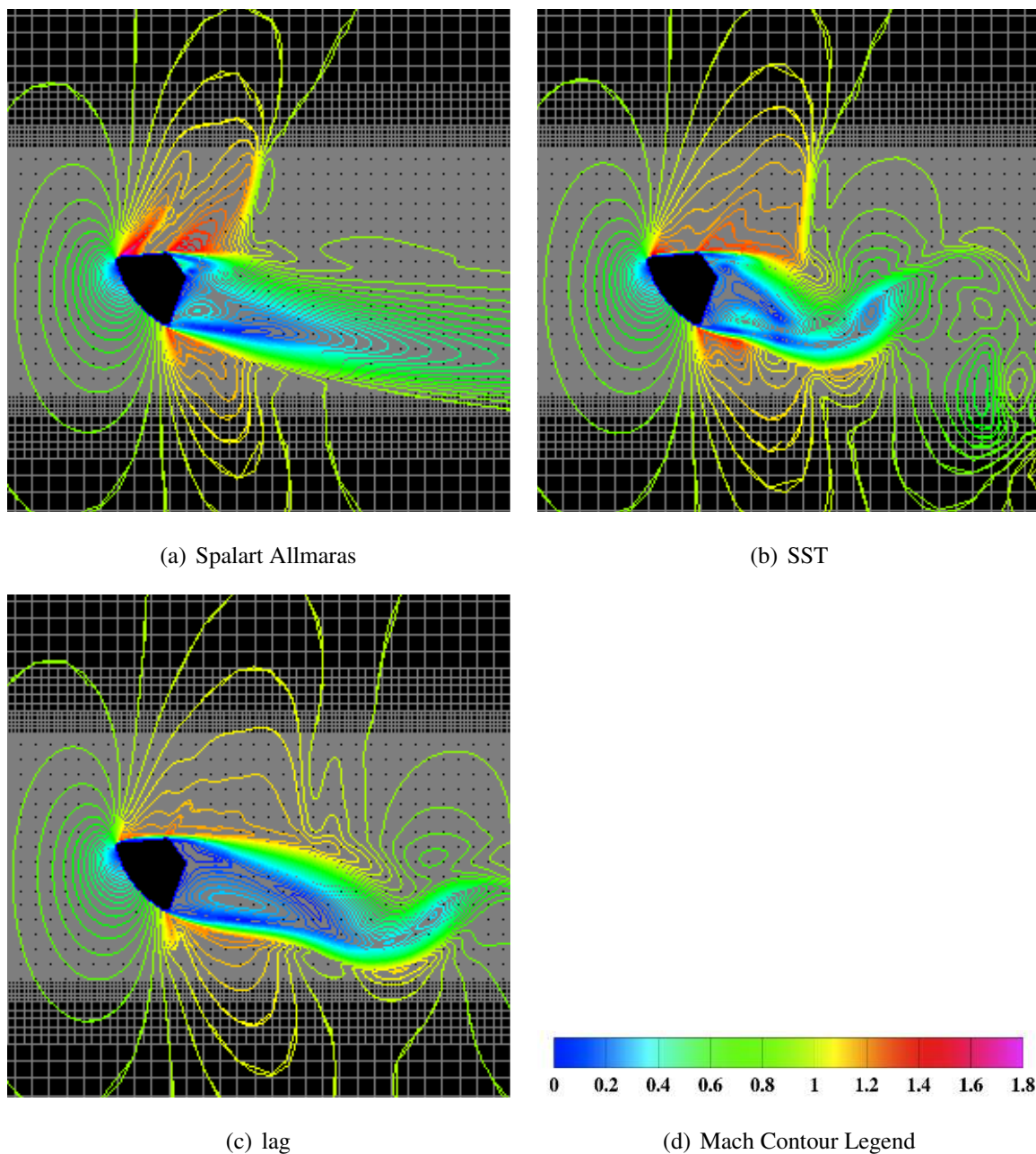
Figure 4.21. Mach contours in the pitch plane for the Spalart Allmaras and SST models showing the wake at $\alpha = 142.4°$.

The baseline SST model provides better results than the Spalart model at all α's, but still has a percent error between 12 and 16 percent for the two low α cases. The prediction for $\alpha = 170.4°$ is excellent, with percent error around 5%.

The lag model provides the best results, if looked at over all three α's. The C_D results are nearly identical at the lower α's, and and the C_L results have some of the lowest percent errors at the same conditions. At $\alpha = 170.4°$, the percent errors raise significantly over the lower α numbers, but still provides a prediction less than 10%.

For the lagRST-1 and lagRST-3 models, the percent errors are of the same order for all α's. This is a definite improvement over the SST model for the lower α cases, but for the $\alpha = 170.4°$ case the errors are larger than the SST model. It is also worth noting that the simulations predict a C_D and C_L above the experimental results for the lower α cases but predict a value below the experimental results for the highest α.

The lagRSTSST has the best prediction of any model at $\alpha = 170.4°$, and the percent errors at the two lower α's are as good or better than any of the other models, excluding the lag model. Even though the results are very close, the predictions have a non-oscillating wake. Even though this is the case, the lagRSTSST model is a huge improvement over the baseline SST, especially at the lower α's, because the percent error for C_D reduces by almost 10% and the $\alpha = 170.4°$, although it has a small percent error to begin with, drops it by around a factor or two over the baseline SST model. Figure 4.22 shows four different versions of SST based models. As previously discussed, the baseline SST provided an unsteady wake whereas the lagRSTSST did not (this is compared in figure 4.22(a) with figure 4.22(c)). At first glance, this behavior is inconsistent with the premise of the lag models. However, there is a valid explanation. The baseline SST model used in these results is the implemented version in OVERFLOW 2.2c, however the SST model used to define the equilibrium conditions for the lagRSTSST model was taken from OVERFLOW 2.0aa. Figure 4.22(b) shows an SST result with the OVERFLOW 2.0aa implementation, but with the new version of the code. This explains the previous inconsistency. The newer implementation of the SST model produces an unsteady answer. Unfortunately, to date, no reference for the exact formulation within the 2.2c version of the code has been obtained, but it is apparent to the author that there are several differences between 2.0aa and 2.2c. These differences are in the form of limiters in the 2.2c version of the code that affect the value of omega in the source calculations, production of k, and the cross diffusion.

NOTE Mike is working on a list of differences, I can put these in the appendix if necessary**

Because the lagRSTSST results were steady, a second set of cases using a lower value of a_o value ($a_o = 0.2$) were ran. With the lower value of a_o, it was postulated that the results could become unsteady and thus more representative of the wind tunnel test. The results for this test case are labeled "lagRSTSST low a_o" in table 4.8. The C_L and C_D results are nearly identical to the lagRSTSST model, however the force and moment data does possess a periodic oscillation. Figure 4.22 shows the Mach contours comparing the lagRSTSST model with the nominal and lower value of a_o. Although the C_D and C_L results are very similar, the wake contours are not. Figure 4.22(d) shows that by reducing the value of a_o, the wake near the point where re-circulation would close becomes unsteady and sheds. This is further downstream than the what the baseline SST model shows and is slightly upstream from what the lag model predicts.

(a) SST OVERFLOW V2.2

(b) SST OVERFLOW V2.0

(c) lagRSTSST

(d) lagRSTSST low a_o

(e) Mach Contour Legend
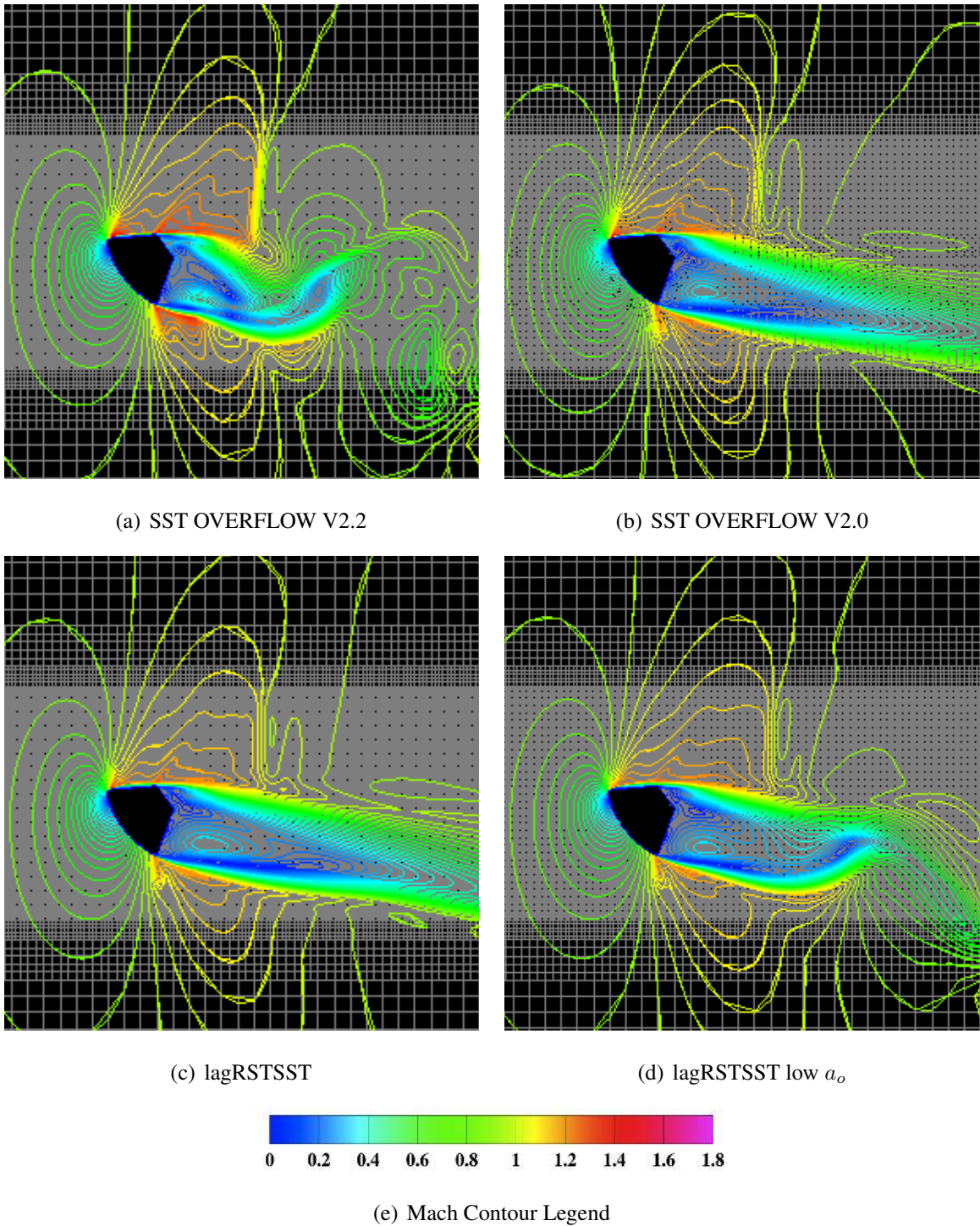
Figure 4.22. Mach contours in the pitch plane for the lagRSTSST model with the nominal and lower values of a_o showing the wake at $\alpha = 142.4°$.

Table 4.8 C_L and C_D results and percent errors for all turbulence models on the medium grid (percentages over 10% noted in red.

Model	Alpha	C_D	C_L	$C_D\%$ error	$C_L\%$ error
SA	142.4	1.04	0.71	-25.8	-31.5
SA	154.4	1.23	0.58	-23.8	-39.2
SA	170.4	1.39	0.23	-19.4	-18.2
SST V2.2	142.4	0.95	0.63	-15.2	-16.2
SST V2.2	154.4	1.12	0.49	-12.6	-16.1
SST V2.2	170.4	1.11	0.18	4.1	5.5
lag	142.4	0.83	0.58	-0.9	-7.1
lag	154.4	0.98	0.44	0.7	-4.4
lag	170.4	1.09	0.17	6.3	10.0
lagRST-1	142.4	0.87	0.59	-5.7	-9.0
lagRST-1	154.4	1.06	0.46	-6.7	-10.2
lagRST-1	170.4	1.08	0.17	6.7	12.1
lagRST-3	142.4	0.87	0.59	-5.2	-7.8
lagRST-3	154.4	1.06	0.46	-6.9	-8.7
lagRST-3	170.4	1.09	0.17	6.2	12.2
lagRSTSST	142.4	0.85	0.59	-3.1	-8.6
lagRSTSST	154.4	1.03	0.46	-4.4	-10.1
lagRSTSST	170.4	1.19	0.19	-2.3	0.9
lagRSTSST low a_o	142.4	0.83	0.57	-4.5	-7.4
lagRSTSST low a_o	154.4	1.01	0.44	-2.3	-6.0
lagRSTSST low a_o	170.4	1.16	0.19	-0.3	4.1
SST V2.0	142.4	0.88	0.62	-7.1	-13.8
SST V2.0	154.4	1.07	0.49	-8.3	-17.3
SST V2.0	170.4	1.22	0.20	-5.6	-4.8

Table 4.9 shows the computed Strouhal numbers for the cases that had oscillating wakes. None of the predictions had oscillations at $170.4°$. The lagRST-1, lagRST-3, and SST models all had a repeatable oscillation pattern in the wake for alpha's of $142.4°$ and $154.4°$. The lagRSTSST model did not have an oscillating wake when using an a_o value of 0.35, but when it was reduced to 0.2, the solution oscillated around a mean value. There was no oscillation at $\alpha = 154.4°$ for this model. In general, the results provided by the models are very consistent between models. At the lowest α, the lagRST-1, lagRST-3, and SST models all have about the same prediction. This is not true for the lagRSTSST (using low a_o). Its prediction is right on the data at the low α. However at the two higher α's, there is no oscillation.

α	Data	lagRST-1	lagRST-3	SST	lagRSTSST	lag
$142.4°$	0.22	0.27 (1.7%)	0.25 (1.4%)	0.26 (2.5%)	0.22 (0.01%)	0.27 (0.64%)
$154.4°$	0.17	0.18 (1.8%)	0.18 (1.9%)	0.19 (2.1%)	n/a	0.24 (0.24%)
$170.4°$	0.15	n/a	n/a	n/a	n/a	n/a

Table 4.9 Computed Strouhal number for the lagRST-1, lagRST-3, SST, and lagRSTSST models. The numbers in parenthesis after the Strouhal number is a measure of the oscillation. It is the percent the amplitude of the oscillation is of the total C_D.

Figures 4.23 through 4.46 show a suite of Mach number and turbulent kinetic energy contours in the pitch plane for the lagRST and the lagRSTSST model for all three α's. The figures are organized at first by alpha and then by turbulence model choice. For each simulation (choice of alpha and turbulence model) there are four figures. The first figure is a zoomed out view of Mach number, while the second figure zooms in within a couple of diameters of the capsule. The third and fourth figure have the same set of views but the Mach number is replaced with turbulent kinetic energy. There are essentially two types of cases represented. The first are the lagRST set at $\alpha = 142.4°$ and $\alpha = 154.4°$ where the wake is oscillating and the C_D is oscillating. This type of case would typically represent the lagRST-1, lagRST-3, and SST set of cases at the two lower α conditions. The set of four

figure was chosen to show roughly one cycle of this oscillation. Note that all three of these turbulence models also have the same wake and C_D behavior at $\alpha = 170.4°$. This behavior is the same as the second set of plots. These plots cover all three α's for the lagRSTSST model. These cases have both a steady wake and C_D time history. The images correlate to the one oscillation of the wake for the lagRST-1 model, but it is clear that there is no oscillation for the lagRSTSST model.

****Add this***** TKE physics, litle puddles of red. Peak TKE is in shear layers, and then gets convected into the wake. Producing TKE at the edge and getting pulled back in. THis is physically what shoudl be occurring, and the models are predicting the physics right here.

(a)

(b)

(c)

(d)

(e) Mach Contour Legend

Figure 4.23. Mach contours in the pitch plane for the lagRST model showing the wake at $\alpha = 142.4°$.

(a)

(b)

(c)

(d)

(e) Mach Contour Legend
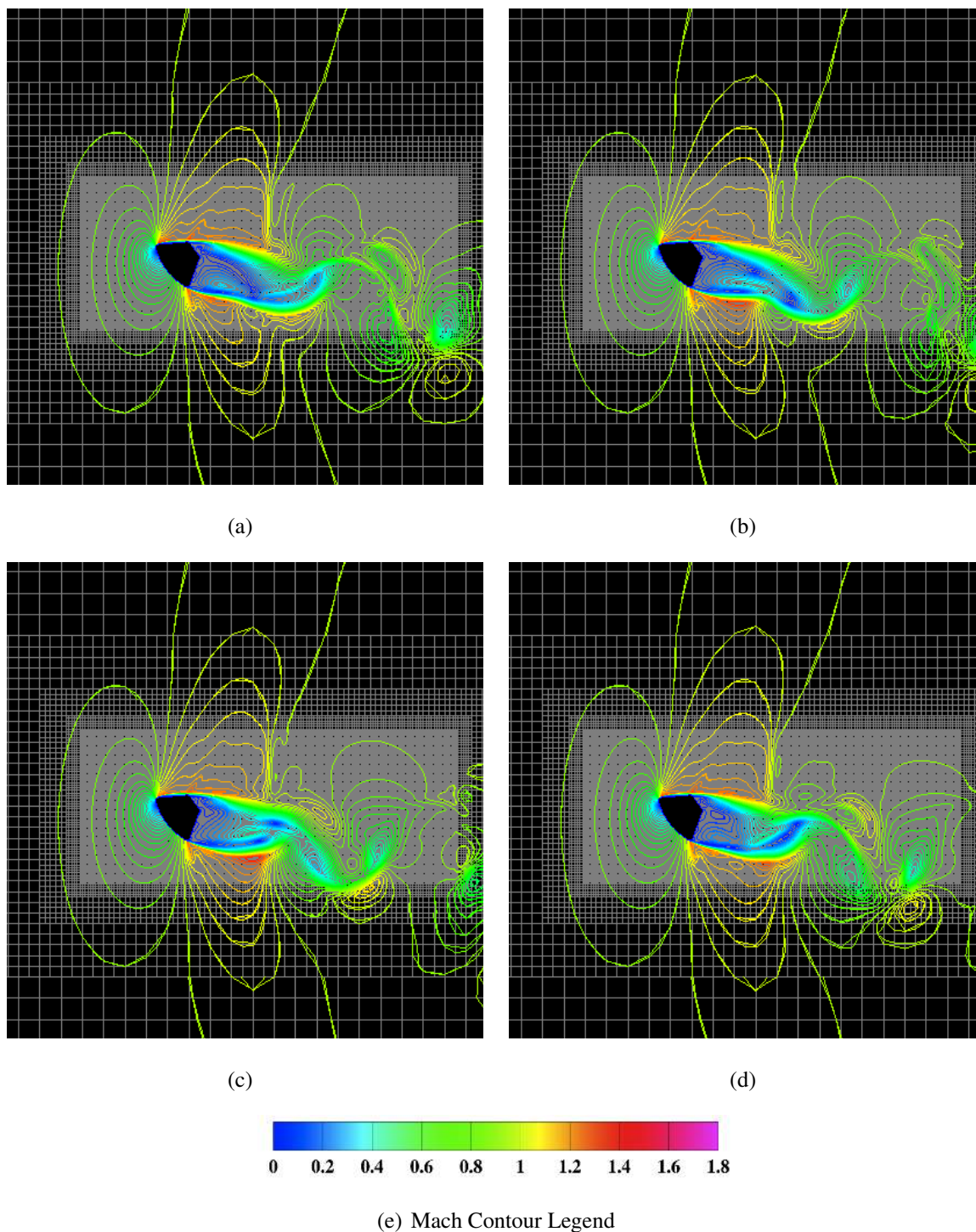
Figure 4.24. Zoomed in Mach contours in the pitch plane for the lagRST model showing the wake at $\alpha = 142.4°$.

157

(a)

(b)

(c)

(d)

| 0 | 0.01 | 0.02 | 0.03 | 0.04 | 0.05 | 0.06 | 0.07 | 0.08 |
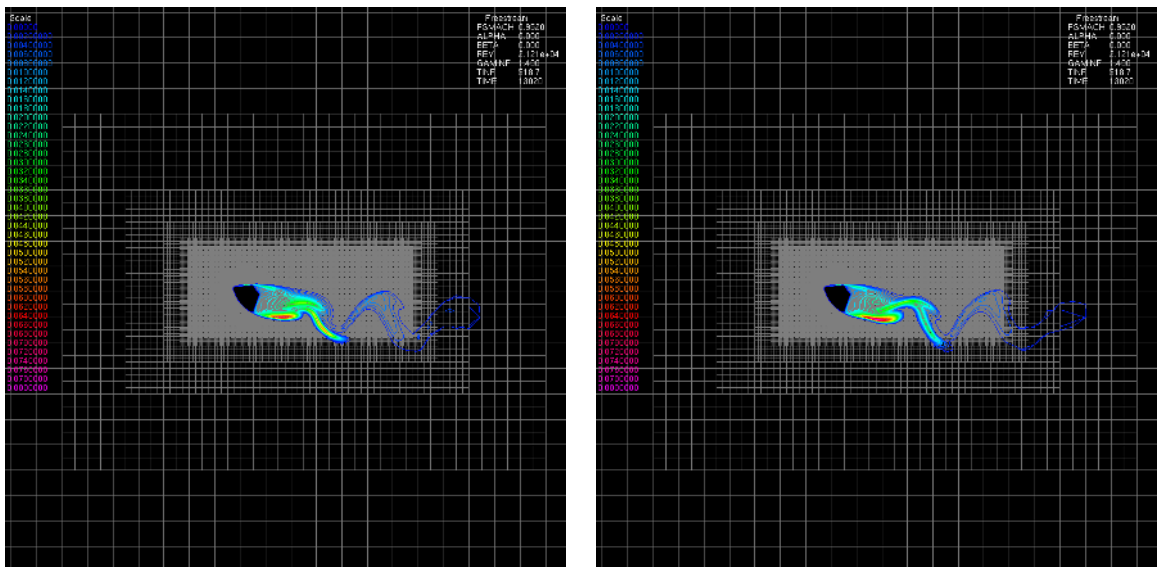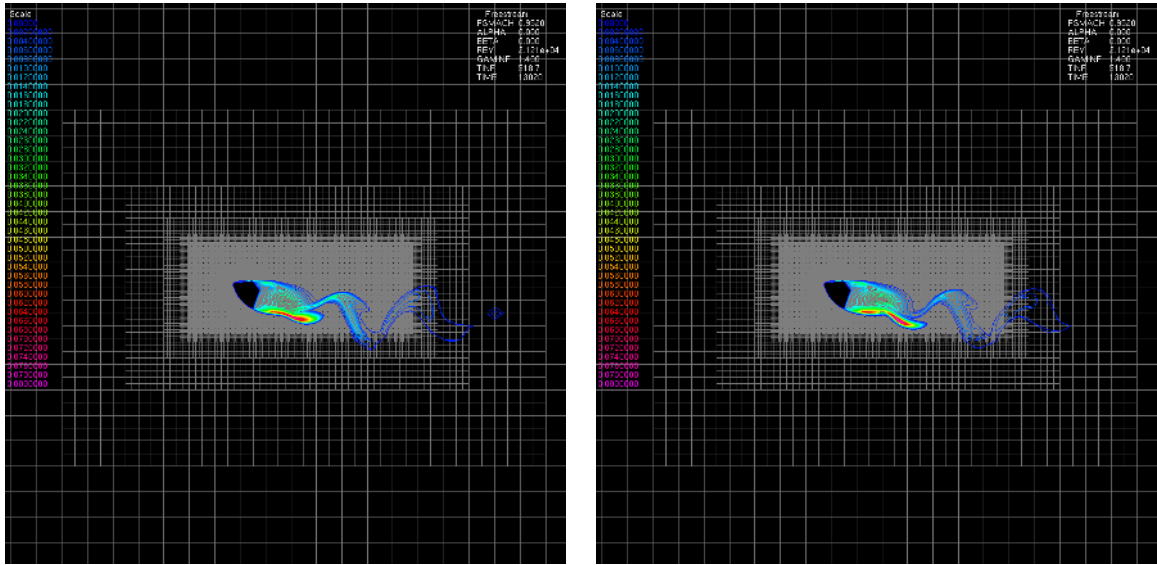
(e) TKE Contour Legend

Figure 4.25. TKE contours in the pitch plane for the lagRST model show-
ing the wake at $\alpha = 142.4°$.

(a)

(b)

(c)

(d)

(e) TKE Contour Legend

Figure 4.26. Zoomed in TKE contours in the pitch plane for the lagRST model showing the wake at $\alpha = 142.4°$.

(a)

(b)

(c)

(d)

(e) Mach Contour Legend
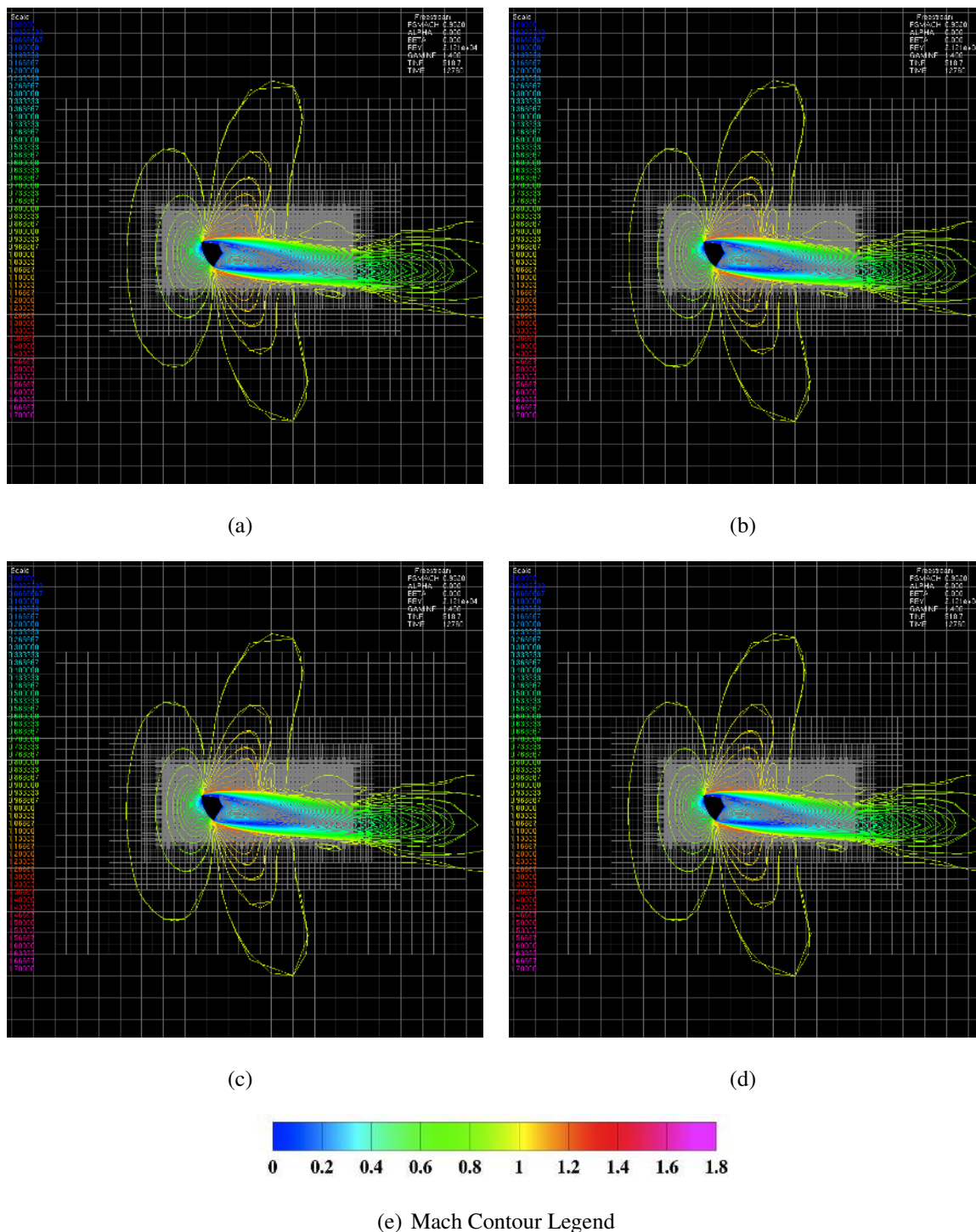
Figure 4.27. Mach contours in the pitch plane for the lagRSTSST model showing the wake at $\alpha = 154.4°$.

(a)

(b)

(c)

(d)

(e) Mach Contour Legend
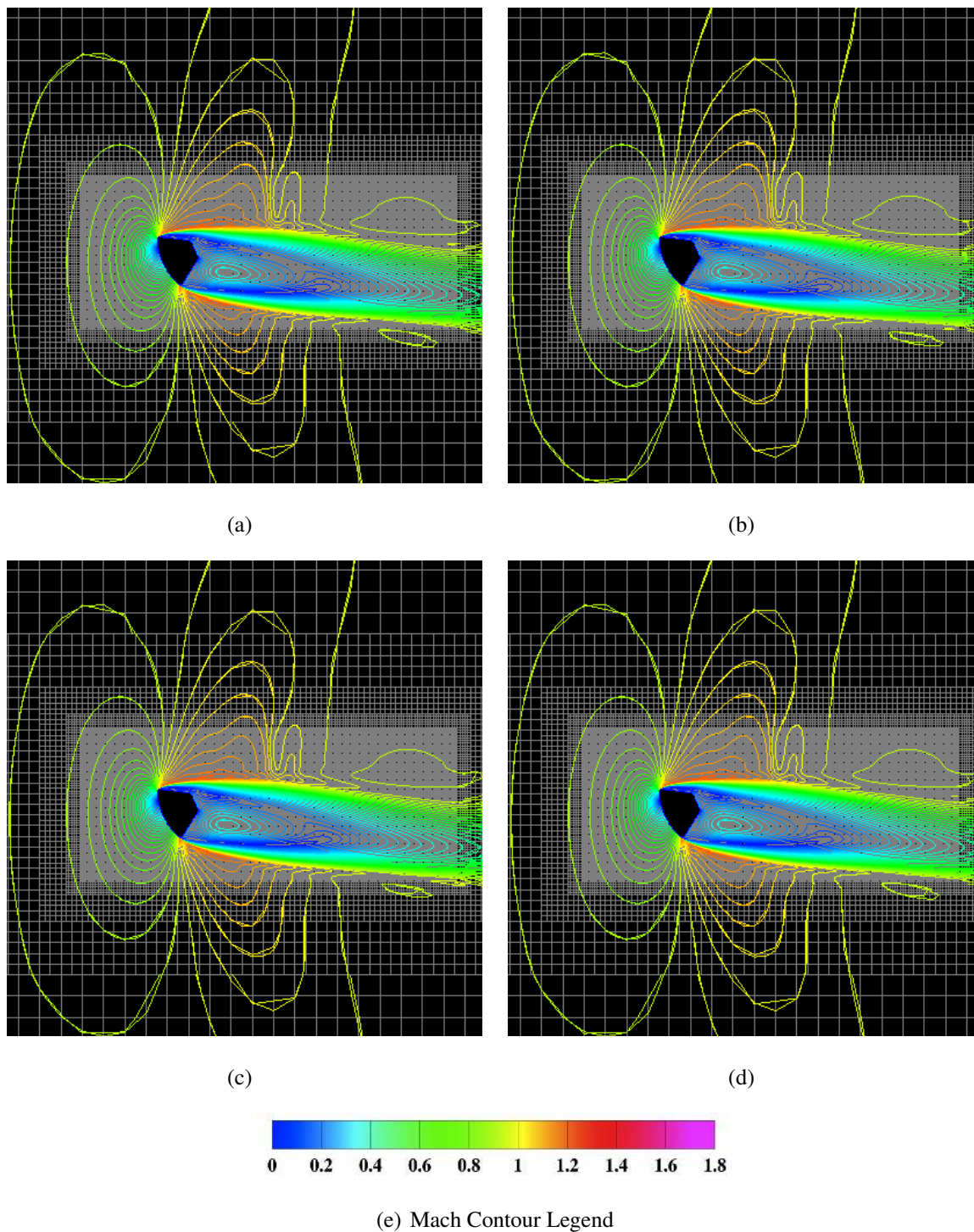
Figure 4.28. Zoomed in Mach contours in the pitch plane for the la-gRSTSST model showing the wake at $\alpha = 154.4°$.

(a)

(b)

(c)

(d)

(e) TKE Contour Legend

Figure 4.29. TKE contours in the pitch plane for the lagRSTSST model showing the wake at $\alpha = 154.4°$.

(a)

(b)

(c)

(d)

(e) TKE Contour Legend

Figure 4.30. Zoomed in TKE contours in the pitch plane for the la-gRSTSST model showing the wake at $\alpha = 154.4°$.

(a)

(b)

(c)

(d)

(e) Mach Contour Legend
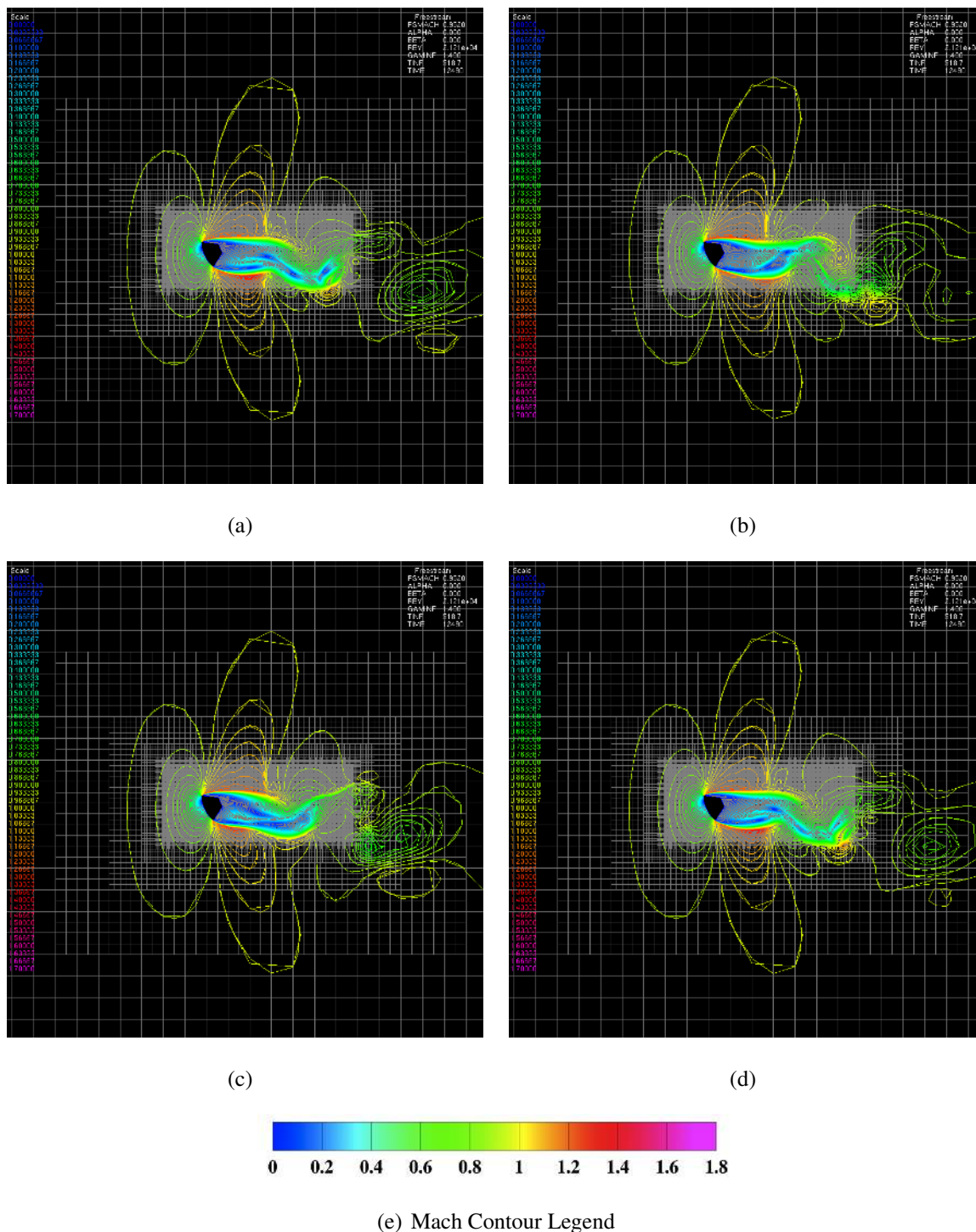
Figure 4.31. Mach contours in the pitch plane for the lagRST model showing the wake at $\alpha = 154.4°$.

(a)

(b)

(c)

(d)

(e) Mach Contour Legend
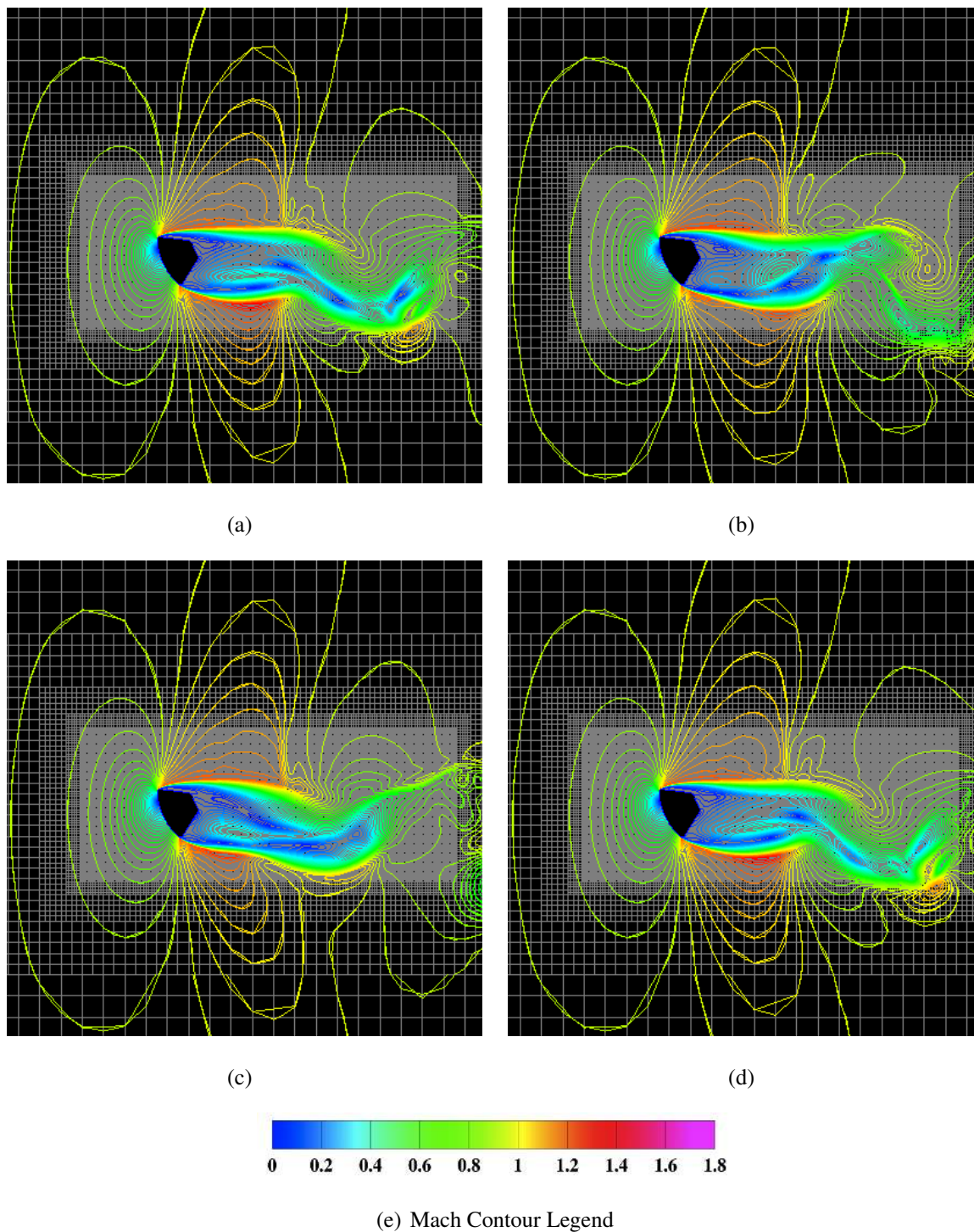
Figure 4.32. Zoomed in Mach contours in the pitch plane for the lagRST model showing the wake at $\alpha = 154.4°$.

(a)

(b)

(c)

(d)

(e) TKE Contour Legend

Figure 4.33. TKE contours in the pitch plane for the lagRST model showing the wake at $\alpha = 154.4°$.

(a)

(b)

(c)

(d)

(e) TKE Contour Legend
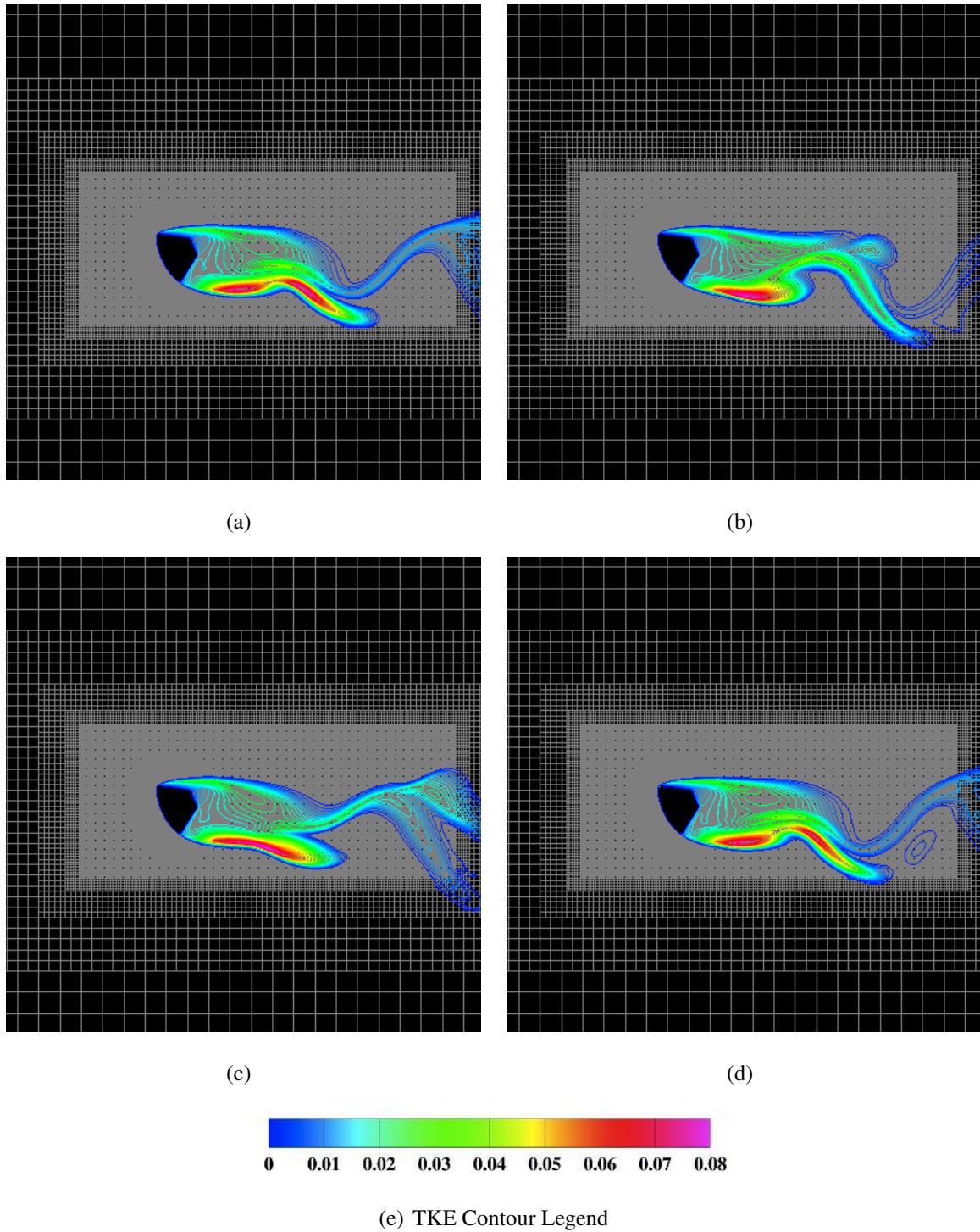
Figure 4.34. Zoomed in TKE contours in the pitch plane for the lagRST model showing the wake at $\alpha = 154.4°$.

(a)

(b)

(c)

(d)

(e) Mach Contour Legend

Figure 4.35. Mach contours in the pitch plane for the lagRSTSST model showing the wake at $\alpha = 154.4°$.

(a)

(b)

(c)

(d)

(e) Mach Contour Legend
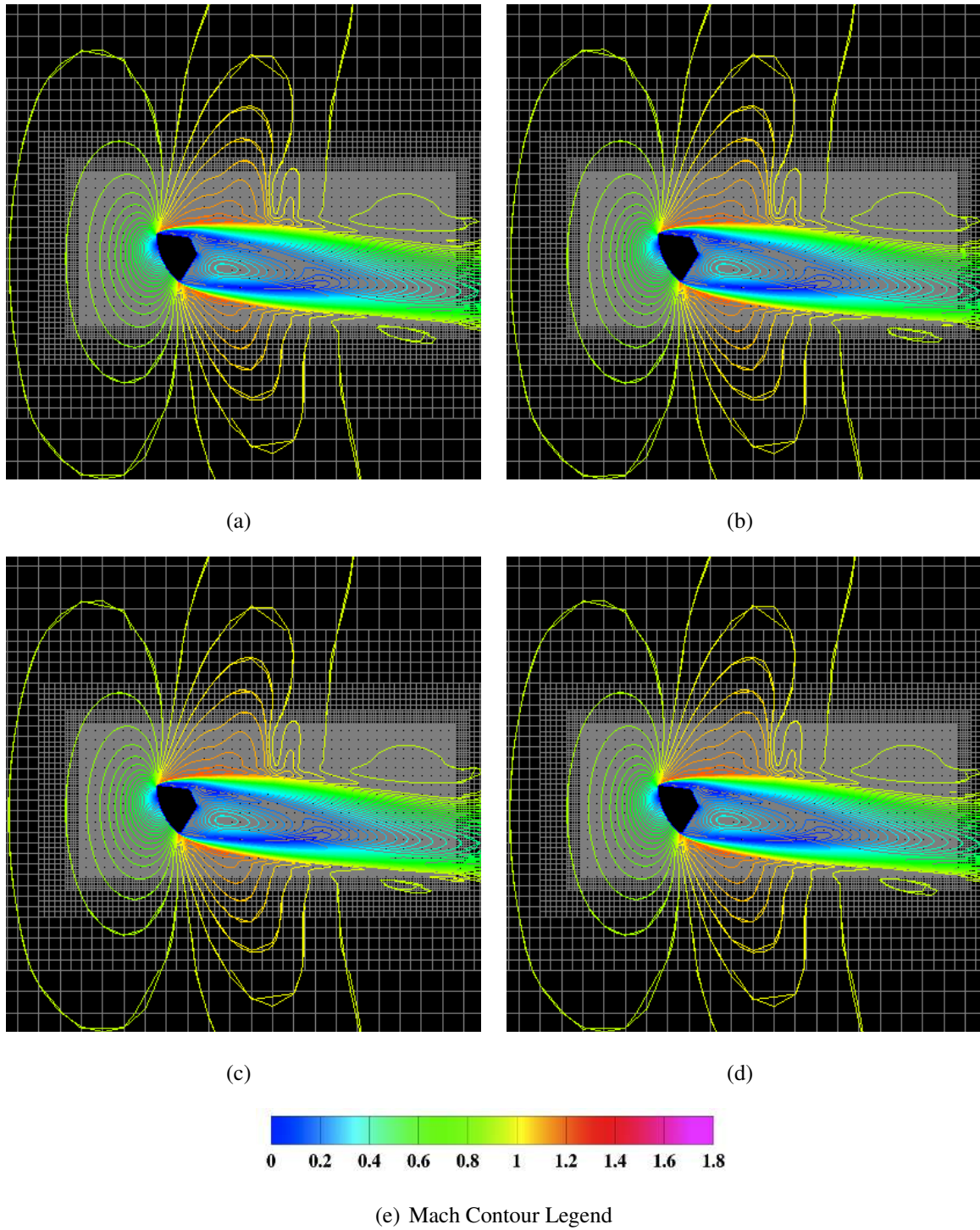
Figure 4.36. Zoomed in Mach contours in the pitch plane for the la-gRSTSST model showing the wake at $\alpha = 154.4°$.

(a)

(b)

(c)

(d)

(e) TKE Contour Legend

Figure 4.37. TKE contours in the pitch plane for the lagRSTSST model showing the wake at $\alpha = 154.4°$.

(a)

(b)

(c)

(d)

(e) TKE Contour Legend

Figure 4.38. Zoomed in TKE contours in the pitch plane for the la-gRSTSST model showing the wake at $\alpha = 154.4°$.

171

(a)

(b)

(c)

(d)

(e) Mach Contour Legend
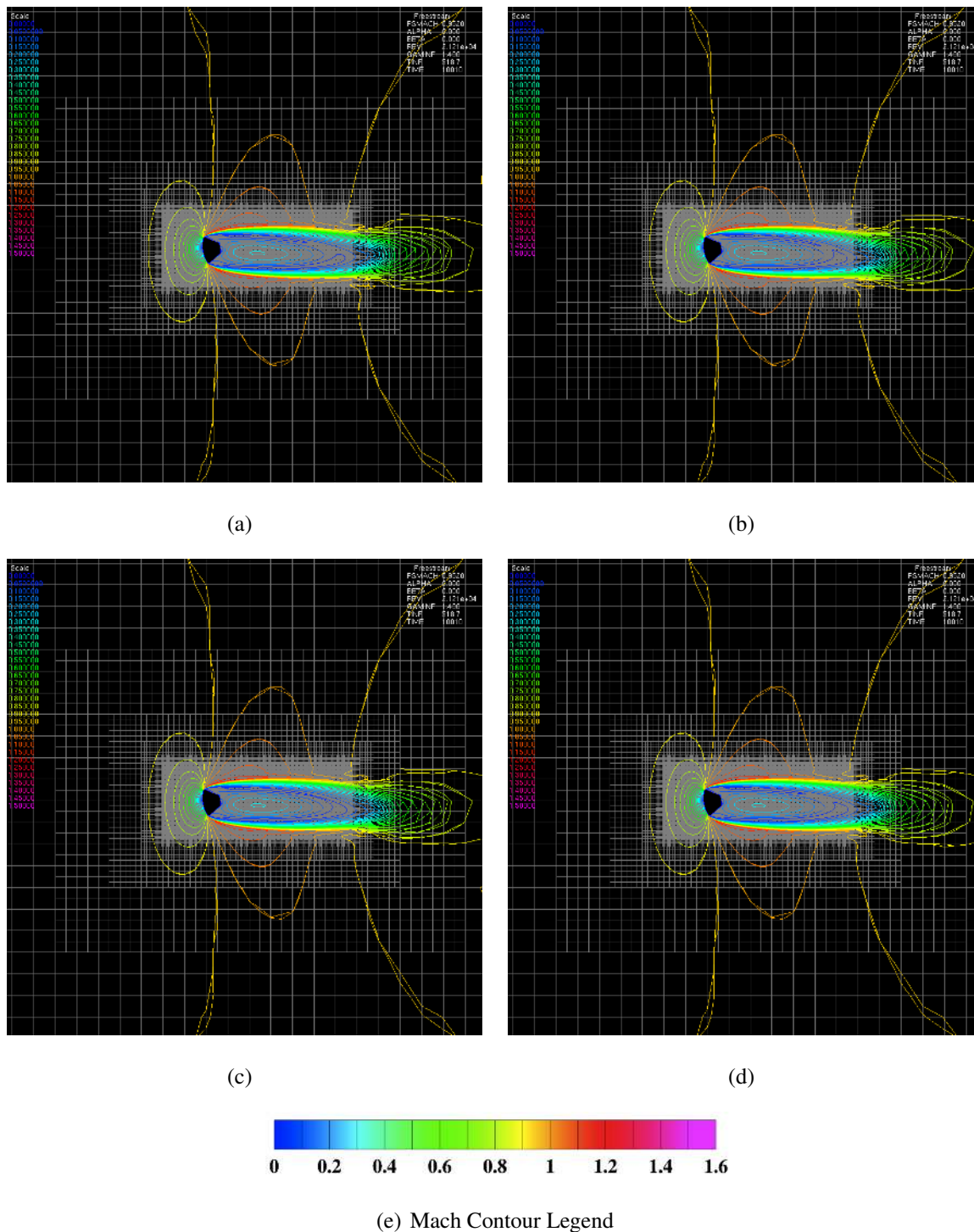
Figure 4.39. Mach contours in the pitch plane for the lagRST model showing the wake at $\alpha = 170.4°$.

(a)

(b)

(c)

(d)

(e) Mach Contour Legend
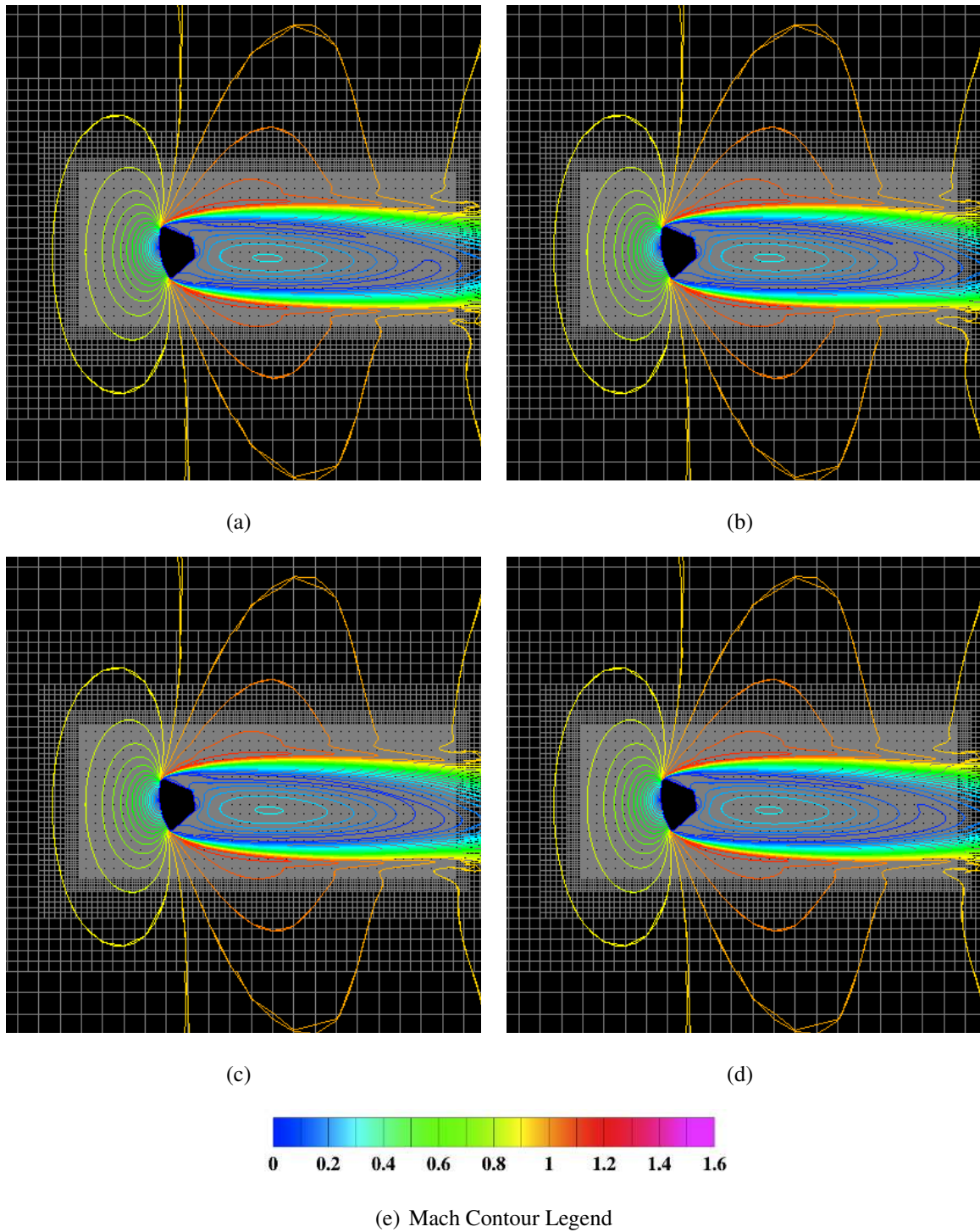
Figure 4.40. Zoomed in Mach contours in the pitch plane for the lagRST model showing the wake at $\alpha = 170.4°$.

(a)

(b)

(c)

(d)

(e) TKE Contour Legend

Figure 4.41. TKE contours in the pitch plane for the lagRST model show-
ing the wake at $\alpha = 170.4°$.

(a)

(b)

(c)

(d)

(e) TKE Contour Legend
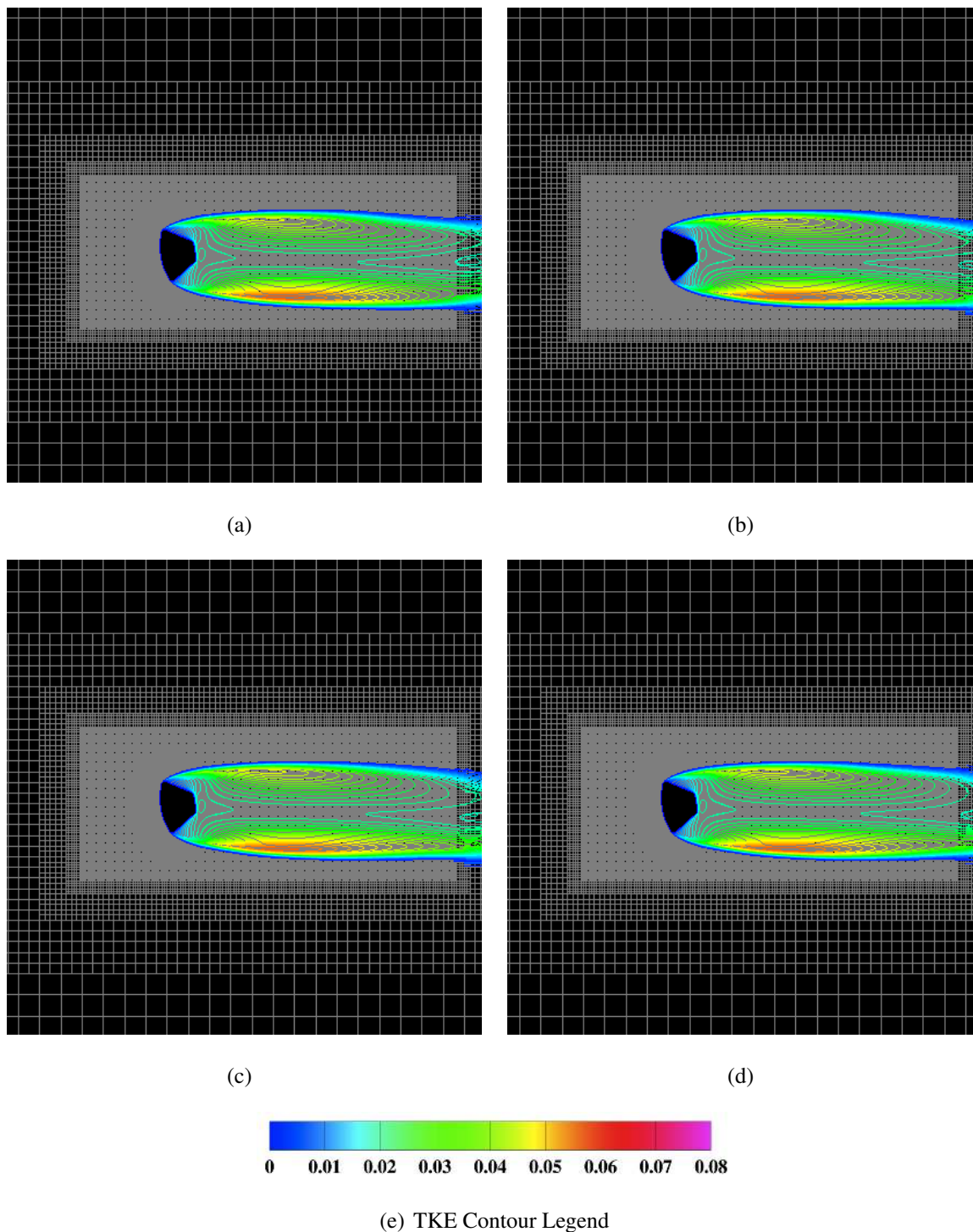
Figure 4.42. Zoomed in TKE contours in the pitch plane for the lagRST model showing the wake at $\alpha = 170.4°$.

(a)

(b)

(c)

(d)
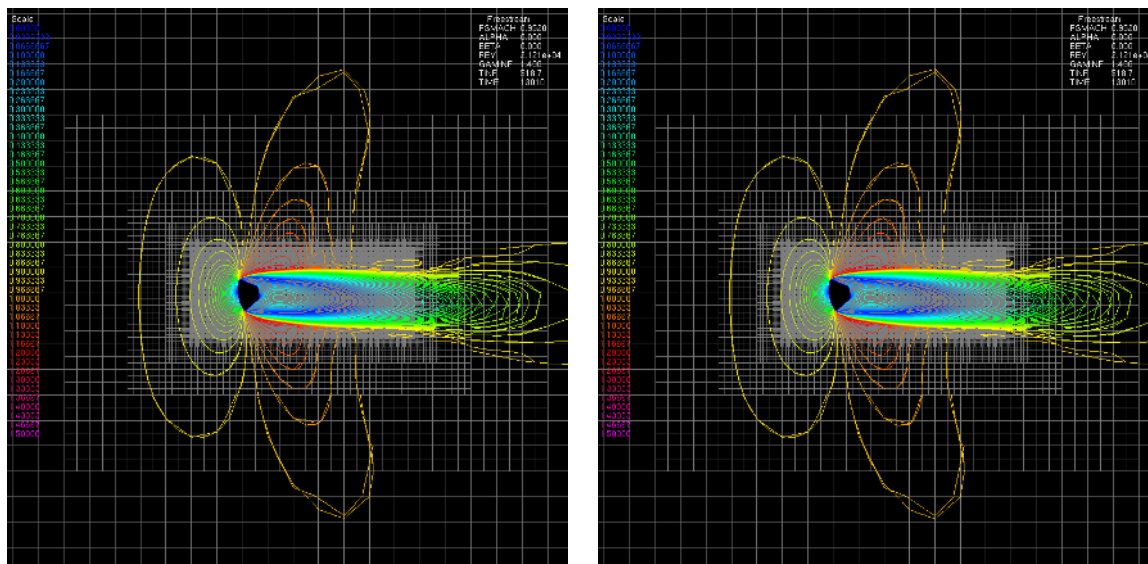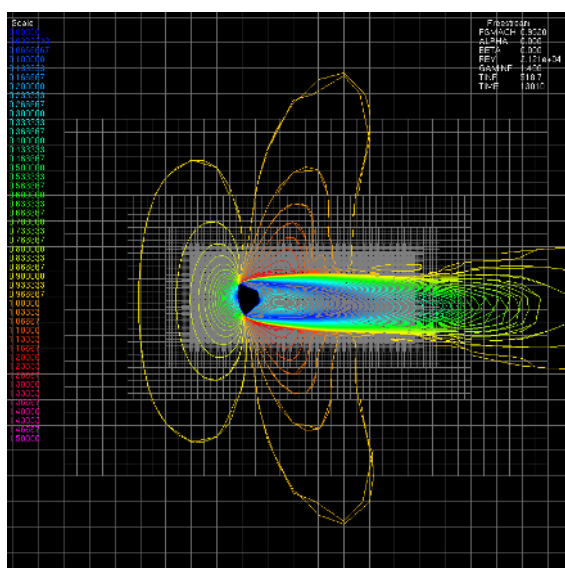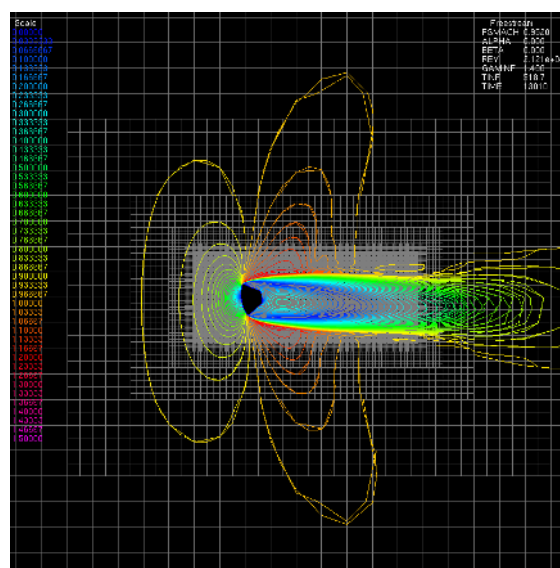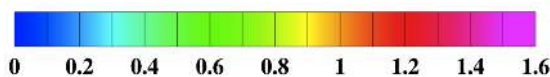
(e) Mach Contour Legend

Figure 4.43. Mach contours in the pitch plane for the lagRSTSST model showing the wake at $\alpha = 170.4°$.

(a)

(b)

(c)

(d)

(e) Mach Contour Legend
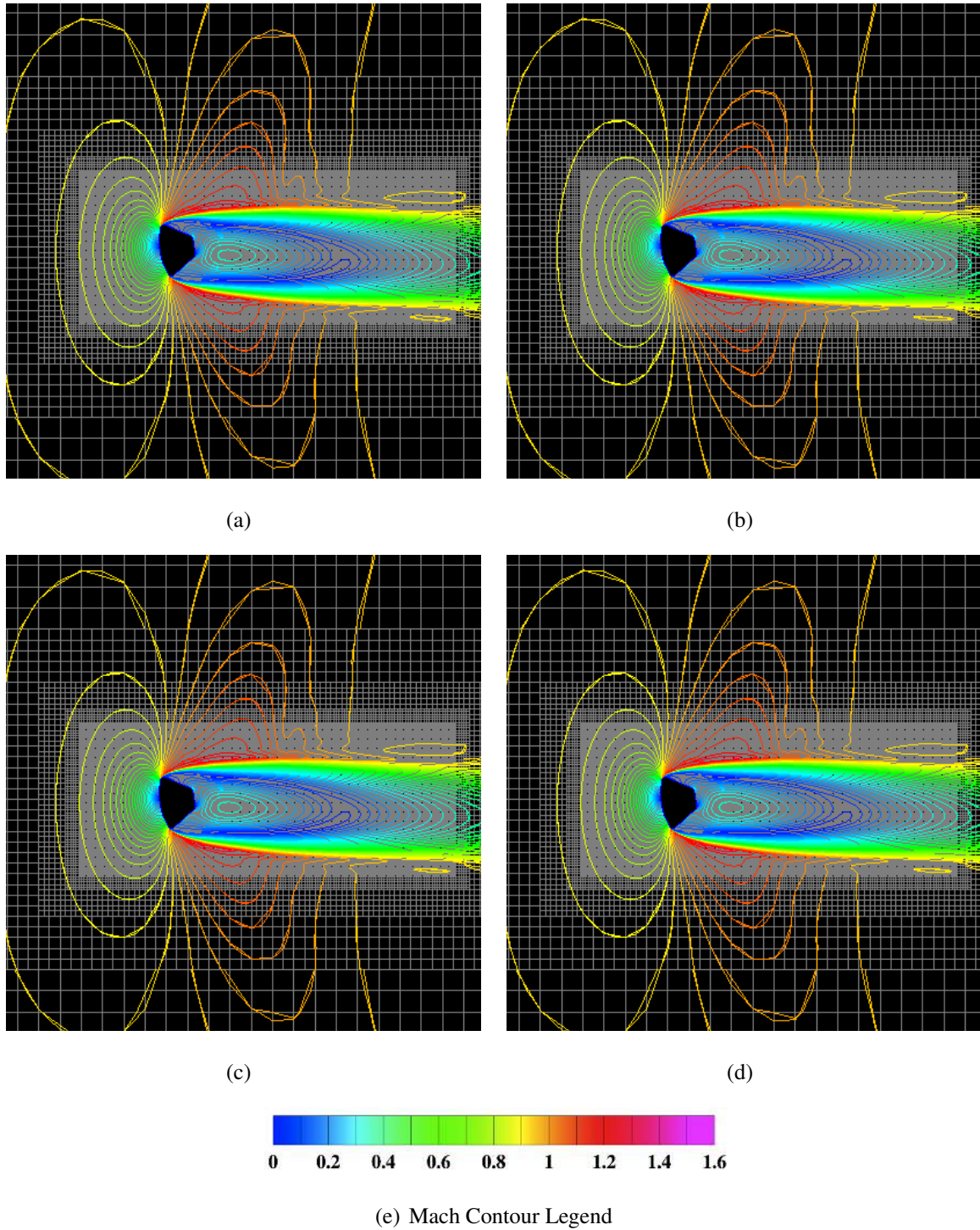
Figure 4.44. Zoomed in Mach contours in the pitch plane for the la-gRSTSST model showing the wake at $\alpha = 170.4°$.
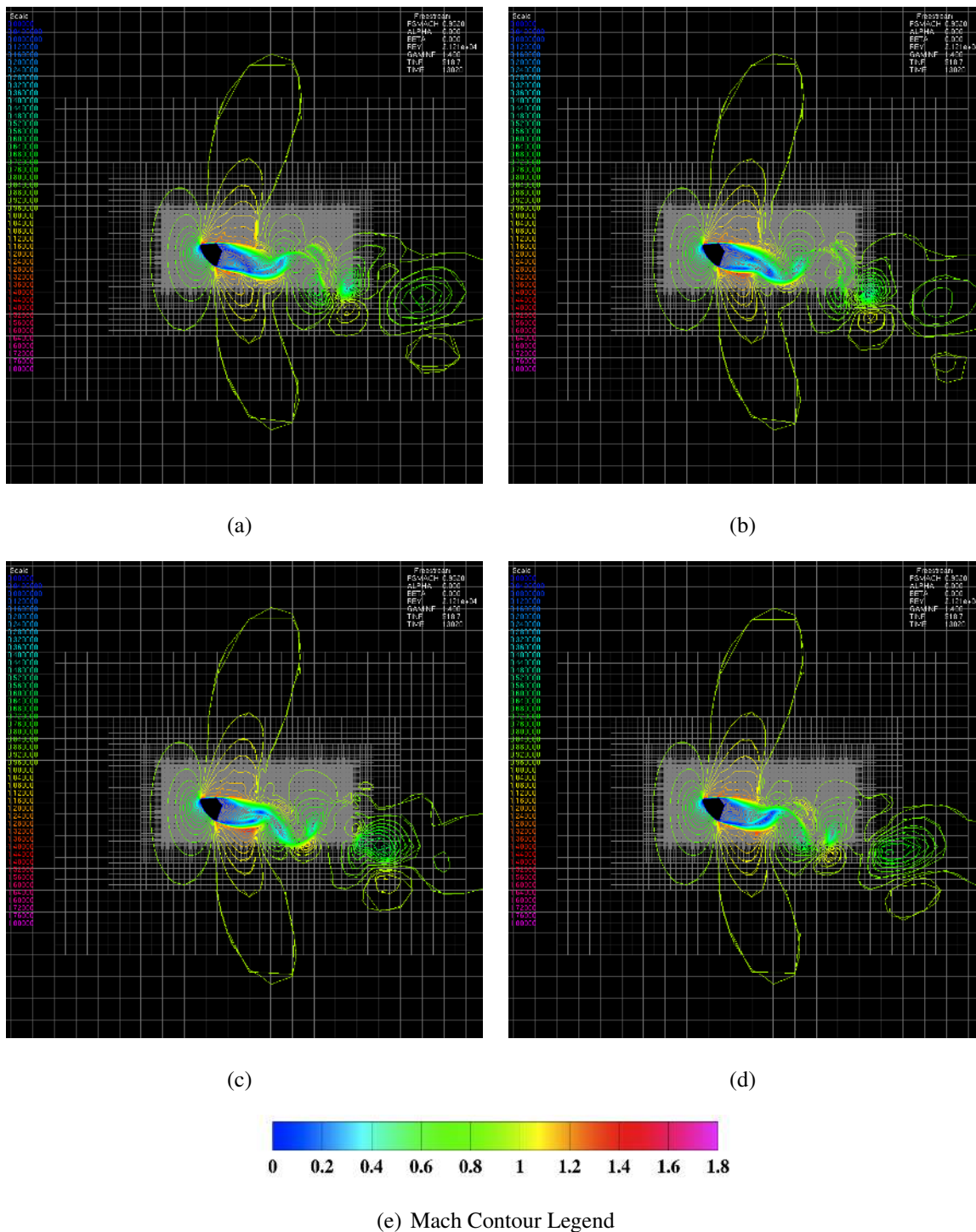
(a)

(b)

(c)

(d)
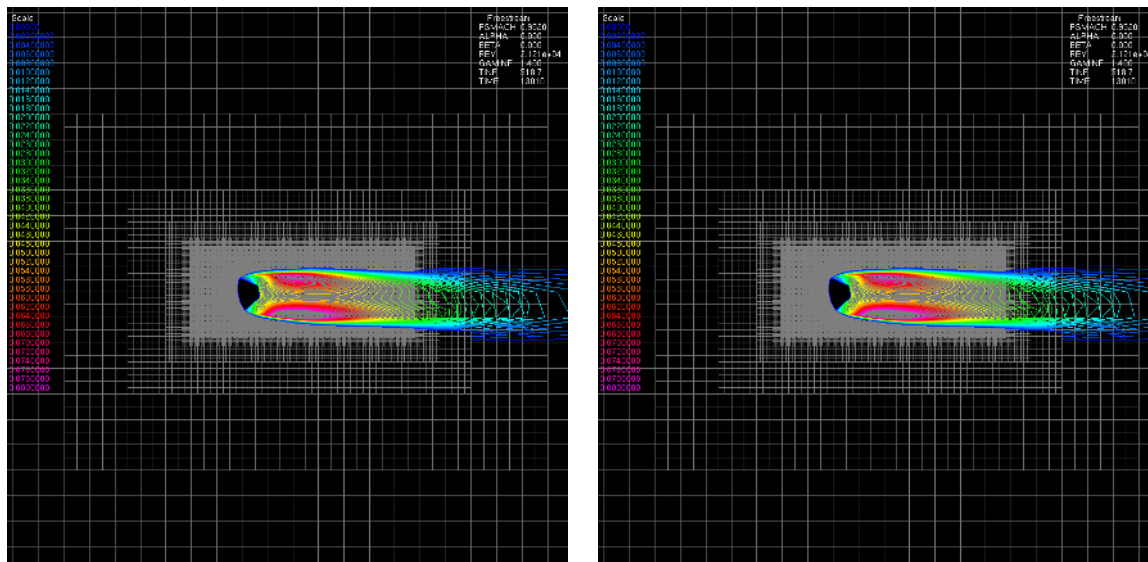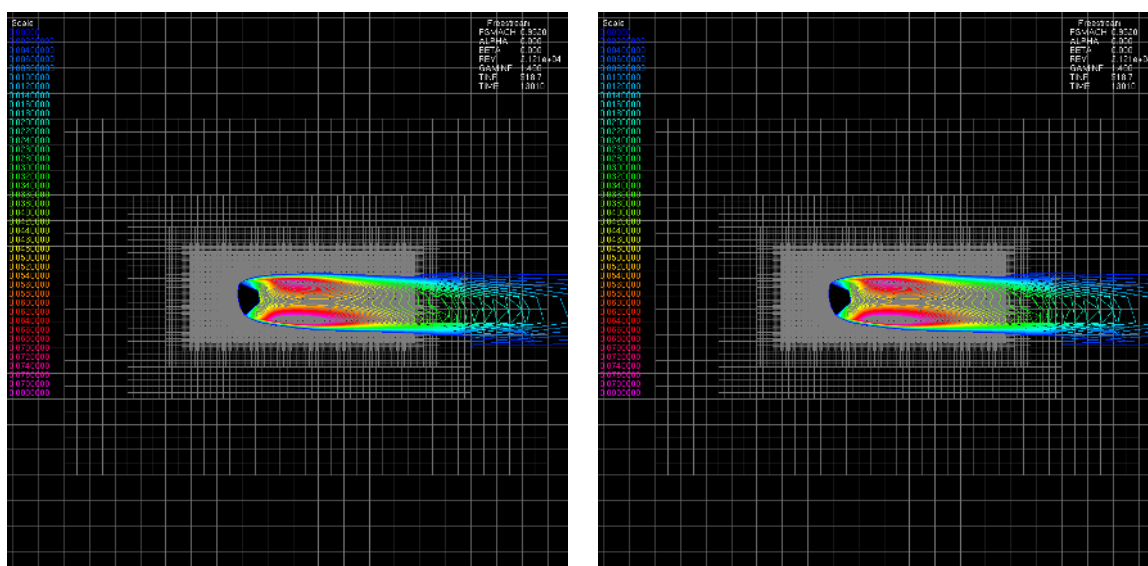
(e) TKE Contour Legend

Figure 4.45. TKE contours in the pitch plane for the lagRSTSST model showing the wake at $\alpha = 170.4°$.

(a)

(b)

(c)

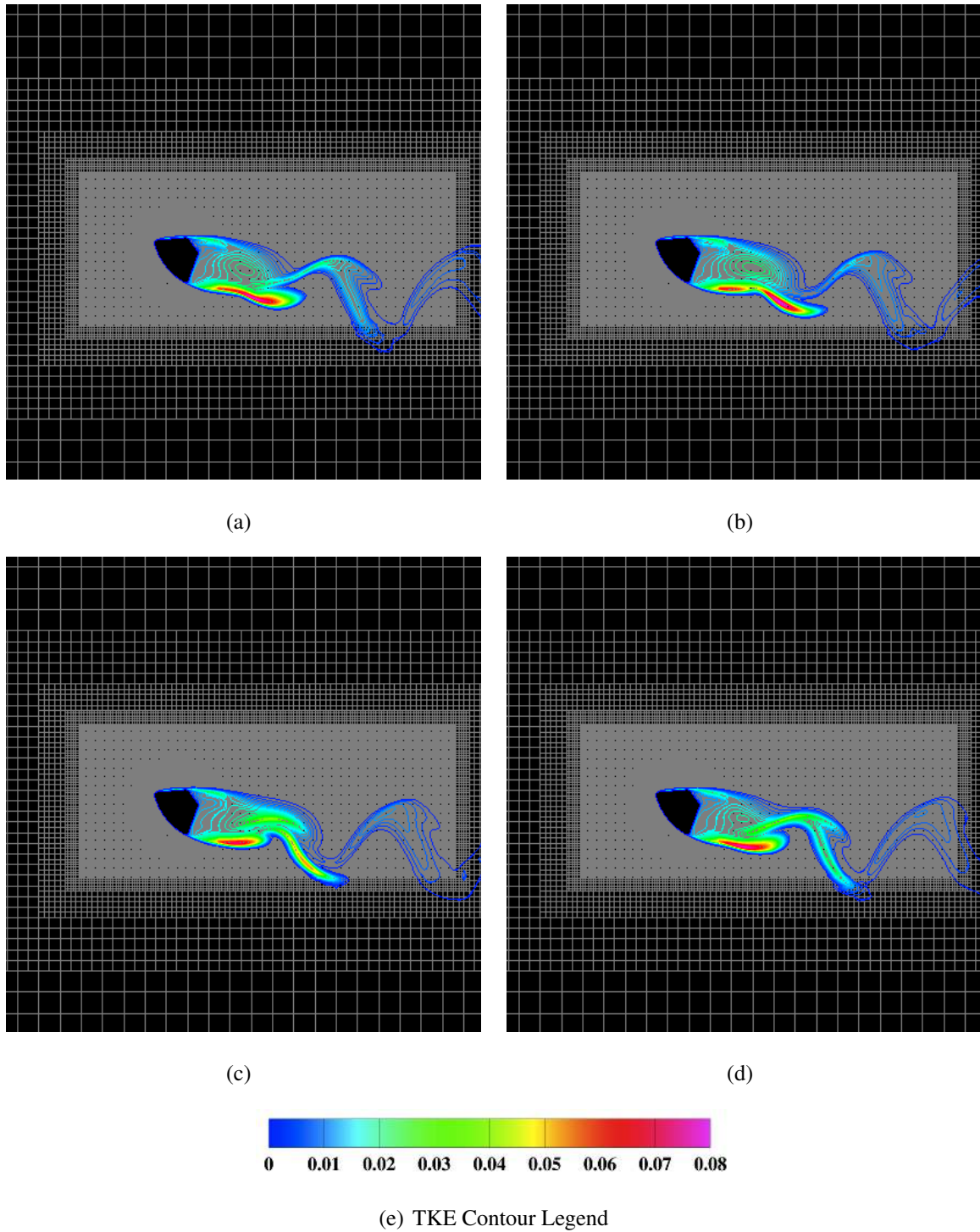(d)

(e) TKE Contour Legend
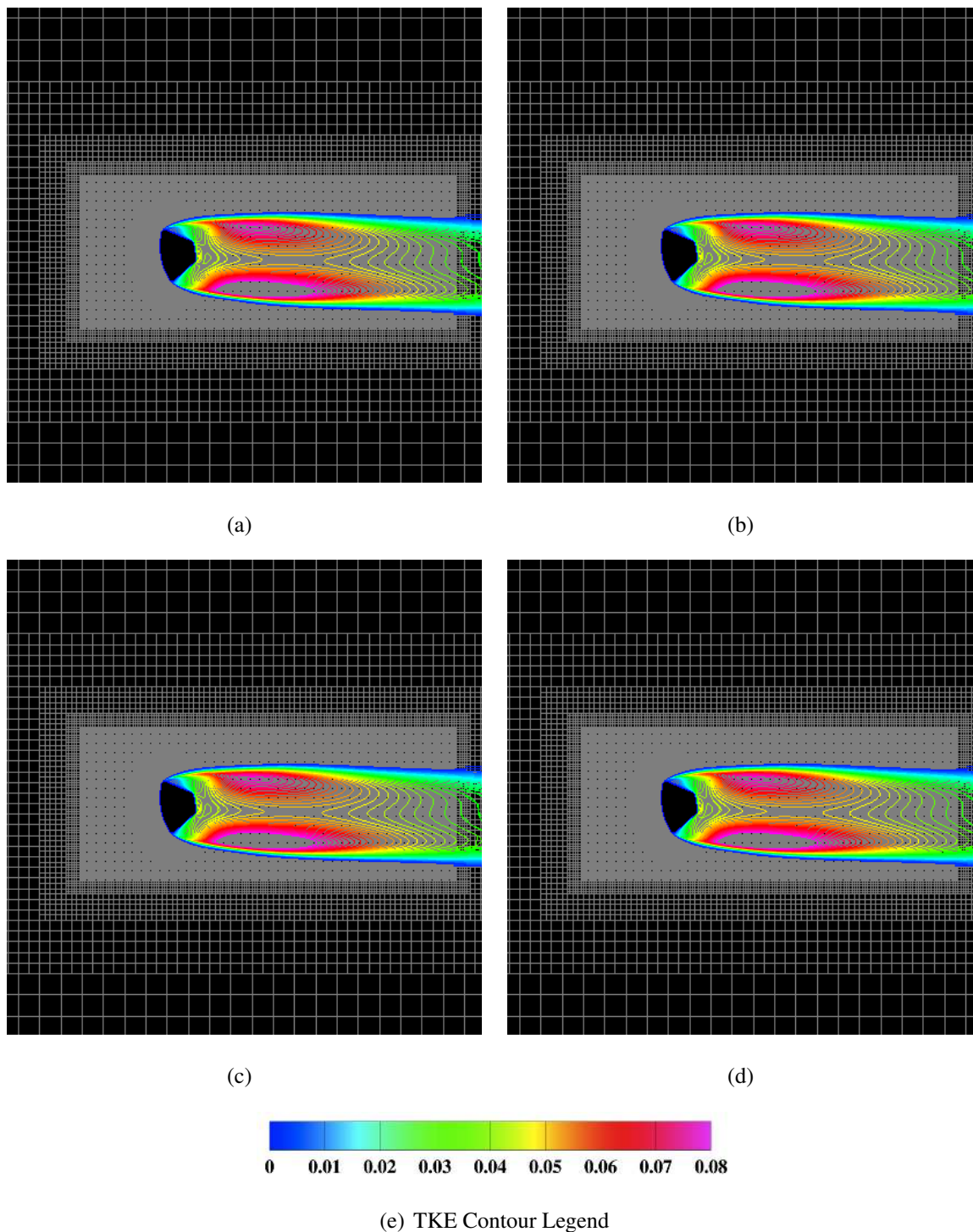
Figure 4.46. Zoomed in TKE contours in the pitch plane for the la-gRSTSST model showing the wake at $\alpha = 170.4°$.

5. Summary

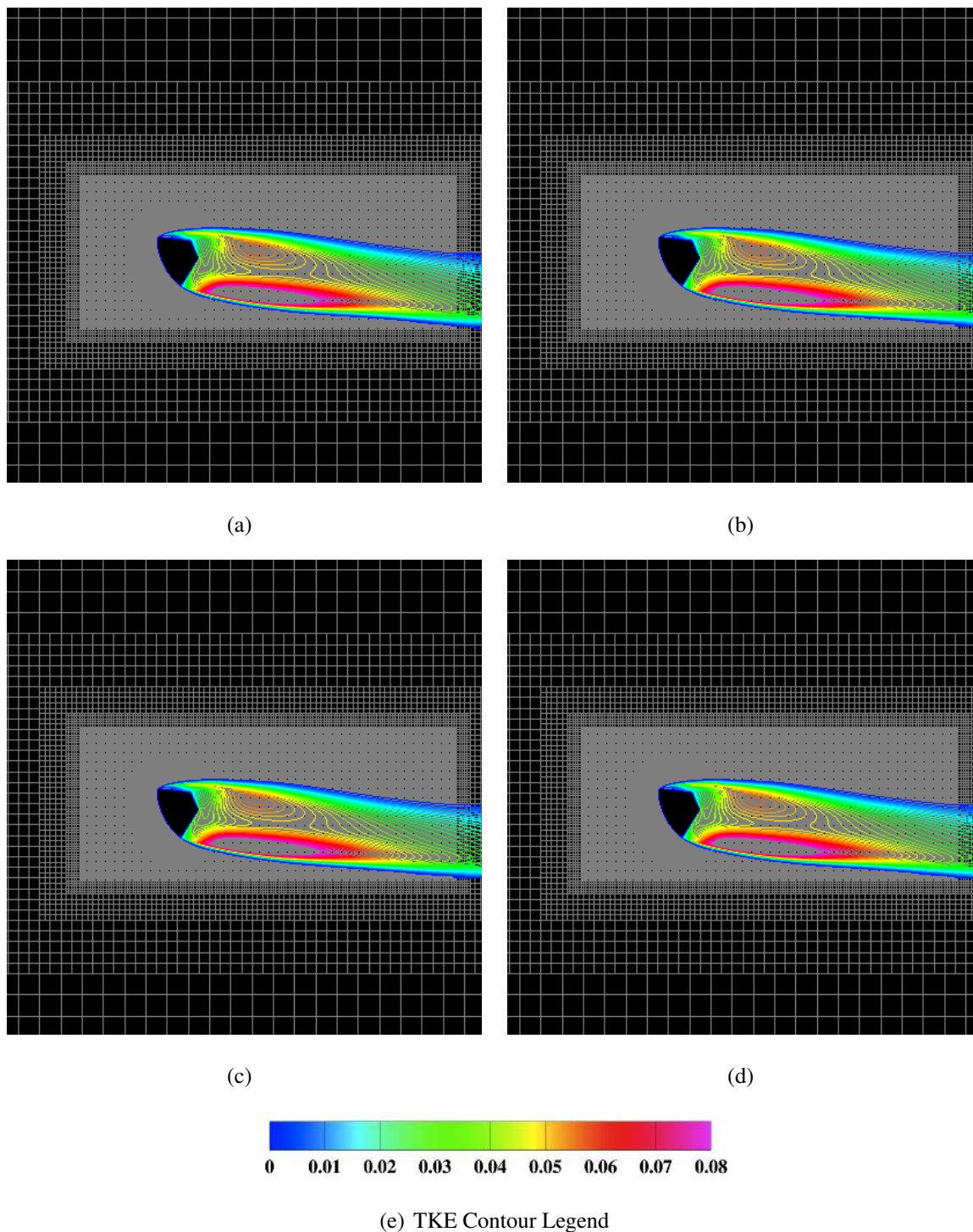The goal of the current research is to advance current turbulence modeling capabilities in the prediction of shock wave turbulent boundary layer interactions and flows with massive separation for complex configurations, relevant to NASA Johnson Space Center. The current methodology involves taking a baseline $k - \omega$ turbulence model and using it to define equilibrium turbulent values to drive the actual Reynolds Stresses towards. This is done with a simple "lag" equation. The new aspect of this work is using actual modeled Reynolds stresses in a production CFD code and applying them to real geometries of interest in a URANS method. By actually solving for the Reynolds Stresses and not the turbulent eddy viscosity, the models are allowed to relax to their non-equilibrium values with more degrees of freedom.

The initial study was on four computationally "simple" test cases, an incompressible flat plate, a turbulent mixing layer, an incompressible adverse pressure gradient turbulent boundary layer with separation, and a transonic bump. The results of this initial study showed mixed results, with no singular implementation of the model providing the best results. All of the implementations worked well for the incompressible turbulent boundary layer, but none of the models were able to predict the proper shape of the velocity profile near the edge. This is not surprising, as typical closure techniques concentrate on matching the wall properties and the law of the wall first. For the mixing layer, the $k - \omega$ based models incorrectly predicted the spreading rate by nearly a factor of two below the experimentally determined value. In contrast, the SST based models predicted a spreading rate that matched the experimental data very well. This result was unexpected and is still being assessed with the developer of the lag model. In contrast, the separation predictions were far more accurate using the $k - \omega$ based models, with the standard lagRST model providing excellent results. The SST based models over predicted the separation zone for both the incompressible and transonic test cases by over 40%.

The major set of analysis done in this project centered around the predictions on two test cases. The first test case was a hypersonic SWBLI of an impinging oblique shock on a fully developed turbulent boundary layer that cause separation. For this test case, the baseline SST model provided separation zone length predictions that were less than 1%. The lagRSTSST model predicted the separation point too early which caused the separation zone to be almost 30% too large. The lag and lagRST models predicted separations zones between 45% to 60% too high. Although this is the case, of particular interest to was the peak heat flux prediction at reattachment. The SST model over predicted this heat flux by 65%. By lagging the Reynolds Stresses, the peak heat flux prediction reduced by 25%. So although the lagging technique had an adverse affect on the prediction of the separation zone, it did have a positive effect on one of the negative characteristics of the SST model for SWTBLI.

The final analysis was done on a geometry of particular interest to NASA, the Orion (now MPCV) capsule. The grid system and techniques used here are the ones used by NASA's aerodynamics teams building the aerodynamic databases for these vehicles, and the baseline models are the ones used by NASA. The first contribution of this analysis is that the Reynolds Stress modeling implemented in the OVERFLOW code is robust and can be ran in an unsteady, time accurate fashion and provide grid converged results. This is a significant contribution since the predictions are solving for Reynolds Stresses. The results for this case showed excellent results for the lag technique. The standard turbulence models (Spalart Allmaras and SST) almost always provided higher percent errors than the lag based models. The lag, lagRST, and lagRSTSST models all were able to generally predict the C_D and C_L to less than 10%. Several of the lag based models predicted oscillating wakes with Strouhal numbers comparable to the experimentally obtained values at lower α's. Unfortunately, none of the models were able to predict an unsteady wake at the highest α.

All the lag model performance per iteration is assessed in table 5.1 along with the SST model. The ratio is the time taken for the given turbulence model over the SA model. The Lag model, because it doesn't use the wall distance, is extremely close to the speed of the SA model. For reference, the SST model is 20% slower than SA. The lagRST model is

35% slower than the SA and the lagRSTSST is 40% slower per iteration. These timings were taking from the flat plate analysis.

SST	lag	lagRST	lagRSTSST
1.2	1.075	1.35	1.4

Table 5.1 Ratio of the given time taken to run one iteration with the given turbulence model in relation to the SA model.

6. Recommendations

It is clear from the analysis done that one lag based Reynolds Stress model does not solve all the problems identified in separation and SWTBLI predictions. Based the suite of cases, two models will be recommended for further study. The lagRST-1 model will be treated as the baseline lagRST model, with the same coefficients used in the standard eddy viscosity lag model, $a_o = 0.35$ and $\sigma_k = 0.8$. This model did very well for incompressible and transonic flow predictions. It should be noted that if the flow of interest has a mixing layer component, the predictions need to be validated with experiments because of its poor predictions of the growth rate of the Bell Mehta mixing layer. Although this mixing layer issue needs to be explained, it did not seem to affect the capsule predictions. The lagRSTSST model with the standard coefficients ($a_o = 0.35$) also performed well for the complicated test cases. The issue with this model is its separation prediction for incompressible and transonic flat plates, where the results were very poor. The separation predictions for this model were actually better for the SWBLI than for the simpler cases, and the lag equations reduced the peak heat flux at the reflected shock. This is a promising results, as an over prediction of the magnitude SST had would most likely result in over design of the TPS system.

The SWBLI results should be verified in other wind tunnel tests to ensure consistent behavior. Brown [21] has identified two other high quality experimental datasets that could be used. One dataset is the Mach 8.9 experiment of Murray [42–44] which was conducted at the Imperial College Nitrogen gun tunnel. This test series consists of a hollow axisymmetric cylinder with an axisymmetric cowl use as a shock ring generator. Data available for this case are wall pressure and heat flux. The second experiment is the Mach 8.18 experiment of Kussoy and Horstman [45]. It was conducted on a 2D flat plate in the no longer operational NASA Ames Research Center Hypersonic facility. The test configuration was the nominal 2D flat plate with a shock generator inclined, similar to the Schulein config-

uration assessed in this study. Pressure, skin friction, and heat flux were obtained in this study as well as flow field quantities (no turbulence quantities) were obtained.

In addition to assessing more configurations, here are also several other forms of the turbulence model that should be assessed. In particular, the forms of the Reynolds stress tensor used in the lagRST model could provide numerical and / or physical modeling improvements over the current implementation. Two of these forms are detailed below. The anisotropy tensor has been used by several other researchers in this type of modeling and may provide improvements to the predictions.

Instead of using τ_{ij}, the mean normal stress component can be subtracted from the Reynolds stress to leave the deviatoric portion of the tensor. The Boussinesq equation (2.10) can be rewritten to show

$$\tau_{ij_{eq}} - \frac{1}{3}\tau_{kk_{eq}}\delta_{ij} = 2\rho\nu_{t_{eq}}\left(s_{ij} - \frac{1}{3}s_{kk}\delta_{ij}\right),$$
(6.1)

$$\tau_{ij_{eq}}^{D} = 2\nu_{t_{eq}}s_{ij}^{D}\rho,$$
(6.2)

where the superscript D denotes the deviatoric part of the tensor. The lag equation would then become

$$\frac{\partial\tau_{ij}^{D}}{\partial t} + \frac{\partial}{\partial x_k}(\tau_{ij}^{D}\tilde{u}_k) = a_o\omega\left(\tau_{ij_{eq}}^{D} - \tau_{ij}^{D}\right)$$
(6.3)

In this formulation, the turbulent kinetic energy solved for in equation 2.3 would be the actual lagged variable used in all flowfield computations.

Reynolds stress anisotropy tensor is another option, discussed below.

$$b_{ij} = \frac{\widetilde{\bar{\rho}u_i'u_j'} - \frac{1}{3}\widetilde{\bar{\rho}u_k'u_k'}\delta_{ij}}{\widetilde{\bar{\rho}u_l'u_l'}}$$
(6.4)

By substituting equations 2.8 and 2.11 into the equation for b_{ij}, you arrive at

$$b_{ij} = -\frac{\tau_{ij} - \frac{1}{3}\tau_{kk}\delta_{ij}}{2\bar{\rho}k}.$$
(6.5)

The numerator of the previous equation is the deviatoric Reynolds stress tensor (left hand side of equation 6.1), thus substitution leaves

$$b_{ij} = -\frac{\tau_{ij}^D}{2\bar{\rho}k}.$$ (6.6)

Equation 6.2 can then be used to define the $b_{ij_{eq}}$, the equilibrium anisotropic Reynolds stress tensor,

$$b_{ij_{eq}} = -\frac{\mu_t s_{ij}^D}{\bar{\rho}k}.$$ (6.7)

The lag equation would then become

$$\frac{\partial \bar{\rho}b_{ij}}{\partial t} + \frac{\partial}{\partial x_k}(\bar{\rho}b_{ij}\tilde{u}_k) = a_o\omega\left(\bar{\rho}b_{ij_{eq}} - \bar{\rho}b_{ij}\right)$$ (6.8)

Another possibility is to remove the Boussinesq approximation and drive the Reynolds Stress tensor to a higher closure model. This could be done by solving for an algebraic Reynolds Stress tensor.

Although it is not directly part of this work, it would also be of value to the community of the differences in the SST models in OVERFLOW 2.0aa and 2.2c were identified and published, and the most optimum set used in the lagRSTSST implementation.

LIST OF REFERENCES

LIST OF REFERENCES

[1] Columbia Accident Investigation Board. *Report Volume I*. August 2003.

[2] T. P. Wadhams, M. G. MacLean, M. S. Holden, and G. J. Smolinski. Return to flight testing of a 3.5% scale space shuttle ots and ot model at mach numbers of 3.5 and 4.0. In *44th AIAA Aerospace Sciences Meeting and Exhibit, January 9-12, 2006, Reno, NV*, January 2006. AIAA 2006-720.

[3] P. Buning. Nasa larc, private communciation. 2004.

[4] D. C. Jespersen, T. H. Pulliam, and P. G. Buning. Recent enhancements to overflow. In *AIAA 35th Aerospace Sciences Meeting, Reno, NV*, January 1997. AIAA 97-0644.

[5] Mike E. Olsen and Dinesh K. Prabhu. Application of overflow to hypersonic perfect gas flowfields. In *15th AIAA Fluid Dynamics Conference, Anaheim, CA*, June 2001. AIAA 2001-2664.

[6] R. P. Lillard and K. M. Dries. Laminar heating validation of the overflow code. In *43rd AIAA Aerospace Sciences Meeting and Exhibit, Reno, Nevada, 2005*, January 2005. AIAA 2005-0689.

[7] M. E. Olsen, T. J. Coakley, and R. P. Lillard. The lag model applied to high speed flows. In *43rd AIAA Aerospace Sciences Meeting and Exhibit, Reno, Nevada*, January 2005. AIAA 2005-0101.

[8] M. E. Olsen, N. Chaderjain, R. P. Lillard, J. S. Greathouse, and T. J. Coakley. Numerical study of massively separated flows. In *45th AIAA Aerospace Sciences Meeting and Exhibit, Reno, Nevada*, January 2007. AIAA 2007-1412.

[9] T. B. Gatski and G. Erlebacher. Numerical simulation of a spatially evolving supersonic turbulent boundary layer. Technical Report NASA TM 211934, NASA LaRC Research Center, September 2002.

[10] S. Pirozzoli, F. Grasso, and T. B. Gatski. Direct numerical simulation and analysis of a spatially evolving supersonic turbulent boundary layer at M=2.25. *Physics of Fluids*, 16(3):530–545, 2004.

[11] S. Pirozzoli, F. Grasso, and T. B. Gatski. DNS of a shock wave turbulent boundary layer interaction at M = 2.25. In *57th Annual Meeting of the American Physical Society, Division of Fluid Dynamics, Seattle, WA*, November 2004.

[12] S. Pirozzoli, F. Grasso, and T. B. Gatski. DNS analysis of a shock wave / turbulent boundary layer interaction at M=2.25. In *Fourth International Symposium on Turbulence and Shear Flow Phenomena, Williamsburg, VA*, June 2005.

[13] E. T. Spyropoulos. *On Dynamic Subgrid-Scale Modeling for Large-Eddy Simulations of Compressible Turbulent Flows*. PhD Thesis, Purdue University, West Lafayette, IN, December 1996.

[14] E. T. Spyropoulos and G. A. Blaisdell. Large-eddy simulations of a spatially evolving supersonic turbulent boundary layer flow. *AIAA Journal*, 36:1983–1990, November 1998.

[15] M. Wu and M.P. Martin. Direct numerical simulation of shockwave and turbulent boundary layer interactions. In *57th Annual Meeting of the American Physical Society, Division of Fluid Dynamics, Seattle, WA*, November 2004.

[16] M. Wu, P. Bookey, M.P. Martin, and A. J. Smits. Analysis of shockwave / turbulent boundary layer interaction using DNS and experimental data. In *43rd AIAA Aerospace Sciences Meeting and Exhibit, Reno, NV*, January 2005. AIAA 2005-310.

[17] P. Bookey, C. Wyckham, and A. Smits. Experimental investigation of a Mach 3 shock-wave turbulent boundary layer interaction. In *35th AIAA Fluid Dynamics Conference and Exhibit, Toronto, Ontario*, June 2005. AIAA 2005-4899.

[18] G. S. Settles and L. J. Dodson. Hypersonic Shock/Boundary-Layer Interaction Database. Technical Report 177577, Pennsylvania State University, University Park, PA, April 1991. NASA Contractor Report.

[19] C. J. Roy and F. G. Blottner. Review and assessment of turbulence models for hypersonic flows. 2006. AIAA 2006-713.

[20] D. Knight, H. Yan, A. G. Panaras, and A. Zheltovodov. Advances in CFD prediction of shock wave turbulent boundary layer interactions. *Progress in Aerospace Sciences*, 39:121–184, 2003.

[21] James L. Brown. Shock wave impingement on boundary layers at hypersonic speeds: Computational analysis and uncertainty. In *42nd AIAA Thermophysics Conference, 27 - 30 June 2011, Honolulu, HI*, June 2011. AIAA 2011-3143.

[22] D. C. Reda and J. D. Murphy. Shock wave - turbulent boundary layer interactions in rectangular channels. In *AIAA 5th Fluid and Plasma Dynamics Conference, Boston, MA*, June 1972. AIAA 72-715.

[23] D. C. Reda and J. D. Murphy. Shock wave/turbulent boundary-layer interactions in rectangular channels. *AIAA Journal*, 11(2):139–140, February 1973.

[24] William C. Rose and Dennis A. Johnson. A study of shock-wave turbulent boundary layer interaction using laser velocimeter and hot-wire anemometer techniques. In *AIAA 12th Aerospace Sciences Meeting, Washington, D.C.*, January 1974. AIAA 1974-95.

[25] D. C. Reda and J. D. Murphy. Shock wave - turbulent boundary layer interactions in rectangular channels, part ii: The influence of sidewall boundary layers on incient separation and scale of the interaction. In *AIAA 11th Aerospace Sciences Meeting, Washington, D.C.*, January 1973. AIAA 1973-234.

[26] D. C. Reda and J. D. Murphy. Sidewall boundary layer influence on ishock wave/turbulent boundary-layer interactions. *AIAA Journal*, 11(10):1367–1368, October 1973.

[27] D. C. Reda. Comment on 'Calculation of a turbulent boundary-layer shock-wave interaction'. *AIAA Journal*, 12(9):1291–1292, September 1974.

[28] W. C. Rose. Turbulence measurements in a compressible boundary layer. *AIAA Journal*, 12(8):1060–1064, 1974.

[29] W. C. Rose. The behavior of a compressible turbulent boundary layer in a shock-wave induced adverse pressure gradient. Technical report, University of Washington, Seattle, WA, March 1973. NASA Contractor Report TN D-7092.

[30] W. C. Rose and M. E. Childs. Reynolds-shear-stress measurements in a compressible boundary layer within a shock-wave-induced adverse pressure gradient. *Journal of Fluid Mechanics*, 65:277–188, 1974.

[31] C. C. Horstman and F. K. Owen. Turbulent properties of a compressible boundary layer. *AIAA Journal*, 10(11):1418–1424, 1972.

[32] F. K. Owen, C. C. Horstman, and M. I. Kussoy. Mean and fluctuating flow measurements of a fully-developed, non-adiabatic hypersonic boundary layer. *Journal of Fluid Mechanics*, 70:393–413, July 1975.

[33] M. I. Kussoy and C. C. Horstman. An experimental documentation of a hypersonic shock-wave turbulent boundary-layer interaction flow - with and without separation. Technical Report NASA TMX 62412, NASA Ames Research Center, February 1975.

[34] C. C. Horstman, M. I. Kussoy, T. J. Coakley, M. W. Rubesin, and J. G. Marvin. Shock-wave-induced turbulent boundary-layer separation at hypersonic speeds. In *AIAA 13th Aerospace Sciences Meeting, Pasadena, CA*, January 1975. AIAA 75-4.

[35] V. Mikulla and C. Horstman. Turbulence measurements in hypersonic shock-wave boundary layer interaction flows. *AIAA Journal*, 14(5):568–75, 1976.

[36] T. J. Coakley, J. R. Viegas, and c. C. Horstman. Evaluation of turbulence models for three primary types of shock separated boundary layers. In *AIAA 10th Fluid and Plasma Dynamics Conference, Albuquerque, NM*, June 1977. AIAA 77-692.

[37] J. R. Viegas and T. J. Coakley. Numerical investigations of turbulence models for shock separated boundary-layer flows. In *AIAA 15th Aerospace Sciences Meeting, Los Angeles, CA*, January 1977. AIAA 77-44.

[38] S. T. Vuong and T. J. Coakley. Modeling of turbulence for hypersonic flows with and without separation. In *AIAA 25th Aerospace Sciences Meeting, Reno, NV*, January 1987. AIAA 87-286.

[39] S. J. Kline, B. J. Cantwell, and G. M. Lilley. Proceedings of the 1980-81 AFOSR-HTTM Stanford conference on complex turbulent flows. In *Stanford University, Stanford, CA*, 1981.

[40] E. Schulein, P. Krogmann, and E. Stanewsky. Documentation of two-dimensional impinging shock/turbulent bound- ary layer interaction flow. Technical Report Rept. 1B 223-96 A 49, DLR, German Aerospace Center, Gottingen, Germany, October 1996.

[41] E. Schulein. Skin friction and heat flux measurements in shock boundary layer interaction flows. *AIAA Journal*, 44(8):1732–1741, 2006.

[42] N. Murray and R. Hillier. Hypersonic shockwave/turbulent boundary layer interactions in a three-dimensional flow. In *44th AIAA Aerospace Sciences Meeting and Exhibit, Reno, NV*, January 2006. AIAA 2006-121.

[43] N. Murray and R. Hillier. Separated shockwave/turbulent boundary layer interactions at hypersonic speeds. In *36th AIAA Fluid Dynamics Conference and Exhibit, San Francisco, CA*, June 2006. AIAA 2006-3038.

[44] N. Murray. *Three-Dimensional Turbulent Shock-Wave/Boundary Layer Interactions at Hypersonic Speeds*. PhD Dissertation, Imperial College, University of London, 2007.

[45] M. Kussoy and K. Horstman. Documentation of two- and three-dimensional shock wave turbulent boundary layer interactions at Mach 8.2. Technical Report NASA TM 103838, NASA Ames Research Center, May 1991.

[46] J. M. Osterlund. *Experimental Studies of Zero Pressure-Gradient Turbulent Boundary-Layer FLow*. PhD Thesis, Royal Institute of Technology, Se-100 44 Stockholm, Sweden, December 1999.

[47] J. M. Osterlund, A. V. Johansson, H. M. Nagib, and M. H. Hites. 1999 wall shear stress measurements in high reynolds number boundary layers from two facilities. In *30th AIAA Fluid Dynamics Conference, Norfolk, VA*, 1999. AIAA 1999-3814.

[48] J. H. Bell and R. D. Mehtai. Development of a two-stream mixing layer from tripped and untripped boundary layers. *AIAA Journal*, 28(12):2034–2043, December 1990.

[49] M. E. Olsen and T. J. Coakley. Reynolds shear stress measurements in a separated boundary layer flow. In *AIAA 22nd Fluid Dynamics, Plasma Dynamics, and Lasers Conference, Honolulu, Hawaii*, June 1991. AIAA 1991-1787.

[50] W. D. Bachalo and D. A. Johnson. Transonic, turbulent boundary-layer separation generated on an axisymmetric flow field. *AIAA Journal*, 24(3):437–443, 1986.

[51] J. Bell. Transonic/Supersonic Wind Tunnel Testing of the NASA Crew Exploration Vehicle (CEV). In *45th AIAA Aerospace Sciences Meeting and Exhibit, 8 - 11 January 2007, Reno, NV*, January 2007. AIAA Paper 2007-1006.

[52] J. Bell. Test 5-CA Final Report. EG-CEV-06-19, March 2006.

[53] D. C. Wilcox. *Turbulence Modelling for CFD*. DCW Industries, Inc., La Canada, CA, 1998.

[54] J. R. Viegas and C. C. Horstman. Comparison of multiequation turbulence models for several shock boundary-layer interaction flows. *AIAA Journal*, 17(8):811–820, 1979.

[55] J. R. Viegas, M. W. Rubesin, and C. C. Horstman. On the use of wall functions as boundary conditions for two-dimensional separated compressible flows. In *AIAA 23rd Aerospace Sciences Meeting, Reno, NV*, January 1987. AIAA 85-0180.

[56] J. Champney. Modeling of turbulence for compression corner flows and internal flows. In *AIAA/ASME/SAE/ASEE 23th Joint Propulsion Conference, Monterey, CA*, July 1989. AIAA 89-2344.

[57] C. C. Horstman. Hypersonic shock-wave/turbulent-boundary layer interaction flows. *AIAA Journal*, 30(6):1480–1481, 1992.

[58] W. W. Liou and P. G. Huang. Calculations of Oblique Shock Wave/Turbulent Boundary-Layer Interactions with New Two-Equation Turbulence Models. Technical report, January 1996. NASA Contractor Report 198445.

[59] T. A. Marshall and D. S. Dolling. Computation of turbulent, separated, unswept compression ramp interactions. *AIAA Journal*, 30:2056–2065, 1992.

[60] L. Brusniak and D. Dolling. Engineering estimation of fluctuating loads in shock/wave turbulent boundary-layer interactions. *AIAA Journal*, 34(12):2554–61, 1996.

[61] D. Knight and G. Degrez. Shock wave boundary layer interactions in high Mach number flows: a critical survey of current CFD prediction capabilities. *AGARD Advisory Report 319*, II:1–1 to 1–35, December 1998.

[62] P. Durbin. On the k-ϵ stagnation point anomoly. *International Journal of Heat Fluid Flow*, 17(1):89–90, 1996.

[63] F. Thivet. Lessons learned from RANS simulations of shock-wave/boundary-layer interactions. In *40th AIAA Aerospace Sciences Meeting and Exhibit, Reno, NV*, January 2002. AIAA 2002-0583.

[64] D. P. Rizzetta. Evaluation of explicit algebraic reynolds-stress models for separated supersonic flows. *AIAA Journal*, 36:24–30, 1998.

[65] V. Viti, G. Huang, and P. Bradshaw. Implementation and validation of recent stress-transport turbulence models: the need for standardized procedures. In *43rd AIAA Aerospace Science Meeting and Exhibit, Reno, NV*, January 2005. AIAA 2005-112.

[66] F. H. Clauser. The turbulent boundary layer. *Advanced Applied Mechanics*, 4:1–54, 1956.

[67] C. C. Horstman. A turbulence model for nonequilibrium adverse pressure gradient flows. In *AIAA 9th Fluids and Plasma Dynamics Conference, San Diego, CA*, July 1976. AIAA 76-412.

[68] J. S. Shang and W. L. Hankey Jr. Numerical solution for a supersonic turbulent flow over a compression ramp. *AIAA Journal*, 13(10):1368–1374, 1975.

[69] G. S. Deiwert. Computation fo separated transonic turbulent flows. *AIAA Journal*, 14(6):735–740, June 1976.

[70] D. A. Johnson and L. S. King. A new turbulence closure model for boundary layer flows with strong adverse pressure gradients and separation. In *AIAA 22nd Aerospace Sciences Meeting, Reno, NV*, January 1984. AIAA 84-0175.

[71] D. A. Johnson and L. S. King. A mathematically simple turbulence closure model for attached and separated turbulent boundary layers. *AIAA Journal*, 23(11):1864–1692, 1985.

[72] S. Ahmed and J. C. Tannehill. Numerical prediction of turbulent flow over airfoil sections with a new nonequilibrium turbulence model. In *AIAA 21st Fluid Dynamics, Plasma Dynamics, and Lasers Conference, Seattle, WA*, June 1990. AIAA 1990-1469.

[73] S. Ahmed and J. C. Tannehill. New nonequilibrium turbulence model for calculating flows over airfoils. *AIAA Journal*, 30(2):302–303, 1992.

[74] R. Abid, V. N. Vasta, D. A. Johnson, and B. W. Wedan. Prediction of separated transonic wing flows with nonequilibrium algebraic turbulence model. *AIAA Journal*, 28(8):1426–1431, August 1990.

[75] T. A. Reyhner. Finite difference solutions of the compressible turbulent boundary layer equations. In *Proceedings of Computation of Turbulent Boundary Layers - 1968 AFOSR-IFP - Stanford Conference*, volume 1, pages 375–383, 1968.

[76] J. Lee, M. L. Sloan, and G. C. Paynter. Lag model for turbulent boundary layers over rough bleed surfaces. *Journal of Propulsion and Power*, 10(4):562–568, 1994.

[77] T. Cebeci and K. C. Chang. Calculation of incompressible rough wall boundary layer flows. *AIAA Journal*, 16(7):730–735, 1978.

[78] D. D. Knight and P. G. Saffman. Turbulence model predictions for flows with significant mean streamline curvature. In *AIAA 16th Aerospace Science Meeting, Hunstville, Alabama*, January 1978. AIAA 1978-258.

[79] C. G. Speziale and X. H. Xu. Towards the development of second-order closure models for nonequilibrium turbulent flows. *International Journal of Heat and Fluid FLow*, (17):238–244, 1996.

[80] F. Radhia, H. Marzougui, Z. Jihene, and T. Lili. On a relaxation model for nonequilibrium flows'. *Comptes Rendus Mecanique*, (338):355–360, July 2010.

[81] P. E. Hamlington and W. J. Dahm. Reynolds stress closure for nonequilibrium effects in turbulent flows. *Physics of Fluids*, 20(115101), 2009.

[82] P. E. Hamlington and W. J. Dahm. Computational validation of new reynolds stress closure for nonequilibrium effects in turbulent flows. In *47th AIAA Aerospace Sciences Meeting Including The New Horizons Forum and Aerospace Exposition, Orlando, FL*, January 2009. AIAA 2009-1323.

[83] M. Churchfield and G. Blaisdell. The lag rst turbulence model applied to a vortex flow. In *AIAA 46th Aerospace Sciences Meeting and Exhibit, Reno, NV*, January 2011. AIAA 2011-663.

[84] M. J. Churchfield. *The Lag RST Turbulence Model Applied to Vortical Flows*. PhD Thesis, Purdue University, West Lafayette, Indiana, August 2009.

[85] M. Churchfield and G. Blaisdell. A reynolds stress relaxation tubulence model applied to a wingtip vortex flow. In *49th AIAA Aerospace Sciences meeting including the New Horizons Forum and Aerospace Exhibition*, January 2008. AIAA 2008-0769.

[86] M. Olsen. Nasa arc, private communciation. 2009.

[87] F. R. Menter. Two-equation eddy-viscosity turbulence models for engineering applications. *AIAA Journal*, 32(8):1598–1605, August 1994.

[88] Florian R. Menter. Zonal two equation k-w turbulence models for aerodynamic flows. July 1993. AIAA paper 93-2906.

[89] M. E. Olsen and T. J. Coakley. The lag model, a turbulence model for non equilibrium flows. In *15th AIAA Fluid Dynamics Conference, Anaheim, CA*, June 2001. AIAA 2001-2564.

[90] H. H. Fernholz and P. J. Finley. The incompressible zero-pressure-gradient turbulent boundary layer: an assessment of the data. *Progress in Aerospace Sciences*, 32:245–311, 1996.

[91] K. E. Schoenherr. Resistance of flat surfaces moving through a fluid. *Trans. SNAME*, 40:279–313, 1932.

[92] R. D. Watson, R. M. Hall, and J. B. Anders. Review of skin friction measurements including recent high reynolds number results from nasa langley ntf. In *FLuids 2000, 19-22, June 2000, Denver, CO*, January 2000. AIAA 2000-2392.

[93] D. Coles. The law of the wake in the turbulent boundary layer. *Journal of Fluid Mechanics*, 1:1191–226, 1956.

[94] W. M. Rohsenow, J. P. Hartnett, and E. N. Ganic. *Handbook of heat transfr fundamentals*. McGraw-Hill Book Co., New York, NY, 2nd edition, 1985.

[95] N. N. Fedorova, I. A. Fedorchenko, and E. Schulein. Experimental and numerical study of oblique shock wave/turbulent boundary layer interaction at m = 5. *Computational Fluid Dynamics Journal*, 10(3):376–183, 2001. Special Issue.

[96] J. Steelant. Effect of a compressibility correction on different turbulence models. In W. Rodi and N. Fueyo, editors, *Engineering Turbulence Modeling and Experiments 5*, pages 207–216. Elsevier, 2002.

[97] M. A. Amaya and A. Boone. Calibration of the 11-by 11-foot transonic wind tunnel at the nasa ames research center. In *41st AIAA/ASME/SAE/ASEE Joint Propulsion Conference and Exhibit, Tucson, Arizona, July 10-13, 2005*, July 2005. AIAA 2005-4277.

[98] William M. Chan, Reynaldo J. Gomez, Stuart E. Rogers, and Pieter G. Buning. Best practices in overset grid generation. In *32nd AIAA Fluid Dynamics Conference, St. Louis, MO*, June 2002. AIAA 2002-3191.

[99] R. L. Meakin. Automatic off-body grid generation for domains of arbitrary size. June 2001. AIAA 2001-2536.

[100] R. L. Meakin. Object x-rays for cutting holes in composite overset structured meshes. June 2001. AIAA 2001-2537.

VITA

VITA

Randolph P. Lillard received his B.S. in Physics and Mathematics in December of 1998 from Morehead State University. He continued his studies at the Georgia Institute of Technology, obtaining a M.S. in August of 2000 from the School of Aerospace Engineering under Professor Jerry Seitzman and Professor Ed Price. As part of his masters thesis he researched the plateau burning behavior of composite solid propellants. Following the completion of his masters, he began working at the Johnson Space Center in the Applied Aerodynamics and Computational Fluid Dynamics Branch. During the next four years, he worked to improve CFD predictions for ascent aerothermodynamics on complex grids, contributed to multiple efforts during the Columbia Accident Investigation including pretest Arc-jet predictions and delta-aerodynamic calculations for missing Reinforced Carbon Carbon (RCC) panels, and internal flow modeling. In 2004, he received a one year NASA fellowship and entered the Doctoral program at Purdue University under the direction of Professor A. S. Lyrintzis and Professor G. A. Blaisdell. His Doctoral research was directed by the Space Shuttle Systems Engineering and Integration board and was intended to improve the state of ascent aerothermodynamic predictions. In 2005, he returned to Johnson Space Center and became the Orion Aerothermodynamics System Manager until 2009. Also in 2007, he became the Deputy Chief of the Applied Aerosciences and CFD Branch. In 2010, he was accepted into NASA's Systems Engineering Leadership Development Program and was detailed to NASA's Jet Propulsion Laboratory to work on the Juno Spacecraft. Finally in 2011, he was assigned to the Office of the Chief Technologist (OCT) at NASA Headquarters for a one year detail. During this time, he continued to work with Professors Blaisdell and Lyrintzis as well as researchers at NASA Ames and LaRC to improve turbulence modeling within the OVERFLOW code. After completing his Ph.D. degree in 2011 he will be returning to NASA OCT throughout the remainder of the 2012 fiscal year.